Report on the analogue modelling of the interactions between regional tectonics and volcanoes

Deliverable 3.5

Report on the analogue modelling of the interactions between regional tectonics and volcanoes

Deliverable 3.5

Version <final>

<Multiple authors>

Work package <WP 3.3>

<September 9th, 2019>

Website: http://www.gemex-h2020.eu

Authors

Marco Bonini, Daniele Maestrelli, Valerio Acocella, Damien Bonté, Gerardo Carrasco-Núñez, Giacomo Corti, Guido Giordano, Federico Lucci, Domenico Montanari, Giovanna Moratti, Gianluca Norini, Federico Rossetti, Stefano Urbani.

T 3.3 Leader: Marco Bonini

WP3 Leader: Damien Bonté

Coordinators:

Domenico Liotta

Víctor Hugo Garduño-Monroy

Table of Contents[1]

---

[1] The content of this report reflects only the authors' view. The Innovation and Networks Executive Agency (INEA) is not responsible for any use that may be made of the information it contains.

List of figures

7

begins to be visible as a system of small-throw conjugate normal faults developed on the left side of the model, where the diverging velocity of the two mobile plates is higher; (g) to (k) faults in the left side of the model gain larger displacement, developing well-structured graben systems that propagate towards the right side of the model (i.e. towards the poles of rotation); (k) after 220 minutes of deformation, the propagating rift has reached the rotation poles. Shallow and smaller grabens developed in this area, while in the left sector of the models the structures acquire larger throws. A clear increasing "V" shaped gradient of deformation toward the poles of rotation is detectable observing the overall ("a" to "l") model evolution. 50

Model RP-2 (Table 2.2; Fig. 3.3a) differs from reference model RP-1 in that we introduced artificial discontinuities belonging to set S1, which trend 30° with respect to the orthogonal to the direction of rift propagation (angle α = 30°; see Figure 3.3). A single set of discontinuities was introduced to avoid any possible reciprocal influence. The general model development did not differ from the evolution of RP-1, showing incipient normal faulting in the left-side area of the model, which progressively propagated toward the rotation poles (right-side of the model) to form a "V-shaped" subsiding wedge in the centre of the model. The wedge tip migrated progressively with the opening of the MP. Model deformation showed a clear gradient in terms of fault throw (larger for faults localized in the left-side of the model) and fault number (larger for faults localized in the left-side of the model). The average fault trend (red line in Fig. 3.3b) is N90° and the length of mapped fault traces shows a distribution marked by a large amount of small fault traces (the frequency peak of 25% is reached for fault trace class of 0.01-0.015 m) and some longer faults (up to 0.1 m). No evidence of reactivation of discontinuities belonging to set S1 is observed (Fig. 3.3a), as also notable from the rose diagram (Fig. 3.3b) where no classes trending N30° are present in the fault segment orientation. 51

List of tables

Executive summary

Deliverable D3.5 summarizes the results obtained by Task T3.3 members (CNR-UNIROMA TRE), implementing analogue models with the aim to test hypotheses about the structural evolution of the Los Humeros volcanic complex and Acoculco caldera systems. In this report, we present the results of two experimental series (Series D3.5-1 and D3.5-2), which were designed to investigate the interactions between regional tectonics and volcanoes. Specifically, Series D3.5-1 investigates the interaction between a propagating rift and inherited structures, while Series D3.5-2 investigates the influence of inherited discontinuities on caldera collapse.

In Chapter 1, we introduce the work of Task T3.3, reporting the regional as well as the local geological setting of Los Humeros volcanic complex and Acoculco caldera system. In Chapter 2, we furnish an introduction to analogue modelling procedure (Section 2.1), we describe the modelling strategy (Section 2.2) and the modelling procedures adopted for the two experimental series (Section 2.3 and 2.4), and, finally, the methodology adopted for monitoring and analysis of models (Section 2.5). In Chapter 3, we describe the results of analogue models (Section 3.1 for Series D3.5-1 and Section 3.2 for Series D3.5-2), while, in Chapter 4, we discuss the specific results of Series D3.5-1 (Section 4.1) and Series D3.5-2 (Section 4.2), and the clues provided by these experiments on the evolution of the Los Humeros and Acoculco volcanic systems (Section 4.3). Finally, Chapter 5 reports the conclusions of this study.

Models of Series D3.5-1 have shown that a propagating rift may reactivate inherited structures if favourably oriented. In particular, models applied to the natural case suggest that inherited faults trending N145° in the Los Humeros and Acoculco area are favourably oriented for reactivation. Analysis of fault dilation tendency performed on models suggests that these reactivated structures have a dilation component that may facilitate magmatic fluid migration. Models of Series D3.5-2 have shown that rectilinear discontinuities bounding an analogue magma chamber may form rectilinear structures at surface, not changing the chronology of fault pattern development, which is generally given by early outward-dipping reverse faults followed by inward-dipping normal faults. Inherited faults in the overburden above an analogue circular magma chamber may instead form intra-caldera rectilinear faults. Inherited faults bounding an analogue magma chamber and affecting the overburden stratigraphy may generate rectilinear caldera ring faults, sometimes inhibiting the formation of the inner reverse fault system. Models show a high degree of similarity with the structural setting of the Los Humeros and Acoculco magmatic systems, supporting the potential reactivation of inherited, rectilinear regional faults during caldera collapse.

1 Introduction

Experimental analogue modelling (carried out in the frame of Task 3.3) has focused on the interplay between regional tectonics, fault reactivation and magmatic processes in shaping volcanic edifices, which are aspects relevant for geothermal exploration. Analogue modelling is an experimental technique that allows to study geological processes in the lab, through the analysis of physical models built and deformed at reduced geometrical and temporal scales. In other words, tectonic processes occurring in millions of years, and length scales of tens to thousands of kilometres, are reproduced in the lab in hours/days and centimetre-scale. In the GEMex Project, analogue modelling has addressed two main research questions, particularly (1) interactions between regional tectonics and volcanoes, and (2) collapse of caldera and volcanic edifices and the associated surface deformation. The results of this activity are illustrated in two reports, namely Report D3.5 (*Report on the analogue modelling of the interactions between regional tectonics and volcanoes*), and Report D3.6 (*Report on the analogue modelling of the collapse of caldera and volcanic edifices and the associated surface deformation*). The set-up of analogue models is based on data available in the literature, as well as on new geological and geophysical data obtained through the GEMex Project (particularly from WPs 4 and 5). The results related to Report D3.5 are described below, starting from the geological setting of the study region, and of the Los Humeros volcanic complex and Acoculco caldera complex, which are host to the geothermal fields targeted by the GEMex Project. Analogue modelling carried out in this research has approached the study of the Los Humeros and Acoculco geothermal systems by investigating natural processes from a general point of view, and thus the experimental results provide original hints that can also be applied to other caldera and volcanic complexes worldwide.

All the different series of analogue models have been performed in the frame of Task 3.3 of the GEMex Project, and thus some parts of chapters 1 and 2 are common to deliverables 3.5 and 3.6 (namely, the regional geological setting, analogue modelling of volcano-tectonic processes, and monitoring and analysis of deformation).

Deliverable D3.5 reports the results of two experimental series addressing different aspects related to magmatic-related processes that may be relevant for geothermal exploration, namely: (1) the effect of a propagating rift on inherited fault reactivation (Series D3.5-1), and (2) testing the possible role of inherited faults on caldera collapse processes (Series D3.5-2). Series D3.5-1 and D3.5-2 have been performed at the Tectonic Modelling Laboratory of CNR-IGG Firenze.

1.1 Regional Geological setting

The Los Humeros and Acoculco geothermal fields occur on the eastern sector of the Trans-Mexican Volcanic Belt (TMVB), which is a large-scale ca. 1000 km-long, ESE-trending zone of volcano-tectonic deformation extending through central Mexico, approximately from the mouth of the Gulf of California up to the Gulf of Mexico (Fig. 1.1). The TMVB is a continental volcanic arc resulting from the subduction of the Cocos and Rivera plates beneath the North American plate along the Middle American trench. In the TMVB, magmatic activity started in Early Miocene (ca. 19 Ma) and extensional deformation affected this zone since Late Miocene (Ferrari et al., 2012, and references therein). The evolution of the TMVB is intimately linked to the evolution of subduction of the Farallon plate beneath the North America plate, which stalled in front of Baja California, then the Farallon slab broke at depth and successively slab tearing started to propagate (Burkett and Billen, 2010).
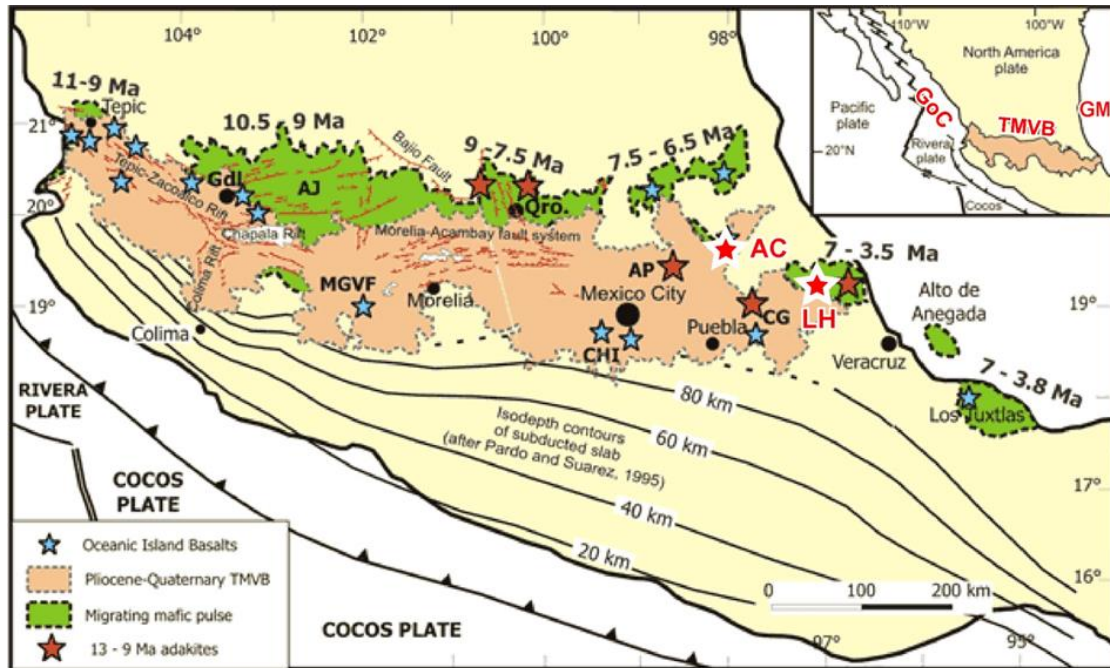
Figure 1.1 Regional geotectonic map of central Mexico, with indication of the study Los Humeros (LH) and Acoculco (AC) geothermal fields (from Ferrari et al., 2004). GoC, Gulf of California; GM, Gulf of Mexico; TMVB, Trans-Mexican Volcanic Belt.

According to Ferrari (2004), magmatism is associated with the lateral propagation of slab detachment beneath the TMVB during the late Miocene. In particular, slab tearing progressed eastward from the Gulf of California to the Gulf of Mexico, in a direction slightly oblique to the trench system (Fig. 1.2; Ferrari, 2004). Interestingly, the lateral propagation of the slab tear is marked by a pulse of mafic volcanism that migrated from west to east since ~11Ma, reaching the Gulf of Mexico by 7 Ma (Fig. 1.1; Ferrari et al., 2012).
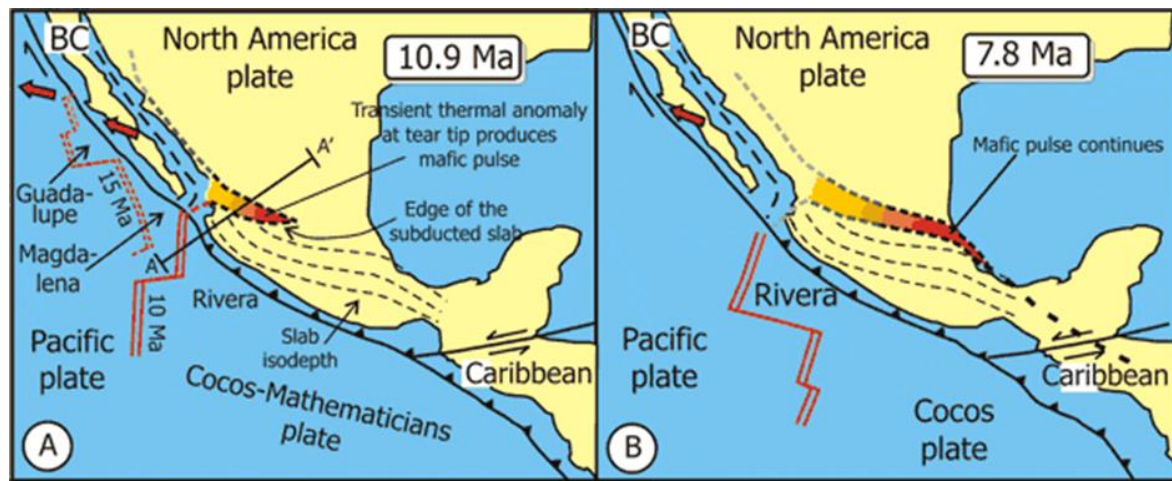
Figure 1.2. Evolution of slab tearing during Late Miocene with proposed location of slab detachment at 10.9 and 7.8 Ma (after Ferrari et al., 2004).

The TMVB covers several ancient fault systems that have been partially reactivated at different times during its evolution. In fact, since the end of the Eocene, the region encompassing the TMVB has been characterized by a broad transtensional kinematics (Alaniz-Álvarez and Nieto-Samaniego, 2007). However, the geometry, kinematics, and time-space distribution pattern of the brittle fault systems affecting the TMVB is complex. In detail, such an extensional deformation affecting the TMVB is relevant west of 100°W, whereas only a limited number of faults, with lesser vertical displacement, can be detected in the eastern TMVB (east of 100°W) (Fig. 1.1; e.g., Suter et al., 2001; Ferrari et al., 2012).

Normal faults affecting the TMVB are generally oriented around East-West, yet variations from ENE to ESE can be observed in the different sectors. Normal faulting shows complex time-space patterns. In the western TMVB, extensional deformation started in Late Miocene (e.g., Rosas-Elguera and Urrutia-Fucugauchi, 1998), with some faults ceasing their activity during Pleistocene (Ferrari et al., 2012), and others showing clear indications of neotectonic (Holocene) activity (e.g., Garduño-Monroy et al., 1993). Some normal faults have been even identified as being seismogenic sources that have produced large historic earthquakes (e.g., the M 6.9 Acambay earthquake of 1912; Suter et al., 1995). Faulting in the eastern TMVB is instead less intense, with the main normal faults being located around Mexico City, where they show evidence of Holocene activity with some left-lateral component of displacement (Norini et al., 2006). The occurrence of normal faults drastically decreases further east in the TMVB, and almost vanishes in the area of the Los Humeros and Acoculco (e.g., Ferrari et al., 2012). Although data on age of deformation is partial, a general southward migration of fault activity has been suggested for the western TMVB, while this pattern cannot be identified in the eastern TMVB where a low level of Pleistocene–Holocene tectonic deformation is reported for the Mexico City region (Ferrari et al., 2012). The general distribution and age of faulting pattern may also suggest that tectonic deformation has been progressing eastward, in a similar fashion of a propagating continental rift. This inference is important for the evolution of the deformation of the study area, and

consequently for assessing the boundary conditions for the analogue models addressing the interactions between regional tectonics and volcanoes (see section 2.2).

Regarding the recent/active tectonic stress field operating over the TMVB region, the World Stress Map (Heidbach et al., 2016) reports maximum horizontal stress (S_{Hmax}) axes approximately oriented from ca. E-W to NE, consistent with a N-S to NW-trending extension direction (Fig. 1.3). This extension direction seems to characterize also the eastern part of TMVB, including the study area in easternmost TMVB. Finally, this extension direction is also apparently coherent with a minor left-lateral component of displacement along the rift structure associated with the TMVB.
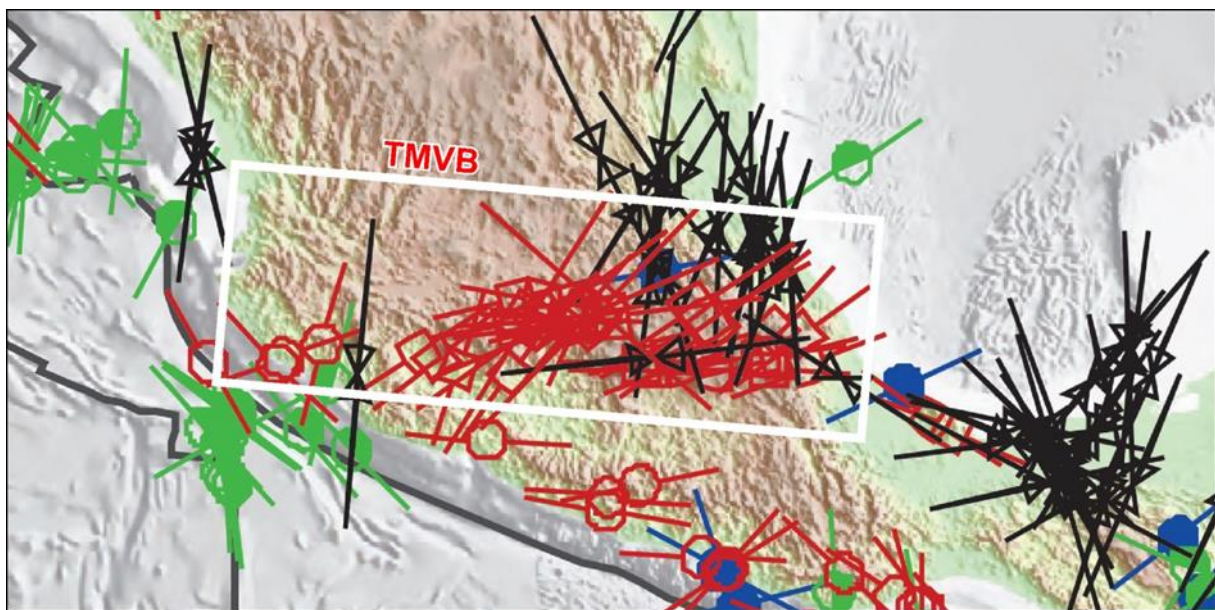
Figure 1.3. Detail of the World Stress Map 2016 for the Trans-Mexican Volcanic Belt (TMVB) (after Heidbach et al., 2016). Coloured bars display the orientation of the maximum horizontal compressional stress (S_{Hmax}) obtained from different data. The study Los Humeros and Acoculco geothermal fields are located on the easternmost sector of the TMVB (cf. with Fig. 1.1).

1.2 Geological setting of the Los Humeros volcanic complex

The Los Humeros volcanic complex (LHVC) is a prominent calc-alkaline, andesitic to rhyolitic volcanic centre located northwest of Perote town. The Pleistocene Teziutlán andesitic lavas form the main volcanic edifice, which experienced at least two large caldera collapse events (Ferriz and Mahood, 1984). The older caldera collapse produced the 15–20 km-wide Los Humeros Caldera and the emplacement of the 115 km^3 Xaltipan ignimbrite (Fig. 1.4). A second caldera collapse event led to the formation of the rhyodacitic Zaragoza ignimbrite (15 km^3) as well as the nested 8–10 km-wide Los Potreros Caldera (Ferriz and Mahood, 1984; Carrasco-Núñez et al., 2012). The caldera collapse structures and associated Xaltipan and Zaragoza

19

ignimbrite deposits are lay over the older Teziutlán volcanic edifice (see cross section in Carrasco-Núñez et al., 2017a; Fig. 1.4, lower panel).
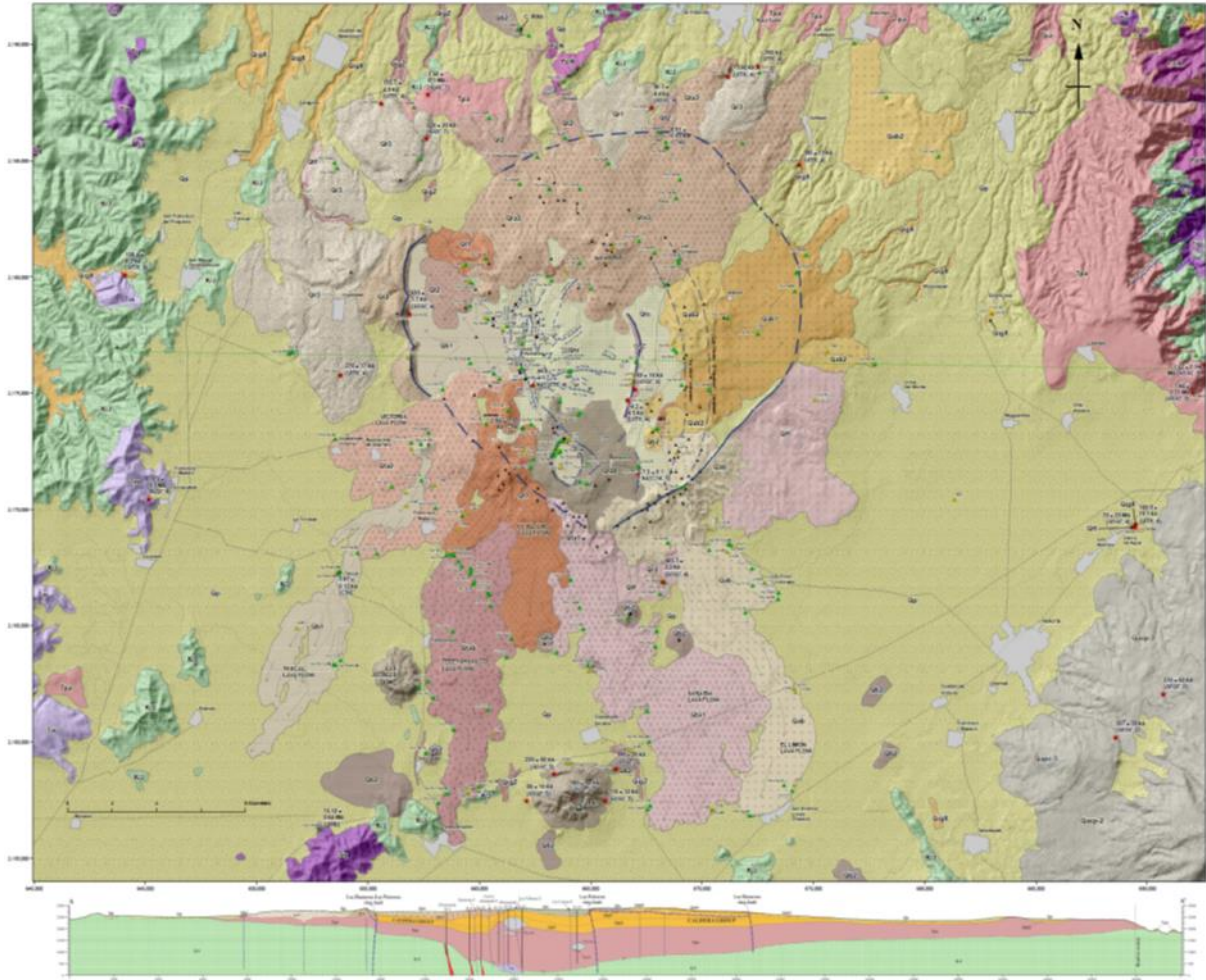
Figure 1.4. Geological map and geological section of the Los Humeros volcanic complex (after Carrasco-Núñez et al., 2017a; for details, the reader is refer to this publication).

Recent radiometric dating yields an age of 1.46 - 2.61 Ma for the Teziutlán andesites, while the Xaltipan and Zaragoza ignimbrites are dated at 164 ka and 69 ka, respectively (Carrasco-Núñez et al., 2018). Interpretative geological cross sections show both caldera structures as being controlled by either inward-dipping (Ferriz and Mahood, 1984; Cedillo-Rodríguez, 1999), or outward-dipping faults (Norini et al., 2015, 2019; Carrasco-Núñez et al., 2017a).

In map-view, the south-eastern margin of the Los Humeros Caldera is bounded by a ca. NE-trending linear scarp referred to as 'Los Humeros scarp', while its south-western rim is apparently controlled by a ca. NW-trending rectilinear structure that is hinted from the clear alignment of several volcanic vents (Carrasco-

Núñez et al., 2017a; Fig. 1.4). More specifically, the results carried out in the frame of GEMex activity propose that existing regional structures have been reactivated during the collapse of the Los Humeros Caldera, and have thus controlled caldera rim geometry (e.g., Liotta, 2019; Liotta and WP4 Working Group, 2019), particularly along its south-eastern and south-western margins (Fig. 1.5).

Figure 1.5. Schematic map of existing regional faults (thick blue and green lines) that are hinted to have controlled collapse of the Los Humeros Caldera (after Liotta, 2019).

The Los Potreros Caldera is defined by the 'Los Potreros scarp' and the 'Oyameles scarps' along its eastern and western margins, respectively (Norini et al., 2015; Fig. 1.4). Such exposed caldera collapse scarps vanish abruptly laterally, or are buried beneath the thick post-caldera products (Fig. 1.4).

A relevant set of faults affects the central part of the Los Potreros Caldera. These intra-caldera faults are characterized by fresh fault scarps denoting recent/ongoing activity. Such a fault system exhibits a complex pattern with fault segments showing two main orientations, particularly (1) faults trending NW to N–S, and dipping west (Maxtaloya and Humeros faults, as well as some minor faults) and (2) faults striking from E–W to ENE–WSW, dipping north (Las Papas and Arroyo Grande faults; Fig. 1.6).
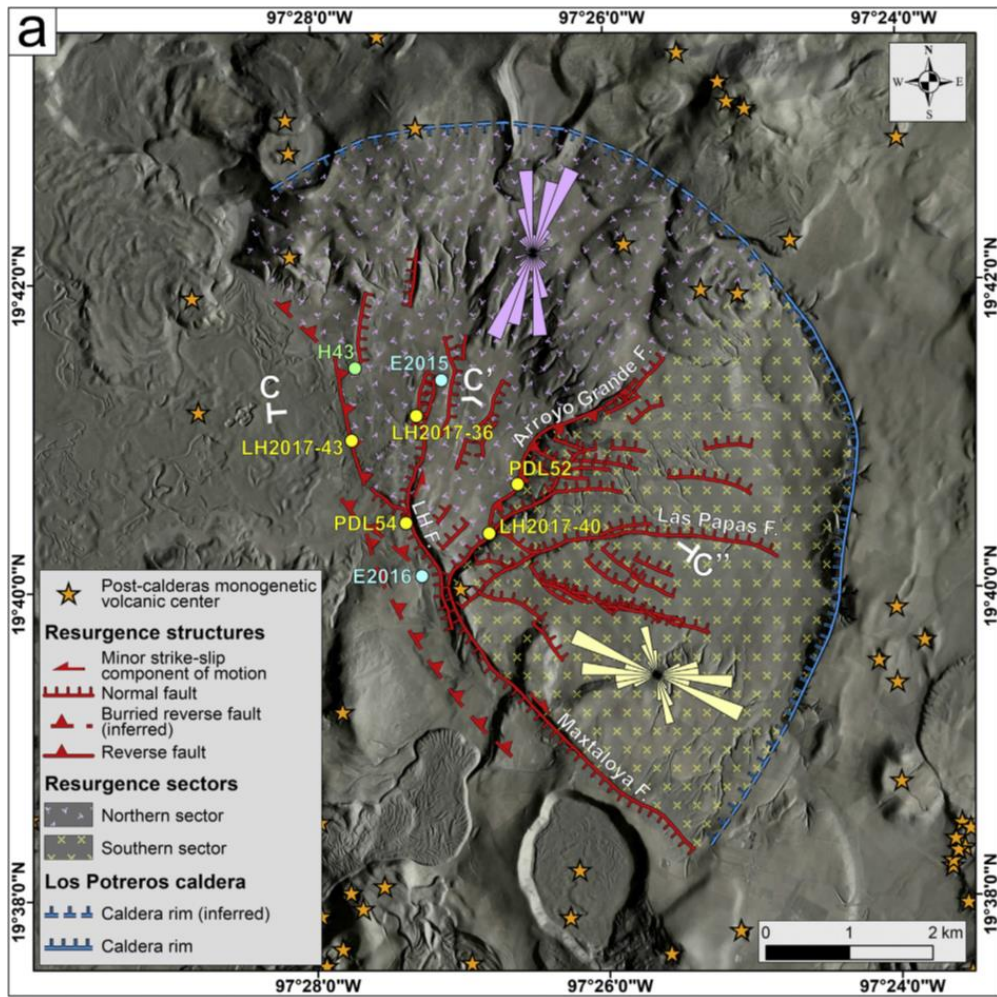
Figure 1.6. Main fault scarps observed within the Los Potreros Caldera together with the interpreted main structural sectors. Northern and southern sectors are interpreted as being related to a resurgent block (after Norini et al., 2019). LHF=Los Humeros fault.

It is worth noting that the minor faults within the Los Potreros Caldera branch-off at high angle from the main NW-striking Maxtaloya and Humeros faults, defining a sort of 'horse-tail pattern' (Fig. 1.6). Importantly, these faults represent the main target of geothermal exploration and production, and are inferred to delimit intra-caldera sectors with similar vertical uplift (Norini et al., 2015). Differential uplift among these blocks has been related to intra-caldera magma resurgence (Norini et al., 2015, 2019; Fig.1.6), which is

22

also suggested by the presence of subsurface rhyolitic domes that have been drilled by geothermal wells (see geological section in Fig. 1.4; Carrasco-Núñez et al., 2017a). Some studies suggest that the magma chamber – that is expectedly sourcing magma resurgence – is currently partly solidified, with present-day temperatures of the order of 600°-650°C (5 to 7–8 km depth; e.g., Verma, 1983, 2000).

1.3 Geological setting of the Acoculco caldera complex

Volcanic activity in the Acoculco caldera complex (Fig. 1.1) is characterized by calc-alkaline composition and ranges in age from Pliocene to Pleistocene (López-Hernández et al., 2009; Avellán et al., 2018; Sosa-Ceballos et al., 2018). Several episodes of volcanism have affected the Acoculco area, producing rhyolitic domes, fissure lava flows, cinder cones, and two large ignimbrite eruptions related to caldera collapse (López-Hernández et al., 2009; Avellán et al., 2018; García-Palomo et al., 2018). The older caldera structure is the 32 km-wide Tulancingo Caldera (3.0–2.7Ma), and the 18 km-wide Acoculco Caldera (1.7 and 0.24Ma) (López-Hernández et al., 2009). The youngest volcanic episode is related to extra-caldera volcanism lasting until 63 ka (Avellán et al., 2018). However, Avellán et al (2018) do not find evidence for the existence of the Tulancingo caldera.

Magmatic activity in the Acoculco caldera complex is structurally controlled by both NE- and NW-trending existing faults in the basement (López-Hernández et al., 2009; Avellán et al., 2018). These faults have been likely reactivated during caldera collapse. In particular, the north-western Acoculco caldera rim follows a NE-SE-trending fault (e.g., Avellán et al., 2018), and the trace of the south-western Acoculco caldera rim is controlled by a NW-SE-oriented fault (Fig. 1.7). Interestingly, also geothermal fluids moved preferentially along NW-SE-oriented faults, as suggested by geothermal alteration that dominantly develops along this fault trend (see Deliverable 4.1 of GEMex Project).
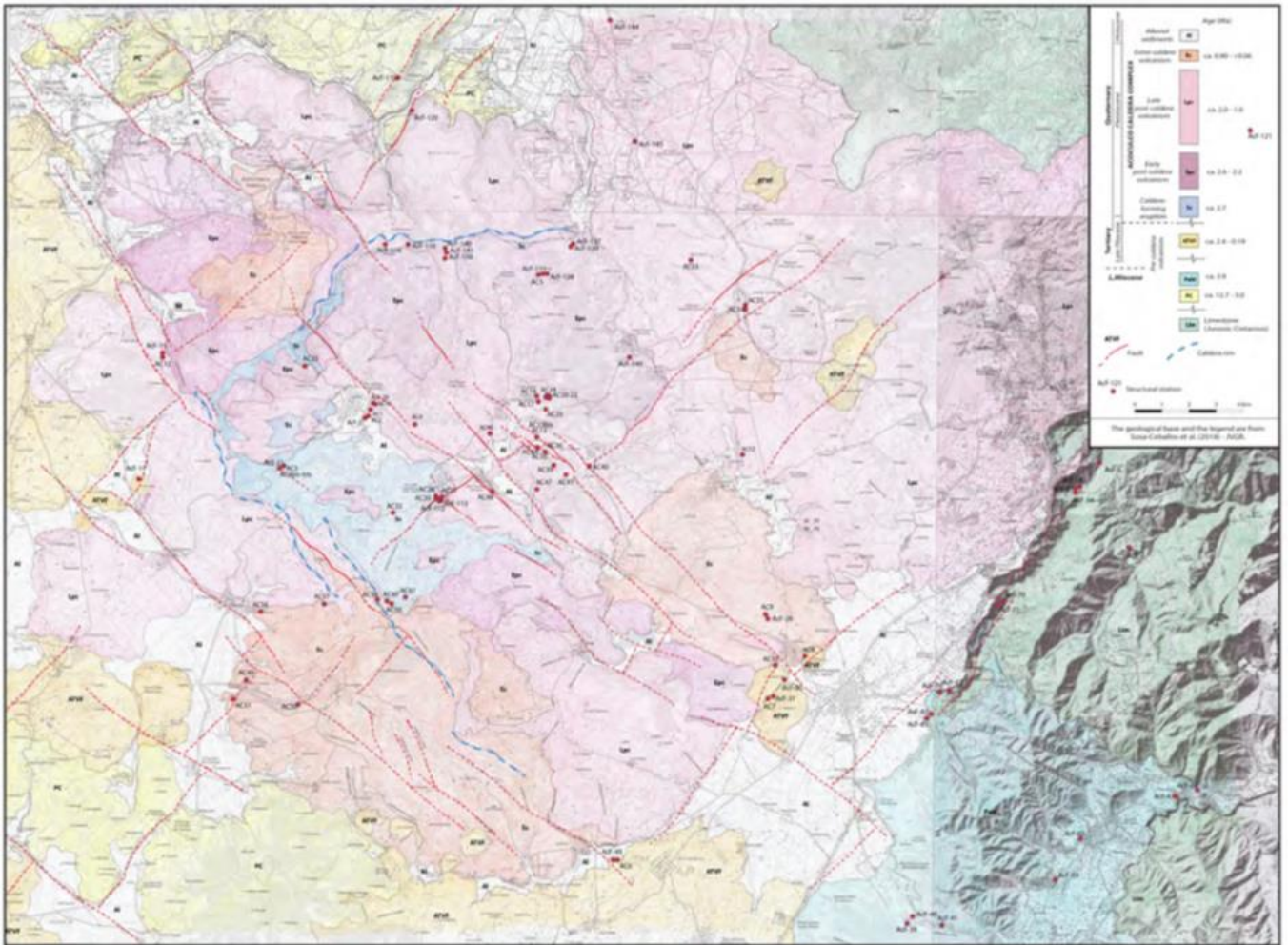
Figure 1.7. Geological map of the Acoculco caldera complex (modified from Sosa-Cabellos et al., 2018, with additional faults surveyed during the GEMex Project) (from Deliverable 4.1 of GEMex Project).

2 Analogue modelling of continental rifting and volcano-tectonic processes

2.1 Introduction on analogue modelling

Analogue modelling is an experimental procedure that allows to reproduce natural processes at a laboratory scale. This means that a model is not only smaller in dimension (property which, of course, is of great advantage for modellers) but that the complete development of the reproduced natural process is also concentrated in a reduced amount of time. This aspect provides the researcher the possibility to control -and monitor step by step- the evolution of a certain process, allowing for an in-depth analysis and comprehension of the mechanism that controls it in nature. Except for near-instantaneous events, generally the time involved in geological scale processes is largely out of the human monitoring possibilities, therefore analogue modelling is an extremely useful tool. This approach is nowadays well know and largely used in many branches of geology, and benefits from the input deriving from a large variety of data types (e.g. seismic data, geophysical, structural geology, stratigraphy, etc…). Geological information can be simplified in order to be used as "hard data" for model setup, or for comparison, once the models have been obtained. Of course, in order to furnish usable and well-sounded results, analogue models need to be quantitatively comparable with the reality of case studies, implying the achievement of correct *scaling* (Hubbert, 1937; Ramberg, 1981) of dimensions, physical properties of material, forces, as well as deformation time.

2.1.1 Short review of analogue modelling of rift propagation

Analogue models have been proven to represent powerful tools to analyse the process of continental rifting and the pattern/evolution of deformation resulting from stretching of continental plates. These models have been deformed either in an enhanced gravity field by using large capacity centrifuges or in the terrestrial gravity field (see Corti, 2012). In the centrifuge, models are thinned vertically and expand laterally in response to the centrifugal body force field, which plays the same role as gravity in natural geologic processes (Ramberg, 1981). Conversely, normal-gravity models extend by means of the pull of the motor-driven movement of basal (mostly crustal-scale models) or lateral (lithospheric-scale models) rigid plates. Several different parameters have been analyzed in previous modelling works, including: the dynamics of and the driving forces for extension (active vs. passive rifting; e.g., Mulugeta, 1985), the distribution of deformation and the resulting mode of rifting (e.g., Benes and Davy, 1996; Brun, 1999; Corti et al., 2003a; Michon and Merle, 2003; Corti, 2005), the cross-sectional evolution of faulting (e.g., Brun and Beslier, 1996; Michon and Merle, 2003; Nestola et al., 2013, 2015), the influence on the plan-view fault pattern of the kinematics of extension at crustal (e.g., Withjack and Jamison, 1986; Tron and Brun, 1991; Brun and Tron, 1993; Dauteuil and Brun, 1993; Clifton et al., 2000; Clifton and Schlische, 2001; McClay et al., 2002)

and lithospheric (e.g., Mart and Dauteuil, 2000; Corti, 2008; Agostini et al., 2009; Autin et al., 2010, 2013) scale, the role of multiphase extension (e.g., McClay and White, 1995; Bonini et al., 1997; Erbello et al., 2016), the presence and influence of pre-existing heterogeneities at crustal (e.g., Bellahsen and Daniel, 2005; Michon and Sokoutis, 2005; Corti et al., 2007) and lithospheric (e.g., Corti et al., 2003a; Corti and Manetti, 2006; Sokoutis et al., 2007) scale, the role of magmatism on extension-related structures (e.g., Callot et al., 2001, 2002; Corti et al., 2001, 2003b, 2004), the along-axis segmentation and the architecture of transfer zones (e.g., Elmohandes, 1981; Naylor et al., 1982, 1994; Serra and Nelson, 1988; Acocella et al., 1999, 2000; McClay et al., 2002; Corti, 2004; Zwaan et and Schreurs, 2018), the influence of rift width on the variation of extension direction between the rift axis and the margins (Sani et al., 2019), the influence of surface processes (erosion/sedimentation) on rift evolution (e.g., Corti et al., 2013; Zwaan et al., 2018). Recent models have also analysed in detail the process of rift propagation at both crustal and lithospheric (Molnar et al., 2018) scale. In these models, rift propagation is induced by motor-driven rotational extension of lateral plates about a pivot; in some of these models, the influence of pre-existing heterogeneities at different angles with respect to the direction of extension is investigated (Molnar et al., 2018; Fig. 2.1).
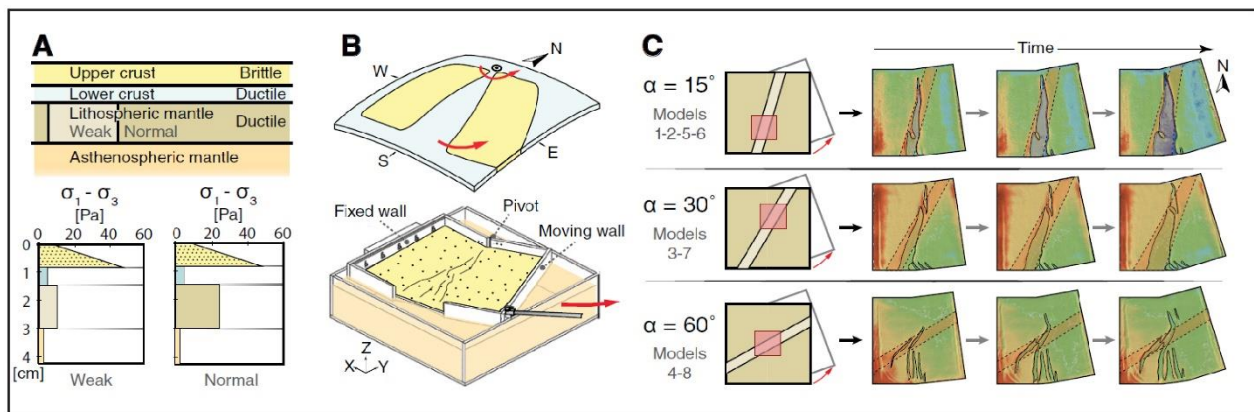
Figure 2.1. Analogue modelling setup and results from Molnar et al. (2018) showing a rotational-rift setup similar to what we have adopted for our modelling strategy; .α is the angle of a pre-existing lithospheric heterogeneity with respect to general rift propagation direction.

2.1.2 Short review of analogue modelling of caldera collapse

In this paragraph we report a brief summary of the large amount of work that has been done during the last decades about caldera collapse and resurgence, in order to provide the reader with a general background to understand our modelling. For an in-depth description of caldera collapse modelling we suggest the reader to refer to the recent reviews by Geyer and Martí (2014) and Acocella (2007; Fig. 2.2). The majority of analogue models involving caldera collapse processes can be generally classified into those applying overpressure and underpressure mechanisms, respectively. The first mechanism implies the increase of pressure inside the magmatic chamber, inducing doming at surface and consequent stretching due to tensile

stress that is likely responsible for caldera collapse initiation (e.g., Gudmundsson, 1988, 2015, 2016; Gudmundsson et al., 1997; Burov and Guillou-Frottier, 1999; Guillou-Frottier et al., 2000). The second mechanism indicates the drop of pressure inside the magmatic chamber due to magma eruption as the driving mechanism for caldera collapse initiation (e.g., Williams, 1941; Druitt and Sparks, 1984; Lipman, 1997). In both models, the complex behavior of the system has been simplified to approximate a purely mechanical deformation. On the other hand, the large amount of experimental work done on this issue demonstrates the reliability of this kind of modeling.

In this frame, various modelling approaches have been applied since the '80. Komuro et al. (1984) modelled caldera collapse applying the overpressure mechanism by pushing a rigid sphere inside granular material, obtaining radial cracking of the resulting dome due to surface tensile stress. Many authors followed the same overpressure approach by intruding a viscous material (e.g., silicone) in a brittle layering or by inflating a balloon placed at the base of granular material (Martì et al., 1994; Walter and Troll, 2001; Acocella et al., 2001a; Troll et al., 2002; Acocella and Mulugeta, 2002). Underpressure mechanisms made large use of various silicones sinking into sand layers, or balloon deflating into brittle materials (e.g., sand, floor). This approach is so far the most applied to reproduce caldera collapse processes (Komuro, 1987; Martì et al., 1994; Roche et al., 2000; Acocella et al., 2000; 2001b; Walter and Troll, 2001; Troll et al., 2002; Kennedy et al., 2004; Lavallée et al., 2004; Geyer et al., 2006), as it offers easiness of the modelling procedure and reproducibility of results. Analogue models using the underpressure mechanism have been also used to investigate the role of regional stress and inherited structures on caldera collapse evolution (e.g., Cailleau et al., 2003; Acocella et al., 2004; Holohan et al., 2005, 2008, 2013).

Category of experiment	Analogue modelling study	Materials+apparatus	Main results
Overpressure	Komuro et al. (1984)	Rigid sphere rising in powder	Radial+concentric fractures with depression on crest of dome
	Martì et al. (1994)	Balloon inflated in powder	Outward dipping reverse faults and crestal normal faults
	Walter and Troll (2001)	Balloon inflation in flour	Subsidence of crest of dome with normal faults
	Acocella et al. (2001a)	Silicone intruding in sand	Doming, crestal thinning and depression
	Troll et al. (2002)	Balloon inflation in flour	Formation of piecemeal collapses
	Acocella and Mulugeta (2002)	Silicone rising below sand (centrifuge)	Doming, crestal depression bordered by inward dipping normal faults
Underpressure	Komuro (1987)	Dry ice evaporating in powder	Outward dipping reverse faults
	Martì et al. (1994)	Balloon in powder	Outward dipping reverse faults+subvertical faults
	Roche et al. (2000)	Silicone sinking in sand	Outward dipping reverse faults+inward dipping normal faults
			Role of root aspect ratio
			Independence from the reservoir shape
	Acocella et al. (2000)	Silicone sinking in sand	Outward dipping reverse faults+inward dipping normal faults
			Room problem
	Acocella et al. (2001b)	Silicone sinking in sand	Constant architecture of nested calderas
	Walter and Troll (2001)	Balloon deflating in flour	Outward dipping reverse faults+inward dipping normal faults
	Troll et al. (2002)	Balloon deflating in flour	Piecemeal calderas through inflation-deflation cycles
	Kennedy et al. (2004)	Balloon deflating in sand	Reverse faults+normal faults controlled by the shape of chamber roof
	Lavallèe et al. (2004)	Balloon deflating in sand (topography–cones)	Topography may locally vary the shape of calderas
	Geyer et al. (2006)	Balloon in sand	Roof aspect ratio and magma chamber withdrawal
Regional stress	Cailleau et al. (2003)	Balloon deflating in flour (regional stress)	Caldera elongated accordingly with the regional stress
	Acocella et al. (2004)	Silicone sinking in sand (regional pre-existing faults)	Caldera elongation may depend on regional fault reactivation
	Holohan et al. (2005)	Balloon deflating in sand (regional stress)	Elongation of calderas parallel to minimum compression

Figure 2.2. Table summarizing materials, methods and main findings of several works investigating caldera collapse processes (after Acocella, 2007).

Among specific results, all these analogue models pointed to general agreement about the first-order characteristics of the process. Acocella (2007) proposed a model for caldera collapse implying the formation of outward-dipping reverse faults followed by the development of inward-dipping normal faults (Fig. 2.3).

In detail, once the magma chamber experienced underpressure (likely due to magma eruption or depletion induced by magma migration) a first stage (Fig. 2.3a) involving down-sagging at surface, implies inward tilting of the incipient caldera boundaries, followed by a second stage (Fig. 2.3b) of outward-dipping reverse fault development. In a third stage (Fig. 2.3c) the down-sagging migrates in the peripheral area around the collapsing caldera, to afterward develop (fourth stage; Fig. 2.3d) inward-dipping normal faults. This model of evolution is largely accepted and constitutes a starting point for our modelling and investigation.
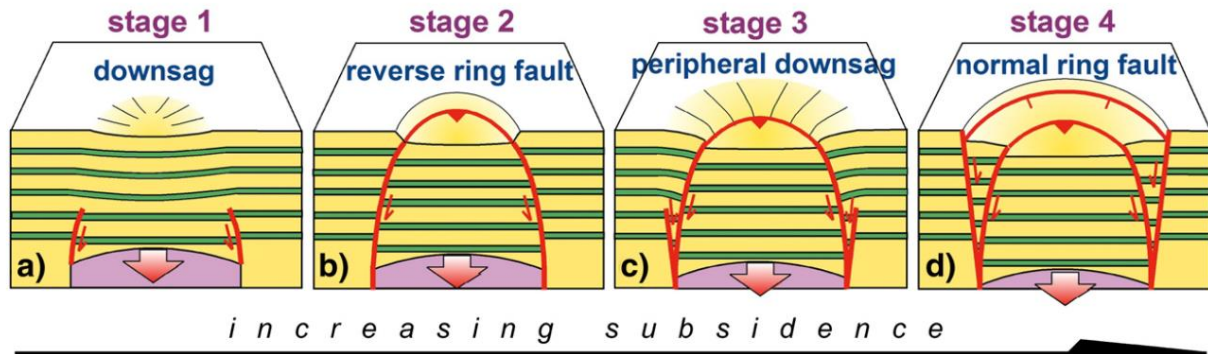
Figure 2.3. Evolutionary model for caldera collapse development, as proposed by Acocella (2007). Stages 1 to 4 describe the formation of incipient caldera to mature collapse through the formation of early outward-dipping reverse faults and subsequent inward-dipping normal faults.

2.2 Modelling strategy

In the following two chapters we describe the modelling strategy adopted to investigate the tectonic evolution of Los Humeros and Acoculco volcanic complexes at two different scales. In a first modelling series (*named D3.5-1: Relationships between a propagating rift and existing crustal faults*) we investigate the study areas at a large scale, speculating on the possible role of reactivated regional structures on fluid migration. The main goal is to test whether pre-existent structures in the area of Acoculco and Los Humeros might be reactivated - and therefore likely be possible preferential paths for fluid migration - by the propagation of rift-related deformation associated with the TMVB. The rationale of our modelling is explained in detail in paragraph section 2.2.1. In section 2.2.2 we describe the modelling strategy of a second experimental series (named *D3.5-2: Role of pre-existing discontinuities within the brittle overburden in caldera collapse process*), which focuses on the role that pre-existing discontinuities might have played at the local scale in the collapse of the Acoculco and Los Humeros calderas, reproducing in detail these volcano-tectonic processes.

2.2.1 Series D3.5-1: Relationships between a propagating rift and existing crustal faults

The aim of the models belonging to Series D3.5-1 "*Relationships between a propagating rift and existing crustal faults*" was to test whether a propagating rift is influenced by - or may influence the reactivation of - inherited fabrics. The hint for this study was given by the necessity to investigate both the role of tectonics inheritance and active tectonics on specific areas of the TMVB (Fig. 2.4a). Its genesis is strictly related to the interaction between the subducting Rivera and Cocos plates and the North America plate, as the eastward propagation of volcanism is considered to be associated with slab detachment, and consequent asthenosphere

upwelling (Fig. 2.4b; e.g., Ferrari, 2004). The progressive ESE-directed tearing of the slab and the consequent detachment are hypothesised to cause crustal extension propagating in the same direction (Fig. 2.4b, c).
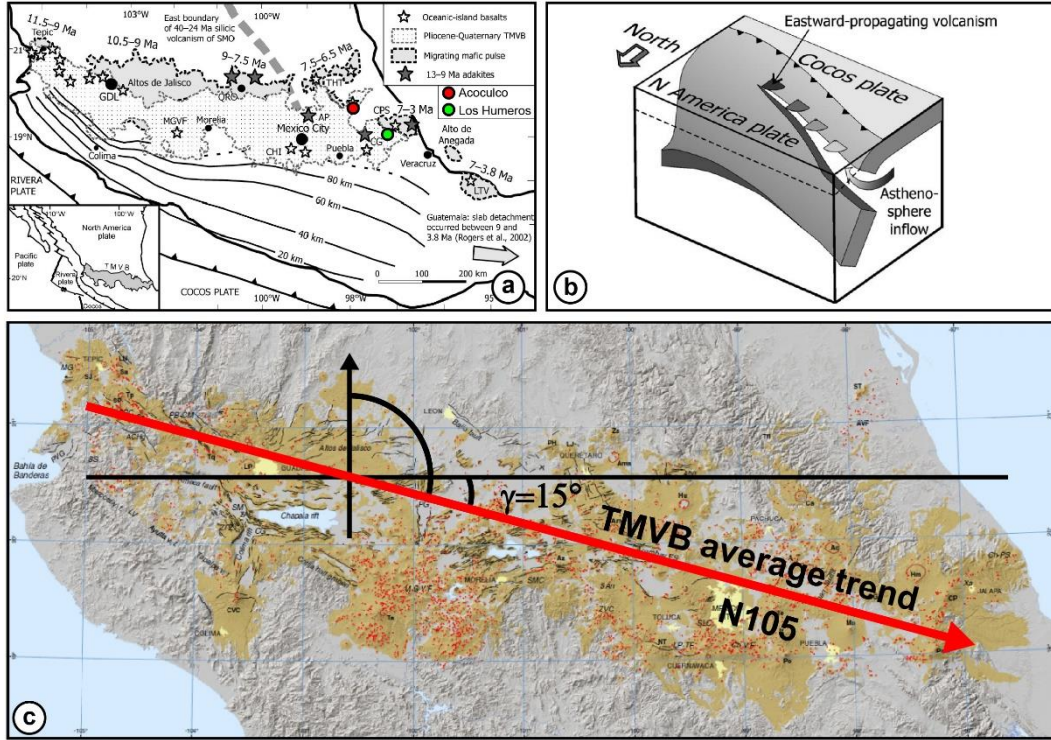
Figure 2.4. (a) The Trans Mexican Volcanic Belt (TMVB) extends for about 1000 km through Mexico, trending WNW-ESE. Locations of Acoculco and Los Humeros volcanic complex, target of geothermal exploration, are indicated (modified from Ferrari, 2004). (b) The TMVB is interpreted to derive from interaction between Cocos and North America plates, inducing slab detachment leading to surface extension and magma emplacement (modified from Ferrari, 2004). (c) The average trend direction of the TMVB is about N105°, interpreted as the direction of rift propagation resulting from crustal extension. This direction makes an angle (γ) of 15° to the E-W direction. Angle γ was used to "normalize" the azimuth of natural structures to an arbitrary North in our models (taken as the orthogonal to the rift propagation direction).

In this context, the TMVB developed several large scale volcanoes and calderas, some of which are the target of geothermal exploration (e.g., the Los Humeros and Acoculco volcanic complexes; Fig. 2.4a).

In the frame of the GEMex Europe-Mexico cooperation project, we aimed to investigate the interplay between the hypothesized propagating rift and inherited crustal fabrics. Particularly, in the easternmost part of the TMVB, where the GEMex Project is focusing its investigation, the inherited fabric is represented by ca. NE-SW and NW-SE regional faults (Fig., 2.5; e.g., Campos-Enriquez & Garduño-Monroy, 1987; Carrasco-Núñez et al., 2017b; García-Palomo et al., 2018; Avellán et al., 2018). These structures may have had a role in the emplacements of volcanic centres, thus being important players in the geothermal investigation processes. We addressed this issue through analogue models, which reproduced continental-scale rift propagation in order to evaluate if and how the inherited structures may interact or reactivate during

30

the rifting. According to the above mentioned authors, in the area of Acoculco, these structures show two main trends striking N40° and N150°, respectively. These trends are similar to those in Los Humeros area, where regional structures strike N40°-N50° and N130°. On average, we can consider for our modelling purpose two mean trends: a first set (indicated as S1) trending N45°and a second set (S2) striking N140°. These measures have been used in our models after an angular correction, in order to fit with the modelled orientation of rift propagation direction, as follows:

$$Av_M = Av_N - \gamma$$

Where Av_M is the average trend of the structures that we aim to reproduce in the models, Av_N is the average trend in nature (see Fig. 2.5) and $\gamma = 15°$ is an angle correction corresponding to the angle between the actual North and the direction of propagation of the TMVB (see Fig. 2.4c). Therefore, in our models we have used Av_M trends for S1 and S2 of:

$$Av_M \, S1 = 45° - 15° = 30°$$

$$Av_M \, S2 = 140° - 15° = 125°$$
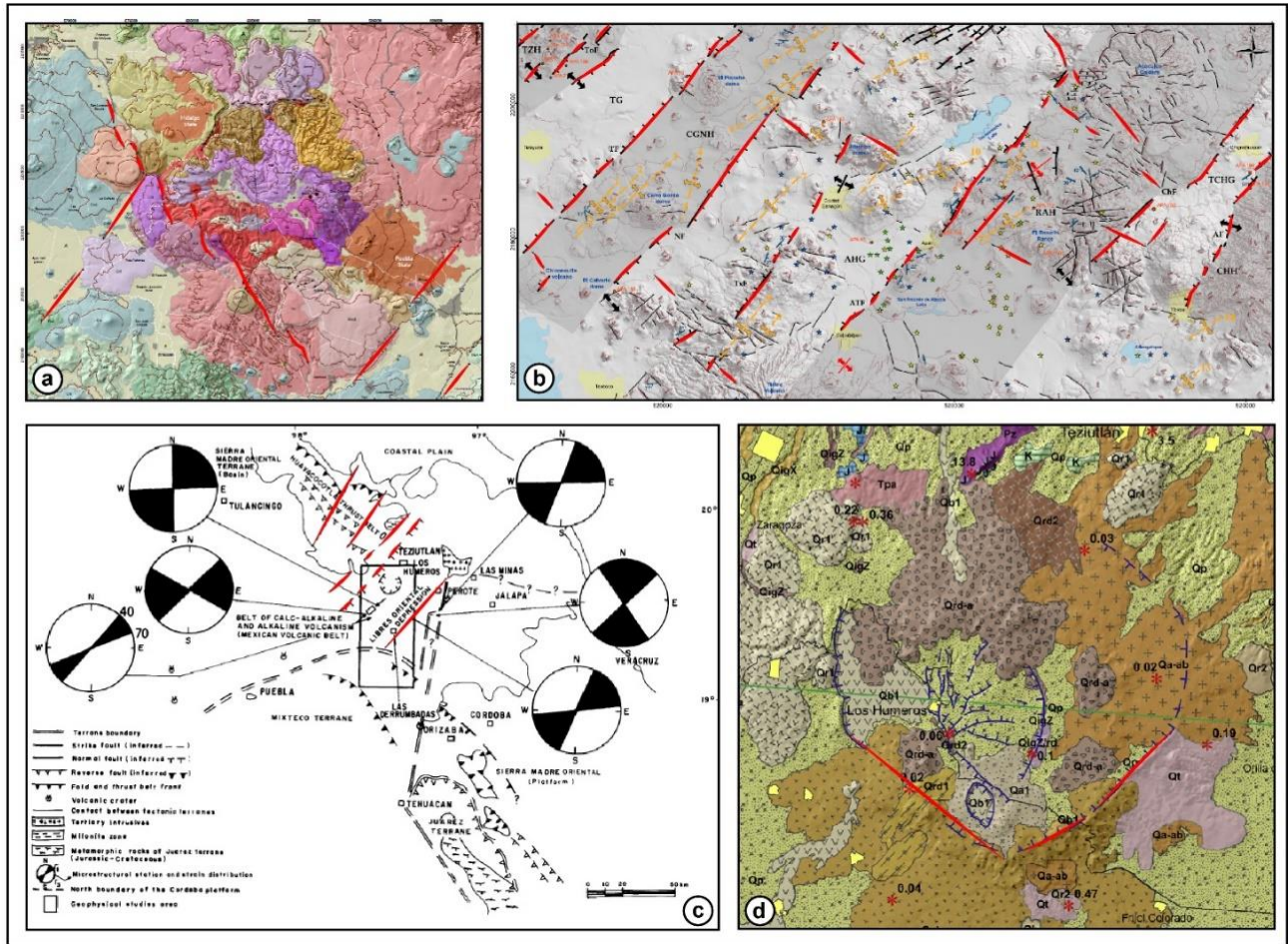
Figure 2.5. (a) Geological map showing the main structural inherited trends at the Acoculco caldera complex (modified from Avellán et al., 2018). (b) Structural sketch of the Acoculco region, highlights the main structural inherited fabrics (from García-Palomo et al., 2018). (c) Structural sketch reporting inherited fabrics in the Los Humeros area (modified from Campos-Enriquez & Garduño-Monroy (1987). (d) Detailed geological map of the Los Humeros-Los Potreros caldera showing the main structural features (Carrasco-Núñez et al., 2017b). Some of these faults are interpreted by fieldwork of Work Package 4 (WP4; Liotta and WP4 Working Group, 2019) as inherited regional structures. In red (a, b, c, d) are indicated the regional structures of interest.

Furthermore, to better understand any possible mutual relationship between rift propagation and inherited fabrics, we have varied the orientation of discontinuities. Besides the specific case of the TMVB, relations between propagating rift and inherited fabrics can be generalized also to other sites worldwide.

2.2.2 Series D3.5-2: Role of pre-existing discontinuities within the brittle overburden in caldera collapse process

Caldera collapse processes and tectonics may be strictly related. This is likely the case of the Los Humeros and Acoculco volcanic systems. The fieldwork of Work Package 4 (WP4; Liotta and WP4 Working Group, 2019) and other studies (Campos-Enriquez & Garduño-Monroy, 1987; López-Hernández al., 2009; Carrasco-Núñez et al., 2017b; García-Palomo et al., 2018; Avellán et al., 2018) have highlighted the possible presence of several inherited structures (outside the caldera and possibly inside; Fig. 2.5 and Fig. 2.6) that might have had a role in controlling or influencing the caldera collapse processes at both sites.
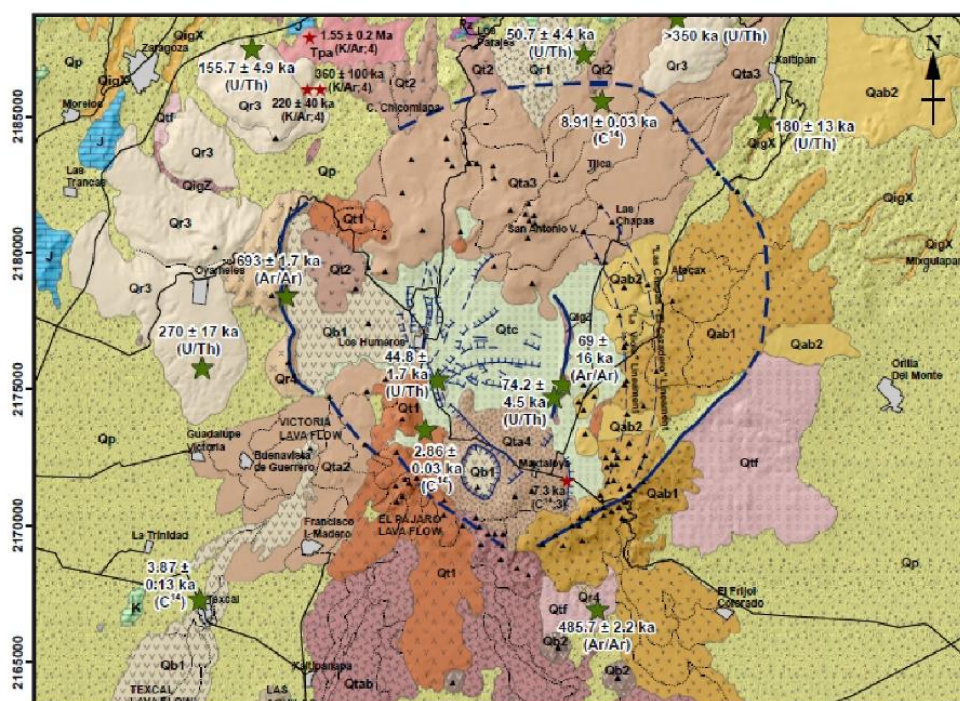
Figure 2.6. Geological map of Los Humeros showing caldera rectilinear ring fault at the south-western and south-eastern margins (from Carrasco-Núñez et al., 2017b).

This experimental series D3.5-2 aims to test the role of tectonics on caldera collapse processes. We have performed a total of 18 models (Model-20 to Model-30, Model-32, and Model-35 to Model-40), of which 16 are shown here. We have tested the role of inherited structures on caldera collapse processes by introducing in model setup artificial discontinuities either in the substrate (referred herein to as the rocks hosting the magma reservoir) or the overburden (or both at the same time). Note that models testing the role of discontinuities are also present in other experimental series (particularly Deliverable 3.6, focusing on volcano collapse and caldera resurgence). In general, we have simulated discontinuities with two different approaches.

The first approach aims to simulate an analogue magma chamber delimited by one or two fault discontinuities. Therefore, we have designed the magma chamber with rectilinear sides (Fig. 2.7), and the dip angle of the discontinuity bounding the analogue magma was vertical 90° or dipping 60°, with the latter simulating inward or outward dipping faults.
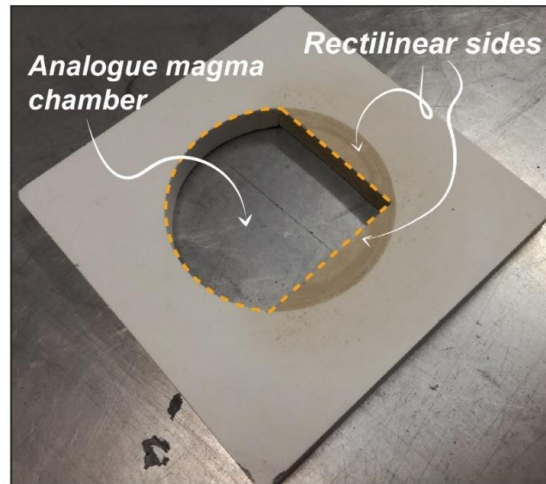
Figure 2.7. Setup employed in Series D3.5-2 to simulate the analogue magma chamber. In this specific case, the chamber had two rectilinear sides that were introduced to modify the circular shape of the standard analogue magma chamber. These two straight sides simulated the inherited fault structures that may have influenced the caldera collapse process. Alternatively, we used a single rectilinear side or a 60°-dipping one simulating different inherited fault attitudes.

The second approach created artificial discontinuities in the brittle overburden, simulated by a granular material. In particular, a "discontinuity apparatus" (DA; Fig. 2.8) consisting of a gliding and reclinable knife allowed us to "cut" into the sand creating weak discontinuities zones. Depending on setup necessities, we coupled these two approaches to create a discontinuity developing from the substrate up to the surface (or terminating at a defined depth below it). A combination of discontinuities was thus tested in the various models to investigate the possible role of a specific discontinuity in natural caldera collapse processes.
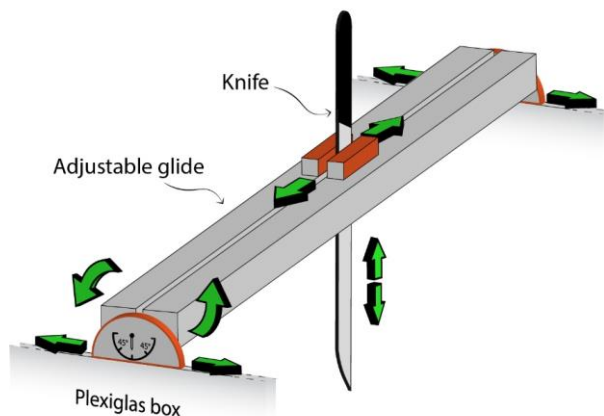
Figure 2.8. Sketch of the "discontinuity apparatus" (DA) employed to perform artificial discontinuities inside the brittle overburden in models of Series D3.5-2 (and D3.5-1 as well). The gliding knife is adjustable in terms of depth and angle of cutting to simulate vertical and 60°-dipping discontinuities.

2.3 Analogue modelling procedure of Series D3.5-1

2.3.1 Series D3.5-1: Material, setup and scaling

The modelling apparatus (Fig. 2.9 and Fig. 2.10) is composed of two moving plates (MP) fixed at their external tips by poles of rotation that allowed the progressive opening and consequent rift propagation (Fig. 2.9a, b). The movement has been obtained by dragging the plates with two undeformable cables, fasten to a stepped-motor. A linear velocity of 20 mm/h was applied in the direction of rift propagation, which corresponds to a maximum velocity opening between the two plates of 10 mm/h, measured at the left-lateral limit of the moving plates (see red dot in Fig. 2.9).
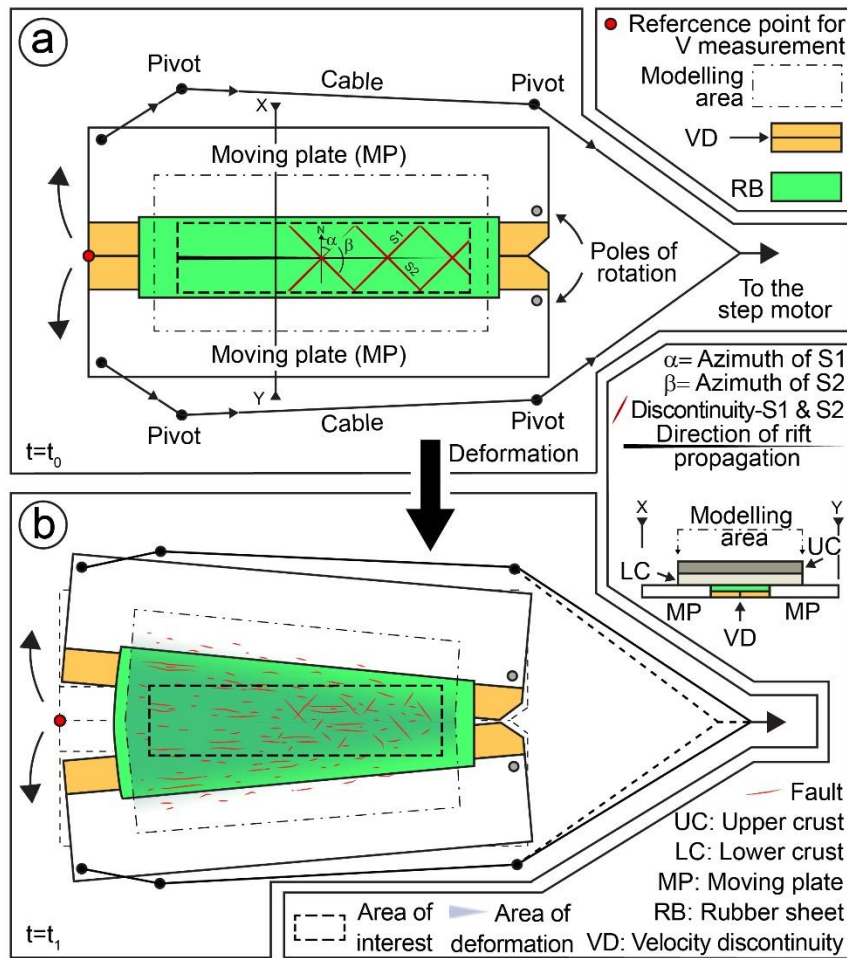
Figure 2.9. Schematic cartoon of the modelling apparatus. (a) Top-view setting of the undeformed model; note that analogue materials are not represented in this sketch, but correspond to the modelling area (dashed rectangle). Two moving plates are fixed at their tips and moved by two cables fasten to a step-motor, in order to obtain a progressive rotational opening. A rubber sheet (RB; green rectangle) was placed above the velocity discontinuity (VD; orange polygons) to distribute the deformation. The modelling area was overlain by a 1 cm-thick PDMS-corundum mixture mimicking a lower crust (LC) and by a 1 cm-thick sand mixture simulating the brittle upper crust (UC). The UC was variously cut with a gliding knife (discontinuity apparatus; DA) to simulate inherited fabrics. These inherited structures (one or two sets; S1 and S2) were placed at defined angles to an arbitrary 'model North' (N), which is orthogonal to the axis of rift propagation (Tab. 2). (b) Top-view setting showing rotational opening imposed to the model and differential strain along the rift axis.
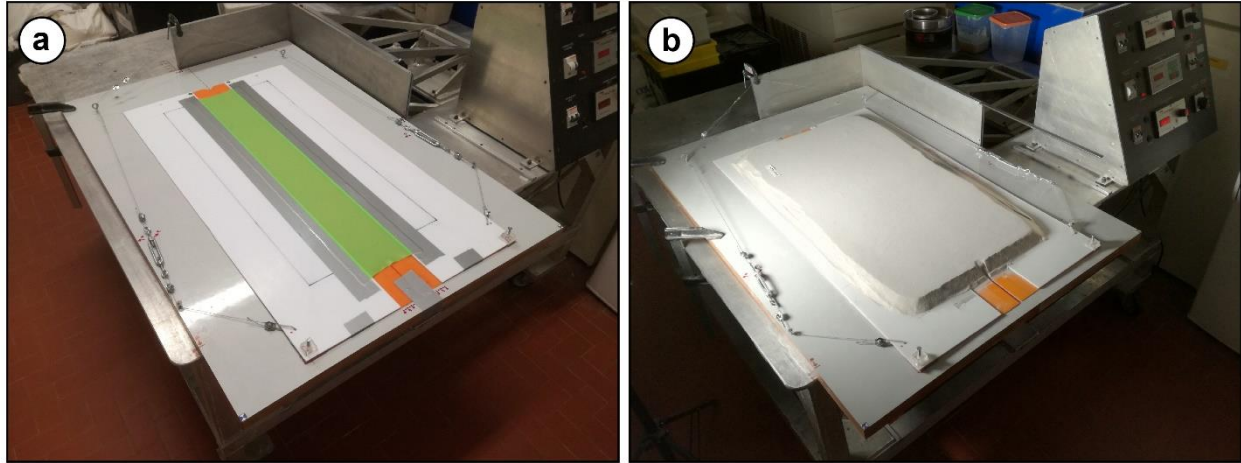
Figure 2.10. Modelling apparatus for series D3.5-1. (a) The biaxial deformation machine ('TOSI' machine) with the modelling apparatus. (b) Same apparatus with a model built, and deforming, on top of it.

Due to the rotational MP movement, the velocity gradually decreased toward the poles of rotation along the propagating rift axis. The boundary dividing the MP generated a velocity discontinuity (VD), which effect was limited by the employ of an elastic rubber sheet (RB; green rectangle in Fig. 2.9a). Stretching of the rubber sheet allowed distribution of deformation and avoided the formation of faults with unrealistic length in correspondence of the VD. The area of interest of each model corresponded to the central portion of the RB, where boundary effects were minimized. To address this aspect, the actual modelling area was kept larger, the area being extended for about 10 cm on both RB sides (Fig. 2.9). The analogue materials used to build the models were placed on this portion of the modelling apparatus. All material properties are listed in Table 1. We simulated the Upper Crust (UC) using a 1 cm-thick layer of Quartz and K-feldspar sand mixture (80:20 proportion % in weight; see Montanari et al., 2017a) (Fig. 2.9a,b). The physical properties (i.e. density, angle of internal friction) of this sand mixture correctly scale to natural rocks and allow to realistically reproduce fault structures (both in plain view and cross section; i.e. fault elongation and fault dip angle). Due to the scale of these models, this mixture resulted to mimic better fault geometry than the standard 70:30 Qz-Kfeldspar mixture codified in Montanari et al. (2017a). The Lower Crust (LC) was simulated by using a 1 cm-thick layer of Polydimethylsiloxane (PDMS) mixed with corundum powder (Tab. 1). The total thickness of models (LC+UC) was 2 cm, for a modelling area of about 7 0x 35 cm and a limited area of interest of about 65 x 15 cm.

Models were scaled to achieve a correct geometric, dynamic, rheological and kinematic similarity (Hubbert, 1937; Ramberg, 1981) (Tab. 1). Specifically, length and thickness (geometrical similarity) of models were scaled using a scaling ratio (defined as $l^*=l_{model}/l_{nature}$ and $h^*=h_{model}/h_{nature}$) of 6.67×10^{-6}, such that 1 cm in the model corresponds to 15 km in nature. The modelling procedure was developed in normal gravity, so that the gravity scaling ratio (g^*) between the model and nature was equal to 1. The density of mixture of granular

36

material (Quartz and K-feldspar) and silicone and Corundum (1440 kg m^{-3}) implied a density scaling ratio ($\rho*$) of 0.53, considering a natural rock density of ~2700 kg m^{-3} leading to a stress scaling ratio ($\sigma*=\rho*g* l*$) of 3.53×10^{-6}. The coefficient of internal friction (μ) requires to be similar both in the analogue material and the natural rock, implying a $\mu*\sim 1$. In order to obtain dynamic scaling of models, cohesion ratio (c*) needs to equal the stress ratio ($\sigma*=c*$), a condition that is correctly fulfilled having c* and $\sigma*$ the same order of magnitude (10^{-6}).

Scaling of the ductile layer simulating the LC, implies the consideration of both viscosity and the strain rate. The LC was simulated with a mixture of PDMS and corundum sand. Being this a non-standard experimental material, density and viscosity need to be determined in order to guarantee the correct scaling. Corundum was added to PDMS in a quantity that allow to reach the correct density value of 1440 kg m^{-3}. In order to obtain a proper density of the PDMS-corundum mixture comparable with the scaled density of the LC and UC (1440 kg m^{-3}), we empirically calculated a proportion of PDMS-Corundum of ~1:1 % in weight. Viscosity of this material was then calculated using a coni-cylinder viscometer apparatus (Fig. 2.11) available at the Tectonic Modelling Laboratory of IGG-CNR Firenze.
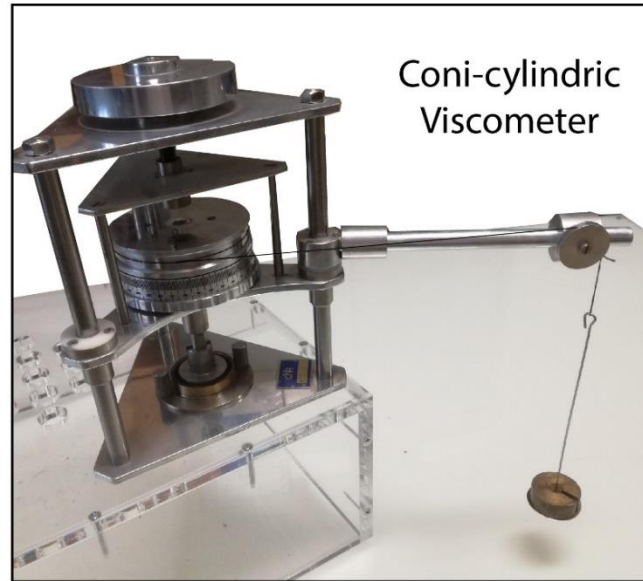
Figure 2.11. Coni-cylindric viscometer available at Tectonic Modelling Laboratory (IGG-CNR Firenze) used to measure the viscosity of the PDMS+corundum mixture.

Through progressive steps, we calculated the shear-stress vs. strain rate curve for the PDMS-corundum material (Fig. 2.12). We obtained the following equation using regression line (R^2=0.99):

$$Y=2\times10^{-6} X^{1.24}$$

where Y=$\dot{\varepsilon}$ (being ε the strain rate) and X=τ (τ being the shear stress):

$$\dot{\varepsilon} = 2\text{x}10^{-6}\, \tau^{1.24}$$

For a Newtonian material:

$$\dot{\varepsilon} = \sigma\eta$$

while for a non-Newtonian material

$$\dot{\varepsilon} = A\,(\sigma)^n$$

The material is Newtonian for n = 1, while for n > 1 the material is power-law (strain-rate softening). Besides, an n < 1 denotes a strain-rate hardening material (Weijermars, 1997).

Since in our case n = 1.24 we can assume the PDMS+corundum as a near-Newtonian material. Viscosity is therefore extrapolated at strain rate of the model ($\dot{\varepsilon}_{mod}$) according to the following equations:

$$\eta = \tau / \dot{\varepsilon}_{mod}$$

$$\dot{\varepsilon}_{mod} = 2\text{x}10^{-6}\, \tau^{1.24}$$

$\dot{\varepsilon}_{mod}$ was directly calculated from our models. We calculated the maximum $\dot{\varepsilon}_{mod}$ considering the linear deformation and the velocity at the left-lateral side of our model setup (see Fig. 2.9).
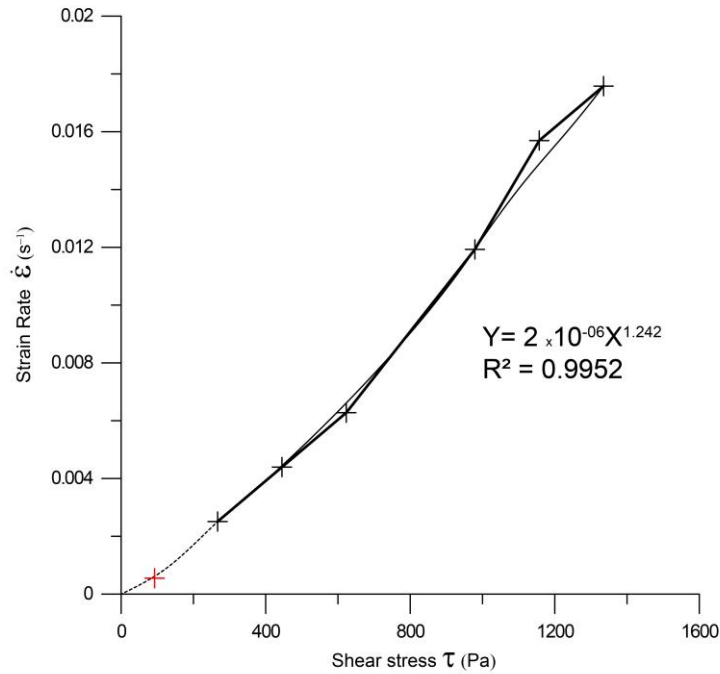
Figure 2.12. Graph showing the strain rate vs. shear stress curve for the used mixture of PDMS+corundum obtained using the coni-cylinder viscometer, from which was extrapolated the density value (red cross) at experimental strain rates.

Considering the maximum engineering strain rate, $\dot{\varepsilon}_{mod}$ can be calculated as follow:

$$\dot{\varepsilon}_{mod}= d/t*h$$

where d is the final length between the corners of the moving plates, t is the cumulative time of deformation and h the thickness of the viscous layer. Modelling parameters are as follow:

- d=0.08 m, representing the maximum opening of the moving plate reached during deformation at the left-lateral side of the model
- t=14400 s, representing the maximum time interval of deformation
- h=0.01 m, representing the thickness of the PDMS+corundum layer simulating the LC. From this follows:

$$\dot{\varepsilon}_{mod}=0.08/14400 \times 0.01= 5.55 \times 10^{-4}\,\text{s}^{-1}$$

We can now extrapolate τ from the following equation:

$$\dot{\varepsilon}_{mod} =2 \times 10^{-6}\,\tau^{1.24}$$

$$5.55 \times 10^{-4}=2 \times 10^{-6}\,\tau^{1.24}$$

$$\tau=92.73\ \text{Pa}$$

We have therefore obtained a value of effective viscosity η_m for the model of:

$$\eta_m= \tau / \dot{\varepsilon}_{mod} = 92.73/5.55 \times 10^{-4} =1.69 \times 10^{5}\ \text{Pa s}$$

Assuming prototype viscosity values η_n of the lower continental crust in the range 10^{20} and 10^{24} Pa s (e.g. Weijermars, 1997), and model viscosity $\eta_m =1.69 \times 10^{5}$ Pa, viscosity ratio η^* ranges from 1.69×10^{-15} up to 1.69×10^{-19}. One can thus obtain $\dot{\varepsilon}^*$ from $\dot{\varepsilon}^*=\sigma^*/\eta^*$, such that ε^* ranges from 2.1×10^{10} to 2.1×10^{14}. Following Merle and Abidi (1995), the horizontal displacement rate $v^*= v_m /v_n$ is given by the product of ε^* and l^*, such that an average viscosity of 10^{22} Pa s corresponds to a natural extension rate of $v_n \approx 12.5$ mm yr^{-1} (Table 2-1).

Dynamic similarity of the viscous layer can be effectively defined by the dimensionless ratio R_m of gravitational to viscous forces (Ramberg, 1981), termed 'Ramberg number' (R_m) by Weijermars and Schmeling (1986):

$$R_m = \frac{F_g}{F_v} = \frac{\rho_d g z_d}{\eta \dot{\varepsilon}} = \frac{\rho_d g z_d^2}{\eta v},$$

where ρ_d and z_d are the density and thickness of the ductile layer, g is the gravitational acceleration, η is the viscosity, $\dot{\varepsilon}$ is the strain rate given by the ratio between the velocity v and the thickness of the ductile layer. In nature, R_m can be estimated to be about 1.6 (considering ρ_n = 2900 kg m^3, g = 9.81 m s^{-2}, h = 15 km, η_n = 10^{22} Pa s, and v_n=12.5 mm yr^{-1}), while in the model R_m can be estimated at 1.5 (considering ρ_m = 1440 kg m^3, g = 9.81 m s^{-2}, h = 0.01 m, η_m = 1.69x10^5 Pa s, and v_m=20 mm hr^{-1}; Table 2-1).

Dynamic similarity of the brittle layer can be estimated using the ratio S_m of gravitational to frictional forces in model and nature (Corti et al., 2003b), which is essentially equivalent to the Smoluchowsky number (S_m) defined by Ramberg (1981):

$$S_m = \frac{F_g}{F_f} = \frac{\rho_b g z_b}{\mu \rho_b g z_b + c_0} \ ,$$

where ρ_b and z_b are the density and thickness of the brittle layer, g is the gravitational acceleration, c is the cohesion, and μ is the internal friction coefficient. In nature, S_m can be estimated to be about 1.6 (considering ρ_n = 2700 kg m^3, g = 9.81 m s^2, μ = 0.6, h = 15 km, and $c_o \approx 10^7$ Pa), while in the model S_m can be estimated at ~1.5 (considering ρ_n = 1440 kg m^3, g = 9.81 m s^{-2}, μ = 0.6, h = 0.01 m, and $c_o \approx$ 6 Pa; Table 2-1). Since both nature and series D3.5-1 models share very similar R_m and S_m numbers, the requirement of dynamic similarity is fulfilled.

The Reynolds number, R_e is another adimensional number (ratio of inertial to viscous forces) relevant for the modelling, which is given as (Ramberg, 1981, notations as above):

$$R_e = \frac{F_i}{F_v} = \frac{\rho v z_d}{\eta}$$

However, R_e numbers cannot be equivalent in model and nature, even though a dynamic similarity with natural conditions can be obtained for analogue models deformed under a natural gravitational field whether $R_e \ll 1$ and inertial forces can be considered as negligible, which leads to the 'quasi-static' approximation (Hubbert, 1937; Ramberg, 1981). More specifically, the not strict equivalence of Reynolds numbers in model and nature can be disregarded when inertias are negligible, that is when (Ramberg, 1981) 'acceleration, in terms of rate of change of velocity, but certainly not in terms of force per unit mass in a body-force field, of most tectonic processes is negligible except, for example, in earthquakes'. R_e estimated for our models of series D3.5-1 yields a value of 4.7 x 10^{-10}, which is enough small to fulfil the quasi-static' approximation.

	Parameter	Model	Nature	Model/Nature ratio
PDMS-Corundum (~ 1:1 % in weight) (simulates the Lower Crust - LU)	Density "ρ" (kg m^{-3})	1440	~2700	ρ*=0.53
	Viscosity "η" (Pa s)	1.69x10^5	10^{22}	η*=1.69x10^{-17}
	Thickness "h" (m)	0.01	15000	h*=6.67 x 10^{-7}
Qz-Kfeld sand mixture (80:20 % in weight) (simulates the Upper Crust - UC)	Density "ρ" (kg m^{-3})	1440	~2700 (upper crust)	ρ *~0.53
	Internal friction coefficient "μ"	0.81-1	0.85-1	μ*~ 1
	Cohesion "c" (Pa)	~6	~1x10^7	c*=6x10^{-7}
	Thickness "h" (m)	0.01	15000	h*=6.67x10^{-7}
Length "l" (m)		0.01	15000	l*=6.67 x 10^{-7}
Gravity "g" (m s^{-2})		9.81	9.81	g*=1
Stress "σ' (Pa)				σ*=3.53x10^{-7}
Strain rate "$\dot{\varepsilon}$" (s^{-1})		5.55x10^{-4}	2.66 x10^{-14}	ε*= σ*/η* = 2.1x10^{10}
Velocity ,'v' (m s^{-1})		5.55x10^{-6}	3.99 10^{-10} (=12.5 mm yr^{-1})	v*= ε* l*=14000

Table 2-1. Scaling ratios for the analogue models presented in series D3.5-1. The asterisk (*) denotes the ratio between model and nature for a given parameter. Characteristics of the granular material represented by the Qz-Kfeld sand mixture (80:20 proportion % in weight) are derived from Montanari et al. (2017a). The range for the internal friction coefficients is calculated considering the "peak friction" and "stable friction" values of the granular mixture.

2.3.2 Description of the experimental series D3.5-1

In order to obtain the most performing setting in terms or materials, scaling and geometry, we have tested the deformation apparatus running 26 models. Some of these models were run to check reproducibility and therefore will be not shown. Among all the models, we have selected 9 models representing a complete experimental series aiming at the investigation of the relationships between rift propagation and inherited fabrics. The basic setup for all these models is described in Section 2.3.1, where 1 cm-thick layer of PDMS-Corundum layer simulates the LC and the 1 cm-thick layer of Qz-Kfeldspar sand mix layer mimics the UC. This basic setup (corresponding to model RP-1) was varied, depending on the model, by introducing 1 or 2 sets of artificial discontinuities (S1 and S2) trending with a specific angle to the orthogonal (defined as the

arbitrary "North" of the model) to the rift propagation direction (Fig. 2.9a). The discontinuity were represented by artificial dilation zones obtained by "cutting" the sand package with a gliding knife. Reorientation of particles caused local weakening of the sand mixture, which has the ability to focus deformation when the discontinuities are favourably oriented under the local stress field induced by model deformation. In each model of series (RP-1 to RP-9) we varied the discontinuity trend as reported in table Table 2. Model RP-1 had no discontinuity and was used as "reference model". In models RP-2 and RP-3 we introduced only one set of discontinuities, to avoid any possible mutual effect of the two sets. Models RP-4 to RP-9 tested the effect of rift propagation on two different sets of discontinuities trending at various angles.

Model Name	Azimuth of S1 (α) [°]	Azimuth of S2 (β) [°]
RP-1	/	/
RP-2	30	/
RP-3	/	125
RP-4	30	125
RP-5	45	135
RP-6	60	120
RP-7	15	165
RP-8	75	105
RP-9	90	180

Table 2-2. List of nine selected models. S1 and S2 represent the two sets of discontinuities introduced artificially in the model upper crust to mimic inherited fabrics. Azimuth was measured in clockwise direction to an arbitrary "north" defined as the orthogonal to the direction of rift propagation (see also schematic sketch in Fig. 2.9).

2.4   Analogue modelling procedure of Series D3.5-2

2.4.1   Series D3.5-2: Material, setup and scaling

Caldera collapse has been modelled by different authors using various approaches, such as rigid "piston-driven" collapse (e.g., Acocella et al., 2000, Roche et al., 2000), with clear advantages for model development and reproducibility. Nonetheless, other approaches -e.g. "balloon-collapse", where an inflated balloon is deflated inside sand layers, or depletion of a magma-analogue reservoir- have been also employed (see Acocella, 2007 and reference therein). In our experiments, we followed the latter approach, building a circular magma-analogue chamber inside a sand-pack mimicking the brittle overburden. In detail, a circular magma chamber (build with wet chalk poured in a standard silicon mould; 12 cm in diameter and 2 cm thick) was placed at the base of a 6 cm-thick sand pack. Coloured millimetre-sand horizons were sieved with a

regular vertical spacing of 1 cm during the building of the model, and used as passive markers to visualise internal deformation once the model were cut. Each model was built in a Plexiglas box and the magma chamber was drained from a central circular hole placed at its base. The amount of drained analogue magma was constantly monitored in order to extract only the desired volume. The magma analogue was simulated with pure vegetable Polyglycerine-3 (PG3; see Montanari et al., 2017b), while the sedimentary cover consisted of a blend of Quartz sand (Fontainebleau sand, provided by Sibelco Italia S.p.A.) and Potassic-feldspar sand (K-feldspar superfine sand, produced by the AKW Kaolin) mixed with a 70:30 proportion in weight (Montanari et al., 2017a). We used frozen PG3 since, from various tests, we realized that an ambient temperature PG3 suffers the differential stress induced on the magma chamber surface during the sand pouring procedure, resulting in an asymmetric caldera edifice (i.e., a trap-door system). Once the models were build, we waited at least 2 hours before starting the deformation, in order to allow PG3 defrosting. This operation was conducted at controlled ambient temperature (25°C) to guarantee a uniform PG3 rheology for all the performed models. Undesired differential surface deformation during the defrosting procedure was also prevented by verifying horizontality of the model with a spirit level, and afterwards tested acquiring DEM of model surface at the end of the defrosting procedure. The obtained high resolution DEM are able to catch incipient deformation, invisible to the naked eye. Thanks to this test, we can exclude undesired differential surface deformation before caldera collapse development. For comparison, during caldera collapse, the 65% of the initial magma-analogue (PG3) was drained out in all experiments to guarantee the same conditions. Initially, we used the basic setup represented by the circular magma chamber and an undeformed overburden, to simply reproduce caldera collapse. We then varied the shape of the magma chamber by imposing one or two straight sides, simulating pre-existing fault discontinuities. Afterwards, depending on the model, the sand package was pre-deformed by introducing various discontinuities in different positions to simulate inherited fabrics within the brittle crust. Discontinuities in the overburden were obtained by cutting through the sand with a "discontinuity apparatus" (DA), which allows to cut perfectly straight into the sand pile through a knife fixed onto an adjustable glide allowing to vary depth and inclination of the cuts (see section 2.2.2). This operation re-orients particles, generating a sharp and narrow millimetre-discontinuity zone that can easily focus the deformation during model development, if favourably oriented with respect to the local stress field. At the end of deformation, target models were impregnated with water and frozen for 12 hours, in order to properly consolidate and section the models. This procedure allows the internal investigation of the caldera fault pattern. Reproducibility of results has been checked by replicating the models several times.

The models were scaled down to nature (Tab. 2-3; Ramberg, 1981) following the assumptions and procedure reported in Montanari et al. (2017a). We set a length scaling ratio l* (being l* the ratio l_m/l_n, where l_m is the length in the model and l_n is the nature length) of 10^{-5}, so that one centimetre in the model scales to 1 kilometre in nature. This scaling value is a proper ratio to investigate model structure at the resolution of

interest. Models were run in natural gravity, so that the g* - this parameter being the scaling ratio between g_m (gravitational acceleration in the model) and g_n (gravitational acceleration in nature) - is equal to 1. The use of Qz/K-feld sand mixture with 70:30 proportion in weight led to a material density (ρ_m) of ~1550 kg m^{-3}, implying a scaling ratio for density ρ* of ~0.5, considering a natural rock density (ρ_n) of ~2800 kg m^{-3}, while the coefficient of internal friction (μ) require to be equal in both the analogue material and the natural rock, (μ*~ 1). The same density scaling ratio can be considered for a natural magma and the PG3 analogue magma, being PG3 density ρ_m ~ 1280 kg m^{-3}, and ρ_n ~2500-2200 kg m^{-3} the density of an andesitic to rhyolitic magma at ~1000 C° (Murase & McBirney, 1973). These values are in agreement with the presence of a basaltic/andesitic magma for the Los Humeros/Los Potreros caldera collapse (Carrasco-Núñez et al., 2017b). However, it is worth noting that these models are not dynamically scaled to natural conditions, since inertial forces are significant in caldera collapse processes and cannot be ignored. For this reason, the 'quasi-static' approximation is not satisfied (see section 2.3.1). Regardless, these models can still give valuable hints regarding the kind of structures accommodating caldera collapse as well as the chronology of deformation, as proven by the several analogue modelling studies carried out on this topic (see section 2.1.2).

	Parameter	Model	Nature	Model/Nature ratio
Qz-Kfeld sand mixture (70:30 % in weight) (simulates the Upper Crust - UC)	Density "ρ" (kg m^{-3})	1550	~2700	ρ *=~0.57
	Internal friction coefficient	0.83-1.1	0.85-1	μ*~ 1
	Cohesion "c" (Pa)	10	~1x10^7	c*=10^{-6}
	Thickness "h" (m)	0.01	1000	h*=10^{-5}
PG3	Density "ρ" (kg m^{-3})	1190	2500-2200	0.48-0.54
	Viscosity "η" (Pa s)	17	~4 × 10^{12}- ~4 × 10^{15}	4.25x10^{-12}-4 × 10^{-15}
Length "l" (m)		0.01	1000	l*=10^{-5}
Gravity "g" (m s-2)		9.81	9.81	g*=1
Stress "σ" (Pa)				σ*=5.7x10^{-6}

Table 2-3. Scaling ratios for the analogue models of Series D3.5-2. The asterisk (*) denotes the ratio between the model and the nature for a given parameter. Characteristics of the granular material represented by the Qz-Kfeld sand mixture (70:30 proportion % in weight are derived by Montanari et al., 2017a). The range for the internal friction coefficients is calculated considering the "peak friction" and "stable friction" values of the granular mixture. Characteristic for Poly-glycerine PG3 are derived from Montanari et al. (2017b)

2.4.2 Description of the experimental series D3.5-2

In the following paragraph we describe the specific setup of the four sub-series composing series D3.5-2, which aims to investigate the role of inherited structures on caldera collapse processes. In order to have a proper reference model for comparison, we first realized simple models with a basic setup without introducing inherited discontinuities. This standard circular model belongs to sub-series D3.5-2a. This basic setup was then modified in order to take into account the role of inherited structures, following the details described in series D3.5-2b to D3.5-2d.

2.4.2.1 Sub-series D3.5-2a: Simple caldera collapse model setup (SCC)

Models belonging to sub-series D3.5-2a were performed as reference, in order to guarantee a helpful comparison with the models belonging to other experimental sub-series as well as with models available in literature. The basic setup consists of a circular analogue magma chamber (12 cm in diameter and 2 in thickness) placed at the centre of a Plexiglas box (Fig. 2.13a). The borders of the chamber were designed perfectly vertical, and the extrusion point for the drainage of the analogue magma is placed at the exact centre of the magma chamber, filled with frozen PG3. Six sand mixture layers, each 1 cm-thick, interbedded with coloured millimetre-markers, where poured and levelled to mimic the volcano-sedimentary overburden sequence. 65% of analogue magma was drained out in order to achieve the caldera collapse.

2.4.2.2 Sub-series D3.5-2b: Overburden-discontinuity caldera collapse model setup (ODCC)

In sub-series D3.5-2b we modified the SCC setup of Series D3.52a to investigate the role of overburden structures during caldera collapse. Vertical discontinuities where placed at designed locations by cutting through the sand pile with the DA. We tested discontinuity crosscutting the sand pile above the magmatic chamber in the exact centre, in a tangent and near-tangent position, as well as external to it (Fig. 2.13b).

2.4.2.3 Sub-series D3.5-2c: Substrate-discontinuity caldera collapse model setup (SDCC)

The setup for models belonging to sub-series D3.5-2c was designed to reproduce the presence of inherited fabrics in the substrate, interacting with the magmatic chamber but not crosscutting the overburden, in order to evaluate the possible influence of previously formed structures during caldera collapse (Fig. 2.13c). We reproduced an inherited structure by introducing alternatively one or two rectilinear sides at the edges of the analogue magmatic chamber. The straight structures were supposed to be normal fault/s and therefore were built with a sub-vertical attitude, and afterwards as 60° inward- and outward-dipping structures.

2.4.2.4 Sub-series D3.5-2d: Substrate to Overburden-discontinuity model setup (OSDCC)

In comparison with sub-series D35-2c, the setup of sub-series D3.5-2d aimed to investigate the role of inherited structures crosscutting the substrate as well as the overburden. Starting from the SDCC setup, we introduced a straight discontinuity in the sand-pack in continuity with the underlying fault in the substrate, creating a single and coherent inherited structure. We reproduced one/two discontinuities intersected at a 90° angle, and dipping inward or outward 90° or 60°depending on the model (Fig. 2.13d).
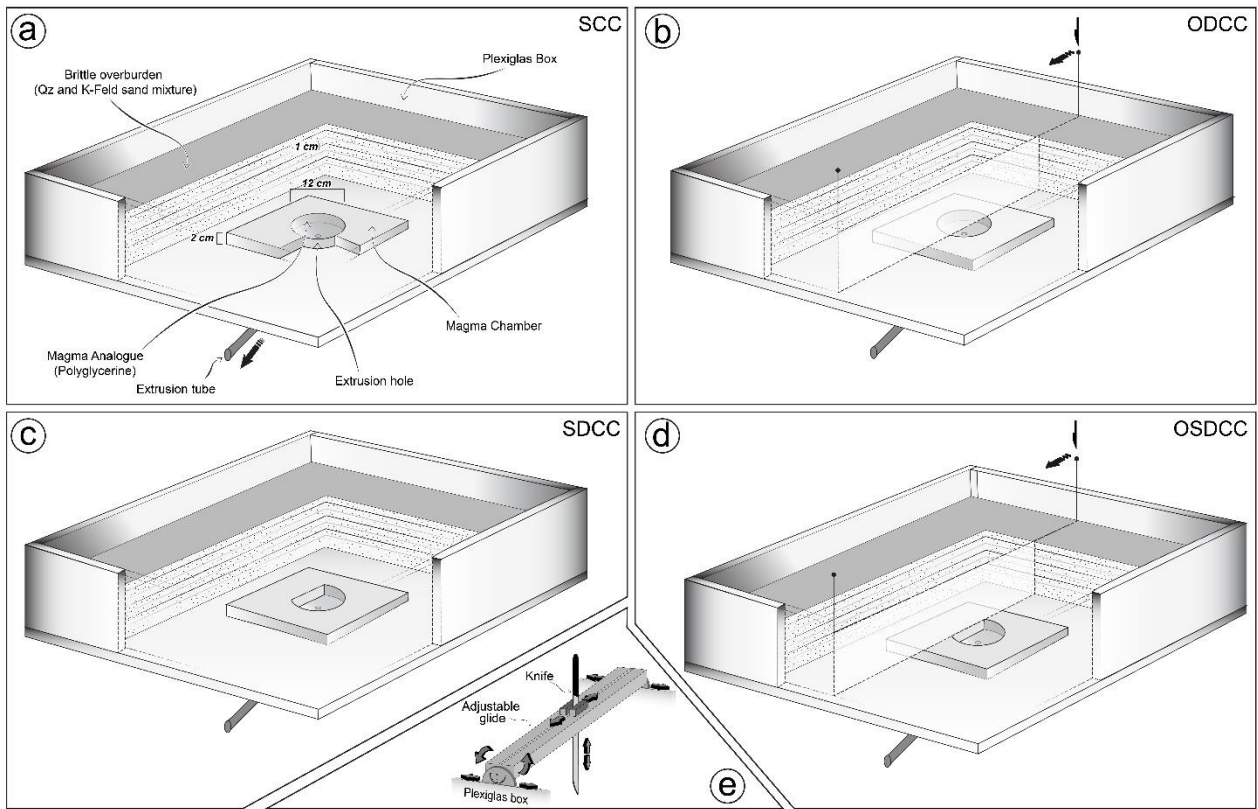
Figure 2.13. Model setup of caldera collapse analogue models for Series D3.5-2. (a) Simple Caldera Collapse (SCC) model setup of sub-series D3.5-2a; (b) Overburden-discontinuity caldera collapse (ODCC) model setup for series D3.5-2b; (c) Substrate-discontinuity caldera collapse (SDCC) model setup for sub-series D3.5-2c; (d) Substrate to overburden-discontinuity (OSDCC) model setup for sub-series D3.5-2d; (e) Cartoon illustrating the Discontinuity Apparatus (DA), used to introduce artificial pre-cuts into the sand pack, mimicking inherited discontinuities.

2.5 Monitoring and analysis of deformation

2.5.1 Monitoring of 2D and 3D deformation

The 2D model deformation was constantly monitored by automatic acquisition of high-resolution top view photos with 120 seconds time-steps. 3D deformation was quantified using photogrammetric techniques by means of the Agisoft Photoscan® software. To this purpose, we have acquired dedicated high-resolution "all-around" photos of the target model from pre-determined perspective (Fig. 2.14) in order to obtain a 3D rendering (point dense cloud) of model surface and the interpolated digital elevation model (DEM). The use of markers placed at fixed, and locally geo-referenced positions on the model setup allowed the equal scaling of all obtained DEMs. The zero-reference level for the height was arbitrary re-assigned to undeformed portions of each model surface, so that uplift and subsidence developed during model deformation resulted in positive and negative elevation values above and below the reference surface.
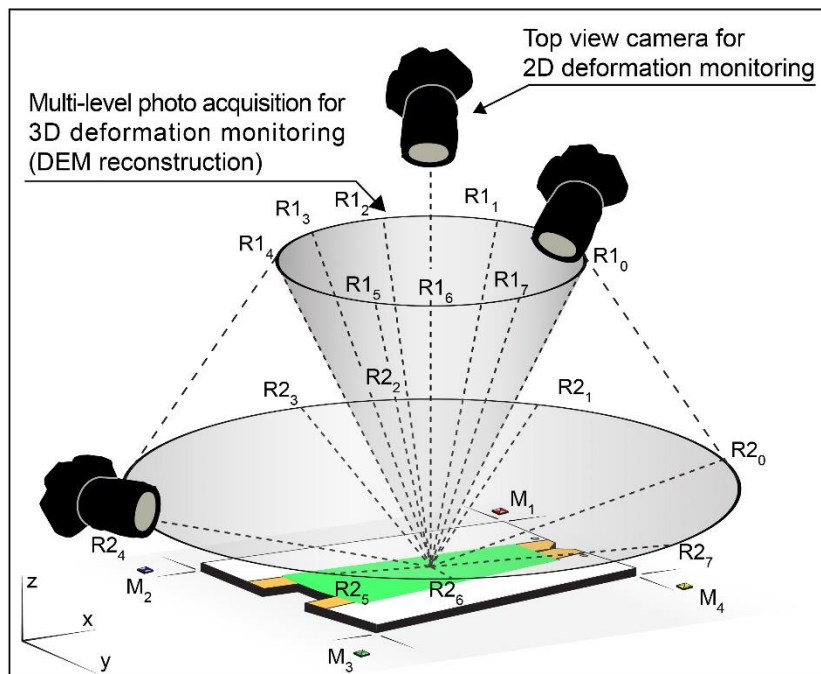
Figure 2.14 Schematic cartoon illustrating the adopted monitoring strategy: a fixed camera acquired high-resolution top-view photos to monitor the 2D deformation, while a moving camera acquired high-resolution photos at pre-determined positions (R1$_0$-R1$_7$ and R2$_0$-R2$_7$, to be used for photogrammetric analysis and DEMs elaboration. The correct scaling of DEMs is warrant by the use of locally geo-referenced markers (M$_1$-M$_4$).

3D deformation was also investigated by cutting a pair of sub-orthogonal cross sections through the models, which were taken through a saw after that models were saturated with water and frozen. The model sections were afterward cleaned by razing with a blade. This allowed us to evaluate fault offset and geometry by observation of mm-thick coloured layers introduced during model construction and acting as passive markers of deformation.

2.5.2 Quantitative analysis of deformation

Acquisition of high-resolution photos allowed for 3D reconstruction of DEM surfaces. DEMs were built, before the beginning of the deformation phase, in order to obtain a reference to check horizontality, and once the deformation phase was completed. GIS software (QGIS®) was used to visualize, elaborate and make calculation on DEM surfaces.

2D top view photos allowed for temporal monitoring of deformation (with time step interval of 120 seconds). Furthermore top view photos were used to implement quantitative analysis of model surface. Specifically, top view photos were elaborated to be used for Digital Particle Image Velocimetry Analysis (DPIV with the *PIVlab* algorithms developed by Thielicke and Stamhuis (2014) available for MATLAB®). DPIV is a common technique for non-intrusive, quantitative and qualitative flow visualization. Specifically, *PIVlab* allows for analysis of image couples that is able to calculate vectors of particle displacements between the two photographic frames. If the frames are correctly scaled in terms of pixel/meters dimension and time interval, the software can easily provide velocity vectors and derivative parameters, visualized as gradient maps. The realized maps can then be interrogated in order to produce statistics, velocity (or other parameters) profile, etc, quantifying the 2D deformation of a target model.

The same 2D photo dataset was used to implement geometrical analysis of models using the algorithm of *FracPaQ* (Healy et al., 2017). This MATLAB® tool allows quantification of the fracture pattern, and can be adapted to investigate analogue model deformation. Specifically, once top view photos have been correctly interpreted with fine line-drawing, this software is able to calculate geometry of the mapped faults and fractures and elaborate statistic as well as derivative parameters (see FracPaQ user guide for an in-depth overview of functions). We have used the FracPaQ tools to produce rose diagrams of mapped structures, histograms of fault trace lengths, and specifically to analyse the tendency of determined faults to experience slip or dilation under a certain stress field.

3 Analogue modelling analysis and results

3.1 Results of Series D3.5-1: Relationships between a propagating rift and existing crustal faults

In the following paragraphs we describe the models belonging to the Series D3.5-1, aiming at the investigation of the interplay of possibly reactivated crustal and rift-related structures. Among a total of 26 models, we present here the results of 9 models, representing the entire series. As detailed above, the other models were run to test reproducibility, sensitivity of specific parameters, and to properly set the modelling apparatus.

3.1.1 Model RP-1: Reference model

Model RP-1 was run with a basic setup, without introducing any discontinuity. The aim of RP-1 model was to obtain a reference model, allowing the observation of the development of a simple rift system. Inherited fabrics may in fact interact with the propagating rift structures, influencing their geometry and evolution. From t=0 to t=80 (Fig. 3.1a-e) the opening of the MP causes incipient deformation out of the area of interest (i.e., the opaque areas in Fig. 3.1). After t=80 (Fig. 3.1e) small graben systems start to develop and link, propagating toward the poles of rotation. Fault throw was larger in the left-side of the model, where more incremental deformation was registered, and decreases toward the rotation poles where shallow grabens were visible. Overall, the cumulative throw of graben fault systems led to a structural configuration somehow similar to a "wide rift", resulting in a deformation wedge propagating toward the poles of rotation and incrementally increasing the number, length and throw of the faults with time (Fig. 3.1a-l, Fig. 3.1a).

The final stage of deformation (Fig. 3.1l; Fig. 3.2a) highlighted the presence of converging graben systems toward the right-side of the model (i.e., toward the rotation poles), indicating the progressive reorientation of the S_{Hmax} in the model. Fault segments show an average E-W trend (i.e., striking N90°, considering the vertical direction, orthogonal to the direction of rift propagation, as the "North" of the model; red line in Fig. 3.2b), and a maximum trace length of 0.12-0.13 m, with a maximum length frequency peak of 28% of measured traces around classes 0.005-0.01 m.
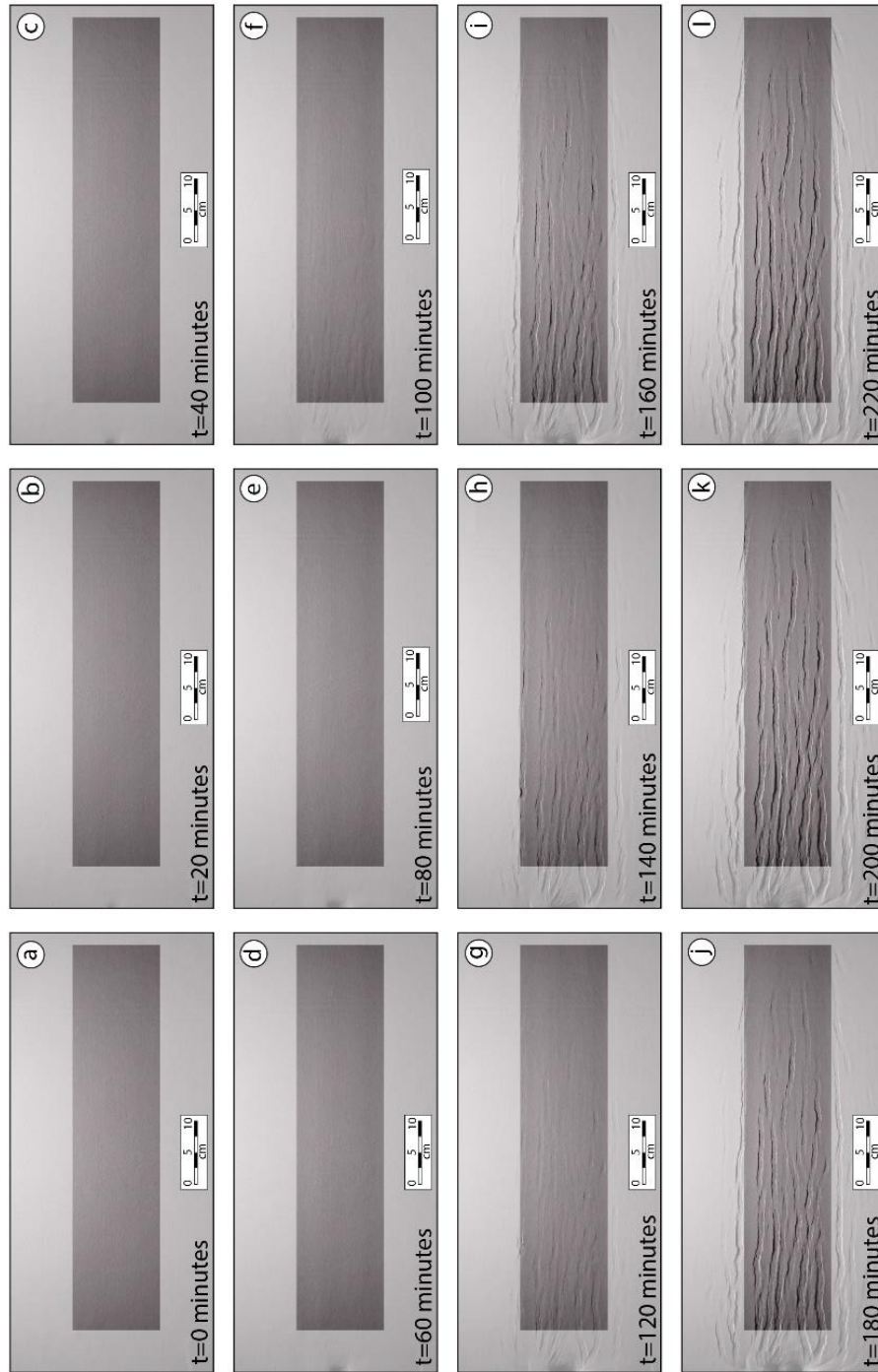
Figure 3.1. Top view evolution of Model RP-1. In this figure, deformation is shown every 20 minutes. (a) to (e) Deformation is localized outside the area of interest, in the centre of the left side of the model; (f) deformation begins to be visible as a system of small-throw conjugate normal faults developed on the left side of the model, where the diverging velocity of the two mobile plates is higher; (g) to (k) faults in the left side of the model gain larger displacement, developing well-structured graben systems that propagate towards the right side of the model (i.e. towards the poles of rotation); (k) after 220 minutes of deformation, the propagating rift has reached the rotation poles. Shallow and smaller grabens developed in this area, while in the left sector of the models the structures acquire larger throws. A clear increasing "V" shaped gradient of deformation toward the poles of rotation is detectable observing the overall ("a" to "l") model evolution.

Figure 3.2. **(a) Top view of the final stage of deformation (t=220 minutes) of Model RP-1. DEM of the surface is superimposed onto the area of interest. A well-developed "V- shaped" pattern of deformation is visible. Stroke of line drawing indicates fault throw magnitude, clearly decreasing toward the right-side of the model (i.e. toward the rotation poles). (b) Rose diagram showing fault segment orientation (for a total of n=955 mapped segments). The red line indicates the average trend. Angles are calculated from the "North" of the model in clockwise direction. (c) Frequency distribution of trace lengths (n= 209) for model RP-1. DEM in a) was obtained through Agisoft Photoscan®, while rose diagrams and histograms in (b) and (c) were elaborated through FrcPaQ (Healy et al., 2017). The same applies to all the models of series D3.5-1 presented in the following paragraphs.**

3.1.2 Model RP-2: S1 trending N30°

Model RP-2 (Table 2.2; Fig. 3.3a) differs from reference model RP-1 in that we introduced artificial discontinuities belonging to set S1, which trend 30° with respect to the orthogonal to the direction of rift propagation (angle α = 30°; see Figure 3.3). A single set of discontinuities was introduced to avoid any possible reciprocal influence. The general model development did not differ from the evolution of RP-1, showing incipient normal faulting in the left-side area of the model, which progressively propagated toward the rotation poles (right-side of the model) to form a "V-shaped" subsiding wedge in the centre of the model.

51

The wedge tip migrated progressively with the opening of the MP. Model deformation showed a clear gradient in terms of fault throw (larger for faults localized in the left-side of the model) and fault number (larger for faults localized in the left-side of the model). The average fault trend (red line in Fig. 3.3b) is N90° and the length of mapped fault traces shows a distribution marked by a large amount of small fault traces (the frequency peak of 25% is reached for fault trace class of 0.01-0.015 m) and some longer faults (up to 0.1 m). No evidence of reactivation of discontinuities belonging to set S1 is observed (Fig. 3.3a), as also notable from the rose diagram (Fig. 3.3b) where no classes trending N30° are present in the fault segment orientation.

Figure 3.4 (a) Top view of the final stage of deformation of Model RP-2 with S1 trending N30°. DEM of model surface is superimposed onto the area of interest. Stroke of line drawing indicates fault throw magnitude. (b) Rose diagram showing fault segment orientation (for a total of n=859 mapped segments). The red line indicates the average trend. Angles are calculated from the "North" of the model in clockwise direction. (c) Frequency distribution of trace lengths (n=212) for model RP-2.

3.1.3   Model RP-3: S2 trending N125°

In Model RP-3 (Tab. 2.2; Fig. 3.4a) we introduced artificial discontinuities belonging to the set S2 with α=125 (i.e., trending N125°). As in model RP-2, a single set of discontinuities was introduced to avoid any possible reciprocal influence. Model development was similar to standard model RP-1 and to RP-2. A well-

developed graben system started to form from the left-side area of the models, propagating toward the rotation poles. Larger faults, bearing the higher throw, reach a maximum length of ~9 cm (Fig. 3.4c), as in model RP-2. Similarly, Model RP-2 and RP-3 shared the same average trend of structures, being the mean strike N93° (Fig. 3.4b). Besides general similarities with model RP-1 and RP-2, Model RP-3 showed the clear reactivation of the S2 discontinuities. Particularly, weak zones trending N125° were reactivated during deformation and developed couples of conjugate normal faults (i.e., incipient small graben systems) trending N125° (Fig. 3.4a). Weak zone reactivation affected all the S2 weak zones, yet in a scattered and discontinuous manner. Nonetheless, it is worth describing the effect of such reactivated weak zones, in that many rift-related structures (i.e., black faults in Fig. 3.4a), trending ~N90°, stopped to propagate in correspondence of the weak zones and were deflected. Reactivated structures (red fault in Fig. 3.4a) may have acted as transfer zones, forcing the propagation of rift-related structures to shift laterally (yellow arrows in Fig. 3.5).
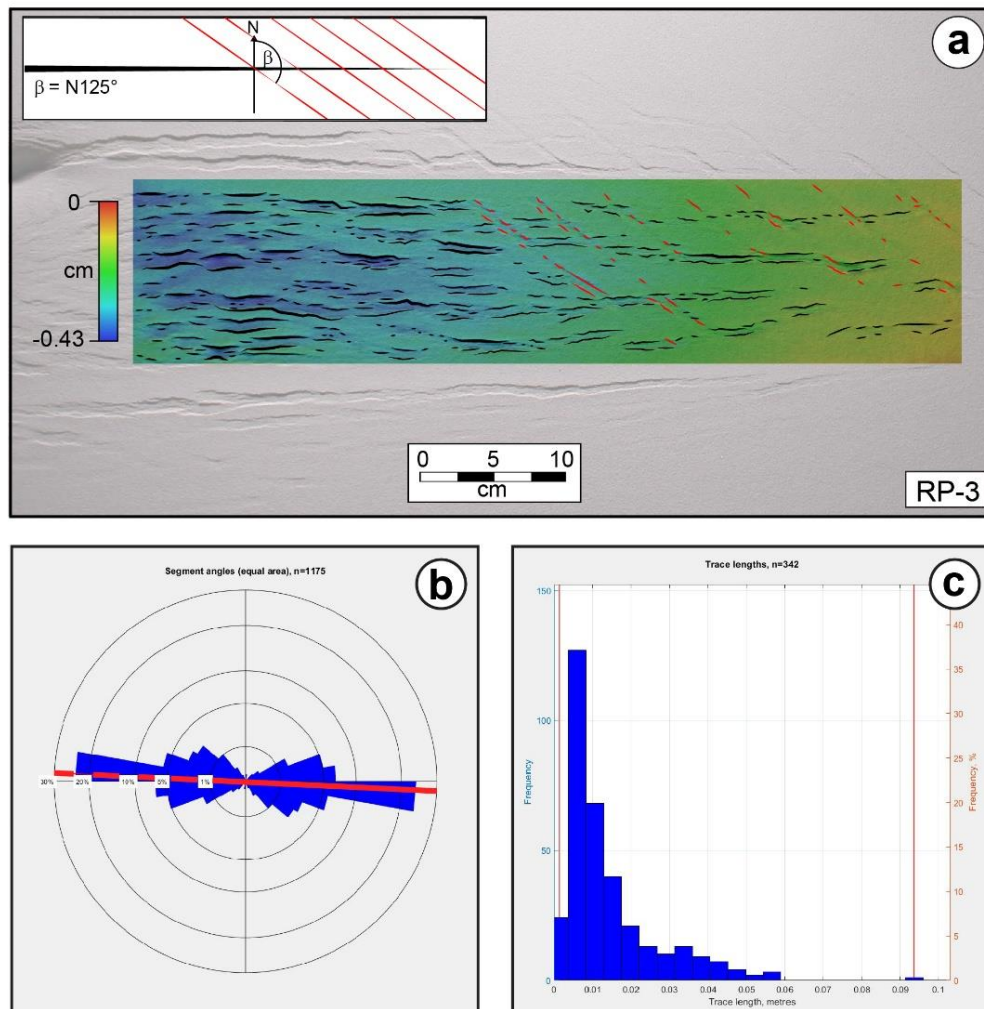
Figure 3.5. (a) Top view of the final stage of deformation of Model RP-3, with S2 trending N125°. DEM of the surface is superimposed onto the area of interest. Stroke of line drawing indicates fault throw magnitude. Red lines mark reactivated S2 discontinuities. (b) Rose diagram showing fault segment orientation (for a total of n=1175 mapped segments). The red line
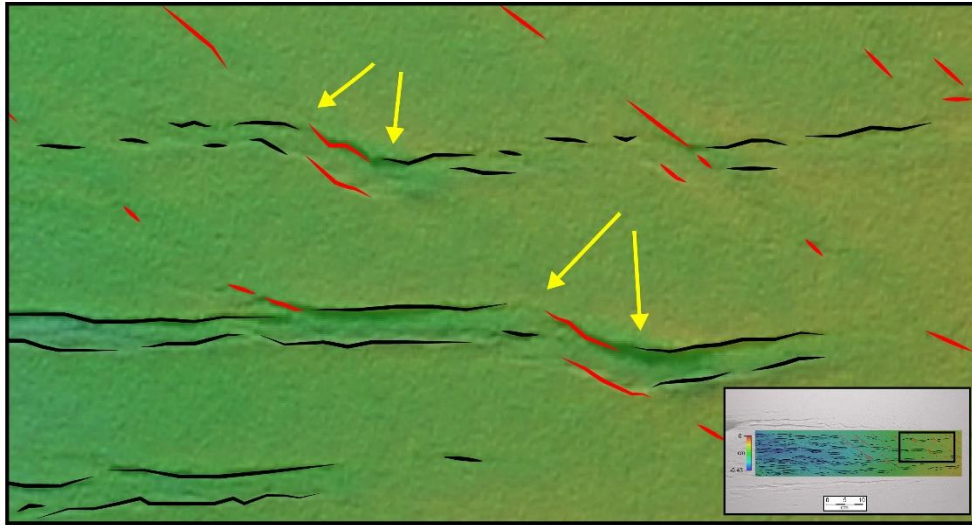
Figure 3.6. Detail of Model RP-3 surface (see inset for location) highlighting the role of reactivated S2 structures (red lines) as possible transfer zones. Rift-related structures were forced to shift laterally their propagation once they reached the weak reactivated zones. Yellow arrows indicate the lateral shift of rift related faults.

3.1.4 Model RP-4: S1 trending N30° and S2 trending N125°

Model RP-4 aims to reproduce the natural setting of the TMVB that includes the presence of inherited structure as observed in the Los Humeros and Acoculco regions by many authors (see section 2.2.1). Following the described angular correction, the average natural trend of N40° and N140° is represented in our models by weak zones trending N30° and N125°, respectively. Therefore, in Model RP-4 we introduced contemporaneously S1 and S2 discontinuities (respectively oriented N30° and N125°). Evolution of model deformation is similar to models RP-2 and RP-3, with the "V-shaped" central depression propagating and subsiding as the result of the development of a graben system (Fig. 3.7a). The average trend of structures (N95°) marks the prominent role of rift-related faults, but, as in Model R-3, the S2 weak zones were reactivated to form conjugate normal faults (i.e., graben systems; red lines in Fig. 3.7a) trending N125°. S1 discontinuities introduced with α = N30° were not reactivated during model deformation, similarly to Model RP-2. As for Model RP-3, some of the S2 weak zones were reactivated as N125°-trending graben systems and acted as transfer structures that forced rift-related faults to shift laterally their propagation toward the rotation poles.
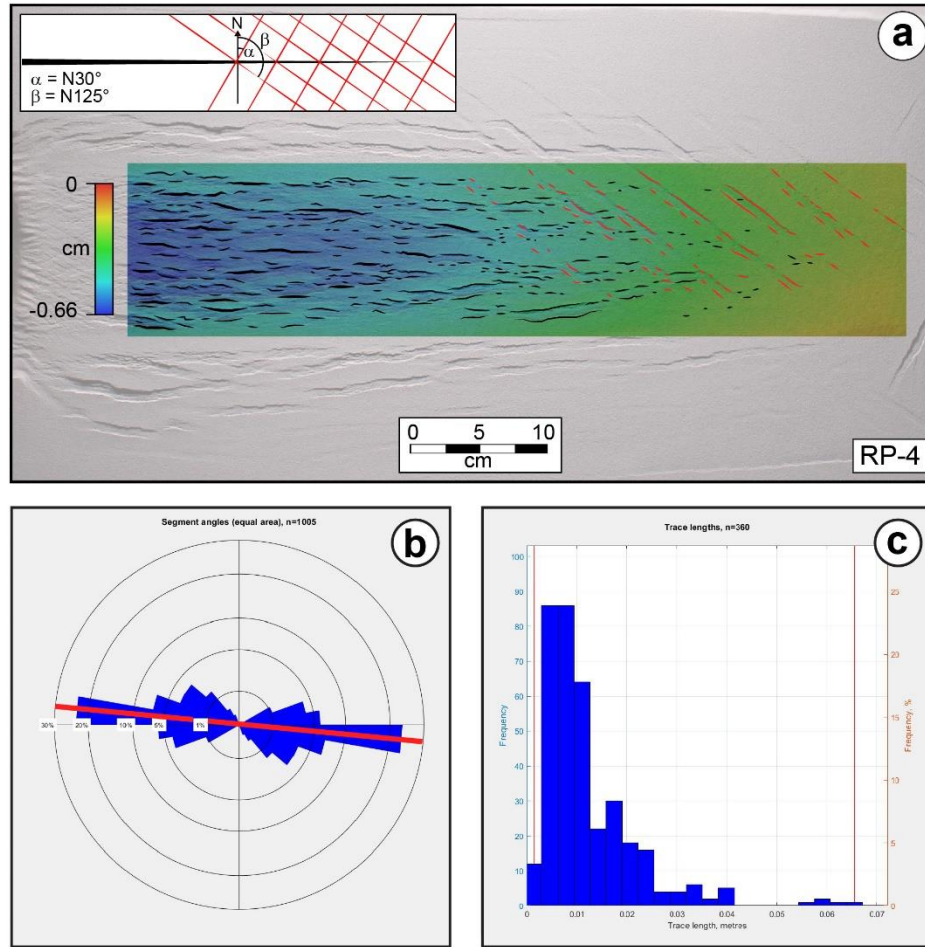
Figure 3.7. (a) Top view of the final stage of deformation of Model RP-4, with S1 trending N30° and S2 trending N125°. DEM of the surface is superimposed onto the area of interest. Stroke of line drawing indicates fault throw magnitude. Red lines mark the reactivation of the S2 weak zones, while no reactivation of S1 discontinuities is observed. (b) Rose diagram showing fault segment orientation (for a total of n=1005 mapped segments). The red line indicates the average trend. Angles are calculated from the "North" of the model in clockwise direction. (c) Frequency distribution of trace lengths (n=360) for model RP-4.

3.1.5 Model RP-5: S1 trending N45° and S2 trending N135°

Model RP-5 tested the role of S1 and S2 set discontinuities trending α = N45° and β = N135°, respectively (i.e., S1 and S2 were orthogonal). The general evolution of the model is consistent with what observed in models RP-1, RP-2, RP-3 and RP-4 (i.e., rift-related fault localization, average trend and trace length distribution, Fig. 3.8 a,b,c). In Model RP-5, weak zones S1 and S2 were both reactivated.
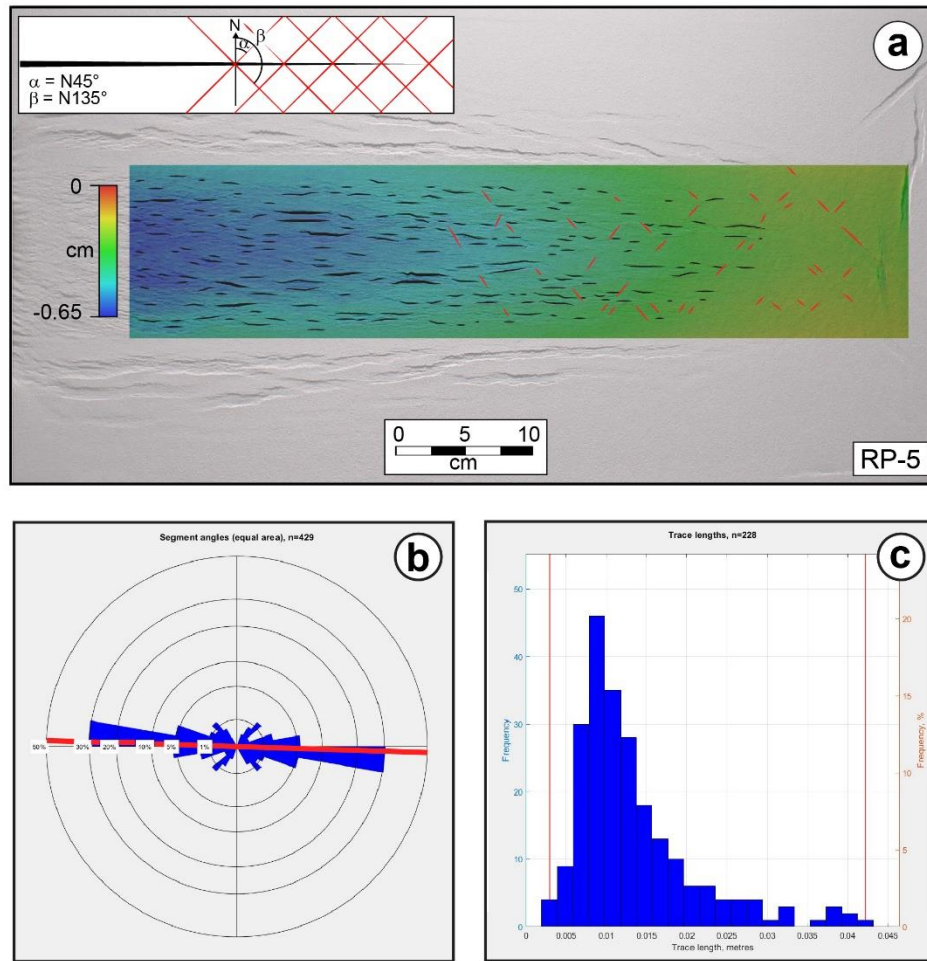
Figure 3.8. (a) Top view of the final stage of deformation of Model RP-5, with S1 trending N45° and S2 trending N135°. DEM of the surface is superimposed onto the area of interest. Stroke of line drawing indicates fault throw magnitude. **(b)** Rose diagram showing fault segment orientation (for a total of n=429 mapped segments). The red line indicates the average trend. Angles are calculated from the "North" of the model in clockwise direction. **(c)** Frequency distribution of trace lengths (n=228) for model RP-5.

3.1.6 Model RP-6: S1 trending N60° and S2 trending N120°

Model RP-6 tested the role of discontinuity sets S1 and S2 trending symmetrically, at 30°, to the direction of rift propagation (i.e., with α=60° and β=120° for S1 and S2, respectively). Model RP-6 followed the same evolution as the other models of the series, developing the "V-shaped" depression progressively propagating toward the poles of rotation (Fig. 3.9a). In this area, the cumulative deformation was gained by the development of N90° trending (on average) graben systems. Both weak zones (S1 and S2 sets) introduced in the undeformed model were largely reactivated by deformation, causing the development of a "chessboard" pattern of reactivated structures.
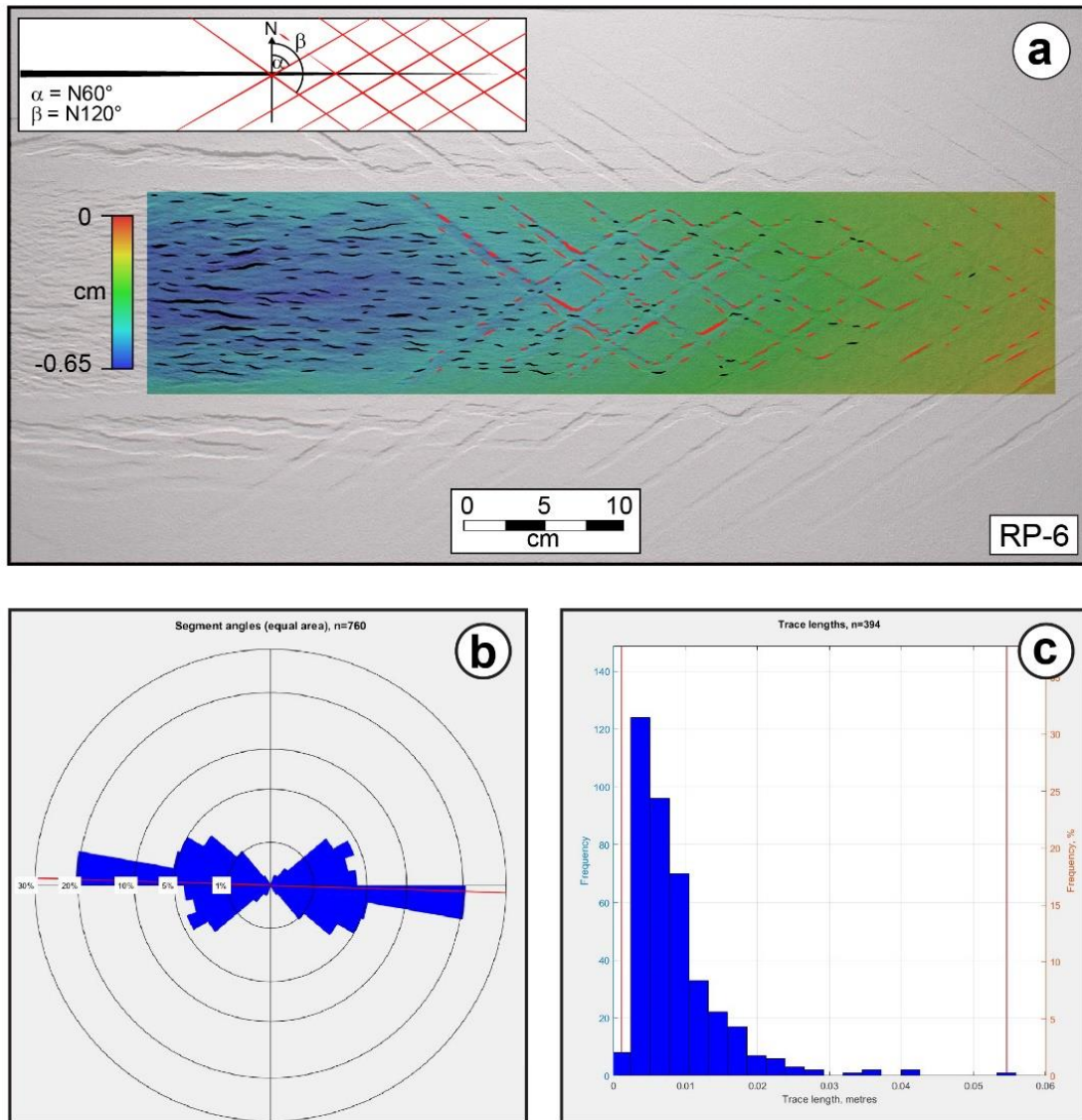
Figure 3.9. (a) Top view of the final stage of deformation of Model RP-6, with S1 trending N60° and S2 trending N120°. DEM of the surface is superimposed onto the area of interest. Stroke of line drawing indicates fault throw magnitude. (b) Rose diagram showing fault segment orientation (for a total of n=760 mapped segments). The red line indicates the average trend. Angles are calculated from the "North" of the model in clockwise direction. (c) Frequency distribution of trace lengths (n=394) for model RP-6.

3.1.7 Model RP-7: S1 trending N15° and S2 trending N165°

Model Rp-7 investigated the role of two discontinuities oriented respectively with a strike of N15° (set S1) and N165° (set S2). In Model RP-7, the "V-shaped" propagation of the graben systems trending on average ~N90° is extremely well developed. Interestingly, none of S1 and S2 sets were reactivated during model deformation, being angles α and β respectively too small and too large with respect to the direction of rift propagation for being reactivated (Fig. 3.10).
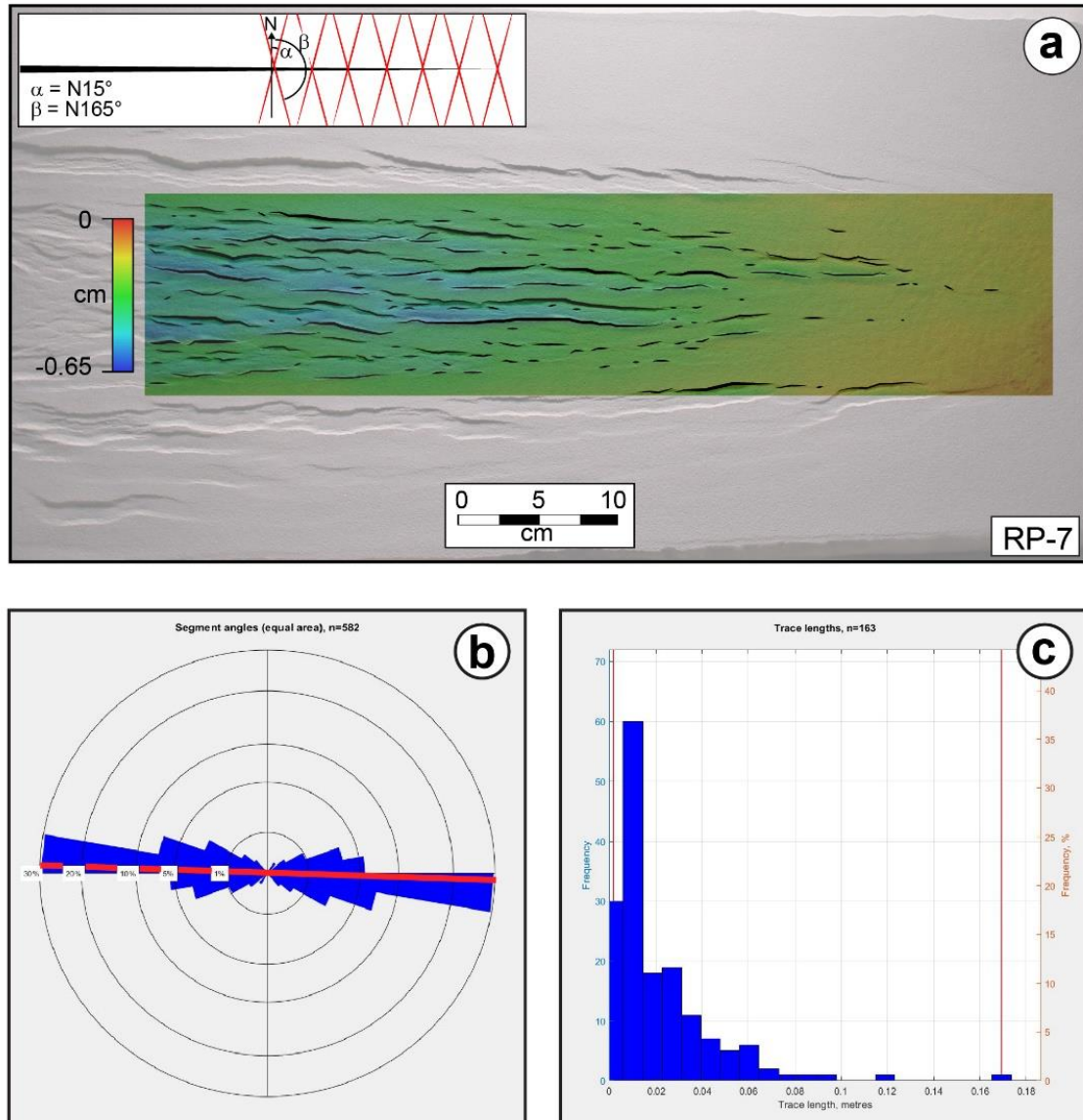
Figure 3.10. (a) Top view of the final stage of deformation of Model RP-7, with S1 trending N15° and S2 trending N165°. DEM of the surface is superimposed onto the area of interest. Stroke of line drawing indicates fault throw magnitude. None of the two sets S1 an S2 was reactivated during model deformation. (b) Rose diagram showing fault segment orientation (for a total of n=582 mapped segments). The red line indicates the average trend. Angles are calculated from the "North" of the model in clockwise direction. (c) Frequency distribution of trace lengths (n=163) for model RP-7.

3.1.8 Model RP-8: S1 trending N75° and S2 trending N105°

Model RP-8 shows the behaviour of two sets of artificial discontinuities (S1 and S2) trending to a low angle with respect to the direction of rift propagation, specifically striking N75° (set S1) and N105° (set S2). Model development followed the same chronology of deformation as the other models, developing graben systems in the left-lateral area of the model that propagated toward the rotation poles with an average trend of N90° (Fig. 3.11a, b). Nonetheless, in Model RP-8, sets S1 and S2 were broadly reactivated forming a series of coupled conjugate normal faults trending N75° and N105°, which apparently inhibited the propagation of the rift-related faults into the central and the right-lateral areas of the model. Weak zones were largely deformed as extensional structures developing strongly subsiding and elongated graben systems.
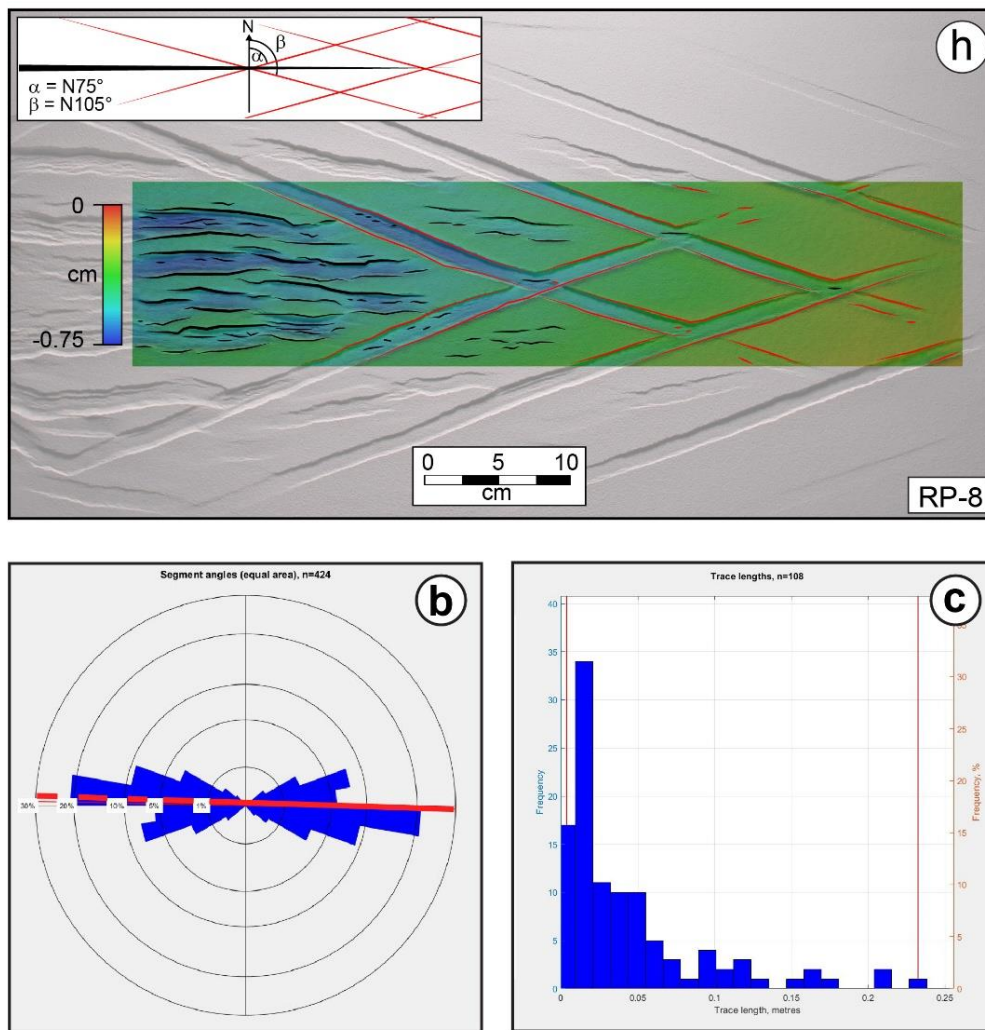

Figure 3.11. (a) Top view of the final stage of deformation of Model RP-8, with S1 trending N75° and S2 trending N105°. DEM of the surface is superimposed onto the area of interest. Stroke of line drawing indicates fault throw magnitude. (b) Rose diagram showing fault segment orientation (for a total of n=424 mapped segments). The red line indicates the average trend. Angles are calculated from the "North" of the model in clockwise direction. (c) Frequency distribution of trace lengths (n=108) for model RP-8.

3.1.9 Model RP-9: S1 trending N90° and S2 trending N180°

For completeness, we report here the description of Model RP-9, which is not shown like the other models of Series D3.5-1 because the RB holding the two MP broke just before the end of the modelling, making impossible to acquire high-resolution photos for photogrammetric analysis and DEM reconstruction. Nonetheless, we did not re-run Model RP-9, since its development gave enough information for discussion. We show here (Fig. 3.12) a top view photo immediately before the RB break. The photo clearly shows reactivation of artificial discontinuities belonging to S1 (trending N90°), while no S2 discontinuity (trending N180°) was reactivated. S1 discontinuities were highly dilatant and continuous. Rift-related faults are well developed, and in scale with rift-related structures developed in the other models of the same series.

Incipient detachment of the rubber sheet (RB) below model setup
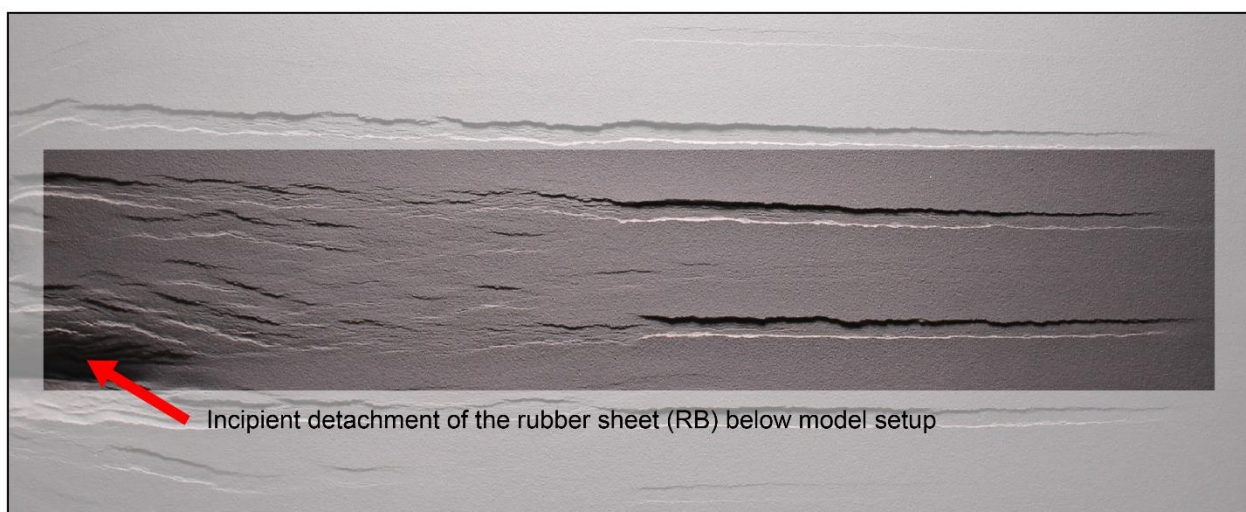
Figure 3.12. Model RP-9 top-view photo before the break of the RB. Red arrow indicates the point where RB starts to detach from the MP. Therefore, no DEM and quantitative analysis are shown for this model. Nonetheless, qualitative description is sufficient to highlight a complete reactivation of discontinuities of set S1 and no reactivation of discontinuities belonging to set S2.

3.2 Results of Series D3.5-2: Role of pre-existing discontinuities in caldera collapse

3.2.1 Sub-series D3.5-2a: Simple caldera collapse (SCC)

Models belonging to this series were performed as a standard to compare the models of the other series. The basic setup is composed of a circular analogue magma chamber (12 cm in diameter and 2 in thickness). The borders of the chamber were designed vertical, and the extrusion point was set at the centre of the magma

chamber, which was filled with frozen PG3 (see sction 2.4.1). Six sand layers of 1 cm each, reproduced the volcano-sedimentary overburden sequence. In order to achieve the caldera collapse, we drained out the 65% of PG3. Several models were run with this setup to test reproducibility. We show here below (Figs. 3.13 and Fig. 3.14) the result of the most representative models (Model-17).

Once the PG3 was completely defrosted at constant standard temperature (25°C) for two hours, deformation started by draining out the analogue magma from the chamber. At time T_1 (Fig. 3.13a), an incipient circular depression was visible above the magma chamber and a fault started to develop from one point and then propagated along a sub-circular trajectory. Top view images of the fault scarp revealed that this incipient fault likely has a reverse kinematics. Before fault propagation reached the point of fault initiation (T_2; Fig. 3.13b), the trajectory of deformation shifted to an outer position, linking the reverse fault to an incipient normal fault (T_3; Fig.3.13c). This variation is likely due to volume accommodation above the analogue magma chamber, and led to the formation of a roughly circular ring of normal faults, constituting the boundary of the caldera collapse (T_4; Fig. 3.13d). If no asymmetry is introduced during model deformation, this model evolution yields a symmetric collapse (T_5; Fig. 3.13e). The symmetric collapsed caldera is therefore constituted by a piston-like inner portion bounded by reverse faults, experiencing subsidence as a result of analogue magma drainage, and afterward formed external normal faults, representing the ring faults and therefore the boundary of the collapsed caldera. Once the model was saturated with water and frozen in order to cut cross sections, it was possible to analyse the internal structure of the collapsed caldera (Fig. 3.14).
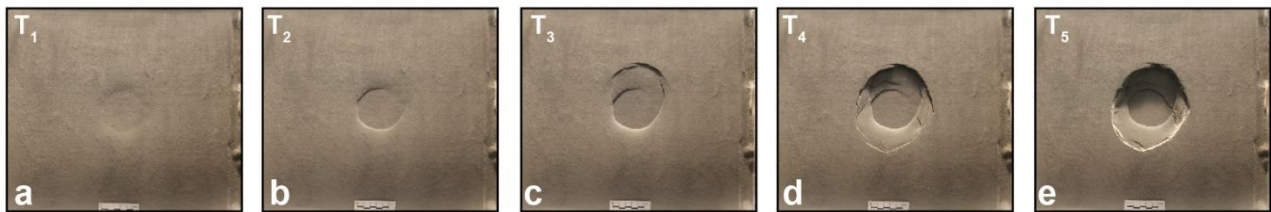
Figure 3.13. Simple and symmetric caldera collapse (Model-17). (a) incipient collapse occurred by down-sagging of the magma chamber roof; (b) circular propagation of reverse fault; (c) shift of fault propagation to a more external position and linking of the reverse fault with incipient normal fault; (d) propagation of normal fault to form ring faults of the collapsed caldera; (e) end of deformation showing the collapsed symmetric caldera system.

Orthogonal cross sections revealed a symmetric subsidence of the inner roof block, bounded by outward dipping reverse faults (developed during interval T_2-T_3). Inward dipping normal faults at the boundary of the collapsed caldera (developed during time interval T_3-T_5) connect at depth with the reverse fault system and limit the area undergoing deformation during caldera collapse.
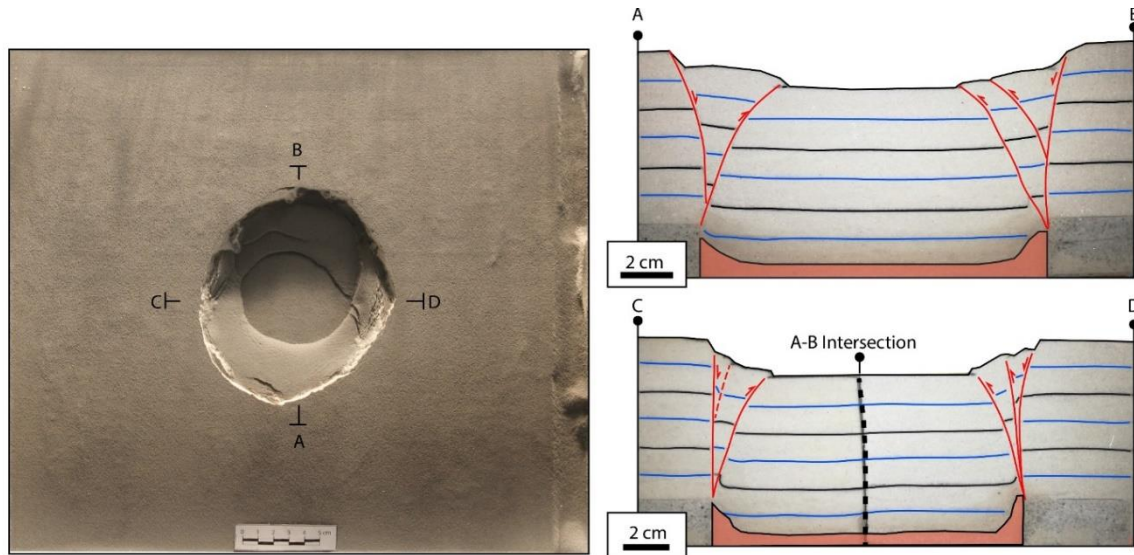
Figure 3.14. Cross sections of Model-17 showing the internal architecture of a symmetric collapsed caldera. Well visible are the systems of reverse and normal faults. Fault displacement is indicated by the coloured, passive sand markers, that were sieved during model building.

DPIV analysis on interval frames of 120 seconds showed that, despite a bulk symmetric deformation, the incremental deformation proceeded through asymmetric steps, the vectors of particle movements being oriented accordingly to fault displacement (Fig. 3.15). Faults, developing from a starting point and propagating laterally along a circular trajectory, accommodated the roof block subsidence, causing an asymmetric movement of particles. The lateral propagation is well highlighted by progressive fault displacement. Notably, faults did not form as circular feature accumulating uniform displacement, but due to lateral propagation acquired relatively non uniform local throw along fault strike.
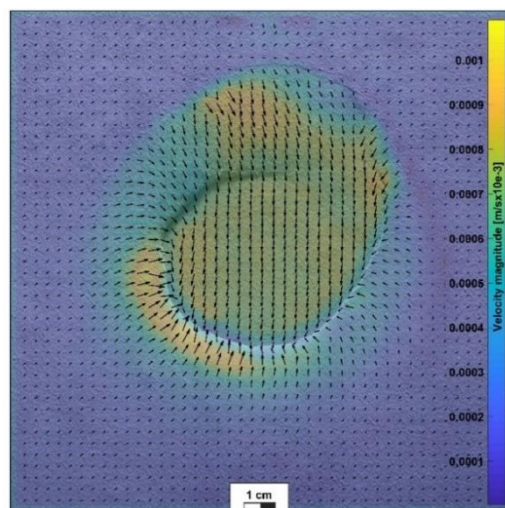
Figure 3.15. DPIV analysis of Model-17 (frames 31-32; time interval between each frame is 120 seconds). Warm colours indicate higher velocities. Note that DPIV is able to catch only 2D horizontal displacement. DPIV highlights inward movement of particles driven by progressive fault propagation and displacement.

3.2.2 Sub-series D3.5-2b: Overburden-discontinuity caldera collapse (ODCC)

In this sub-series the SCC setup (series D3.5-2a) was modified to investigate the role of overburden structures during caldera collapse processes. We placed, by cutting through the sand pile with the DA, target discontinuities at various positions with respect to the magma chamber, namely: (1) exact centre, (2) tangent and (3) near-tangent positions, and (4) external to it (Fig. 3.16) in order to test their potential influence on caldera formation and development. For each setup we show here one model (Model-20 to Model-23).

MODEL SETUP

MODEL #	SETUP	SETUP DESCRIPTION
Model-20		Near-tangent discontinuity
Model-21		Tangent discontinuity
Model-22		Central discontinuity
Model-23		External discontinuity

○ Magma Chamber | ┊ Discontinuity (sand pre-cut)

Figure 3.16. Model setups for series D3.5-2b, where artificial discontinuities in the overburden were introduced at various positions (i.e., near tangent, tangent, central and external with respect to the magma chamber).

Model-20: Near-tangent discontinuity

Model-20 tested the role of a near-tangent (internal) discontinuity, placed above the analogue magma chamber. This model started to develop as a "classic" symmetric caldera collapse, developing internal outward dipping reverse faults that started to propagate in a circular shape. Before the internal ring was closed by reverse fault propagation along the circular trajectory, deformation stepped to the external area, starting to develop normal faults. In this specific case, normal faulting did not begin as the continuation of the reverse fault propagation but reactivated the introduced vertical discontinuity (Fig. 3.17; T_1). A circular ring fault developed on the opposite side, and connected to the straight reactivated inherited structure. Notably, the reactivation influenced the final stage of reverse faulting development, attracting the tip of the reverser fault that terminated against the vertical scarp generated by the reactivation of the inherited structure (Fig. 3.17; T_1 and T_2). Nonetheless, the circular shape of the buried magma chamber still strongly controls the final morphology of the collapsed caldera: the reactivated structure is afterward bypassed and the ring fault propagation terminated with the formation of a circular normal fault system representing the ring faults of the collapsed caldera (Fig. 3.17).
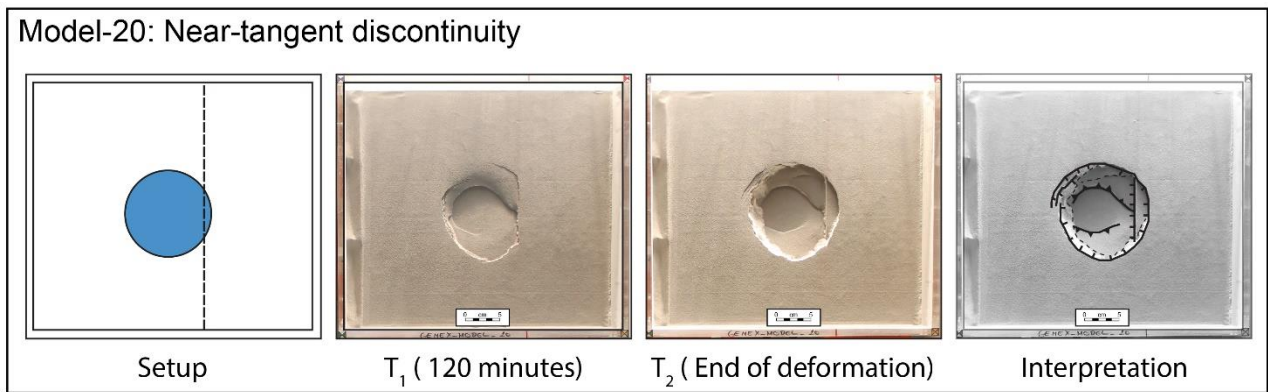
Figure 3.17. Model-20 setup, development (T₁ and T₂ corresponding to 120 and 134 minutes of deformation) and interpretation.

The final result is a collapsed caldera system showing a circular ring of normal faults (Figs. 3.17 and 3.18) with a rectilinear scarp bounding and limiting the reverse fault system. The overall depth of the depression system is about 20 mm (Fig. 3.19).

Figure 3.18. 3D reconstruction (using Agisoft Photoscan®) of Model-20 showing the rectilinear feature derived from the reactivation as normal fault of an inherited fault. The latter was introduced before model deformation as a brittle discontinuity in an internal and near-tangent position with respect to the analogue magmatic chamber.
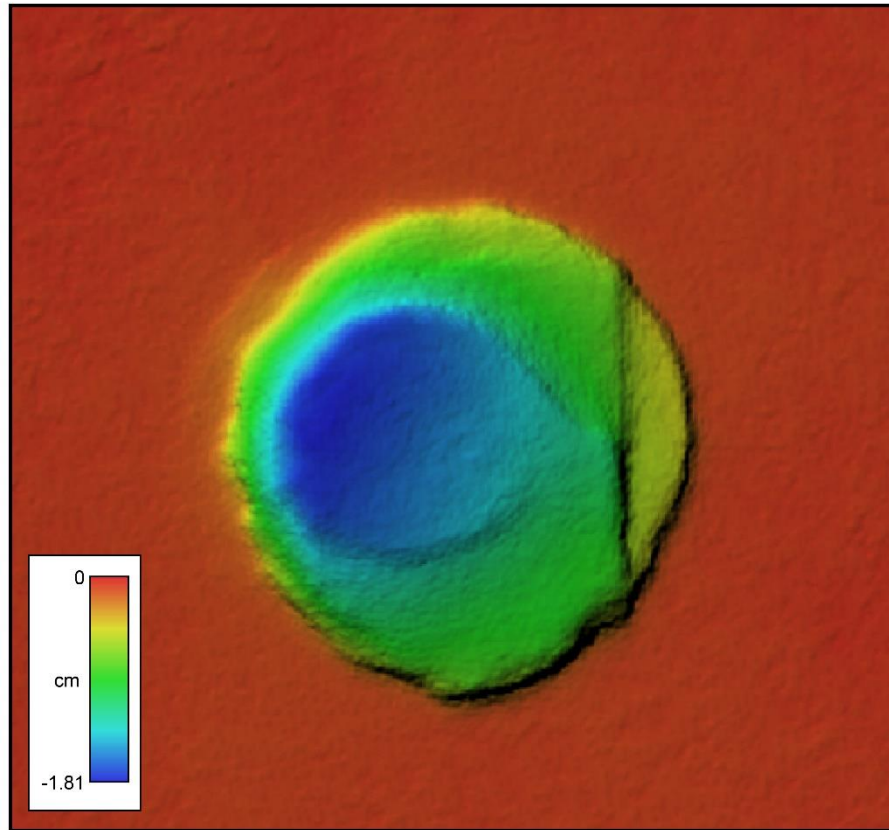
Figure 3.19. Digital Elevation Model (DEM) showing final morphology (after 134 minutes) of Model-20. The reactivated discontinuity is well visible on the right side of the model.

Interestingly, the inherited structure is one of the first to form with a normal kinematics: DPIV analysis (Fig. 3.20) shows that it stopped the propagation of the reverse fault and linked together with incipient ring faults. On the left side of the discontinuity (see red arrow in Fig. 3.20) no deformation is detected by DPIV. This inherited structure is thus acting as an internal boundary during caldera deformation.
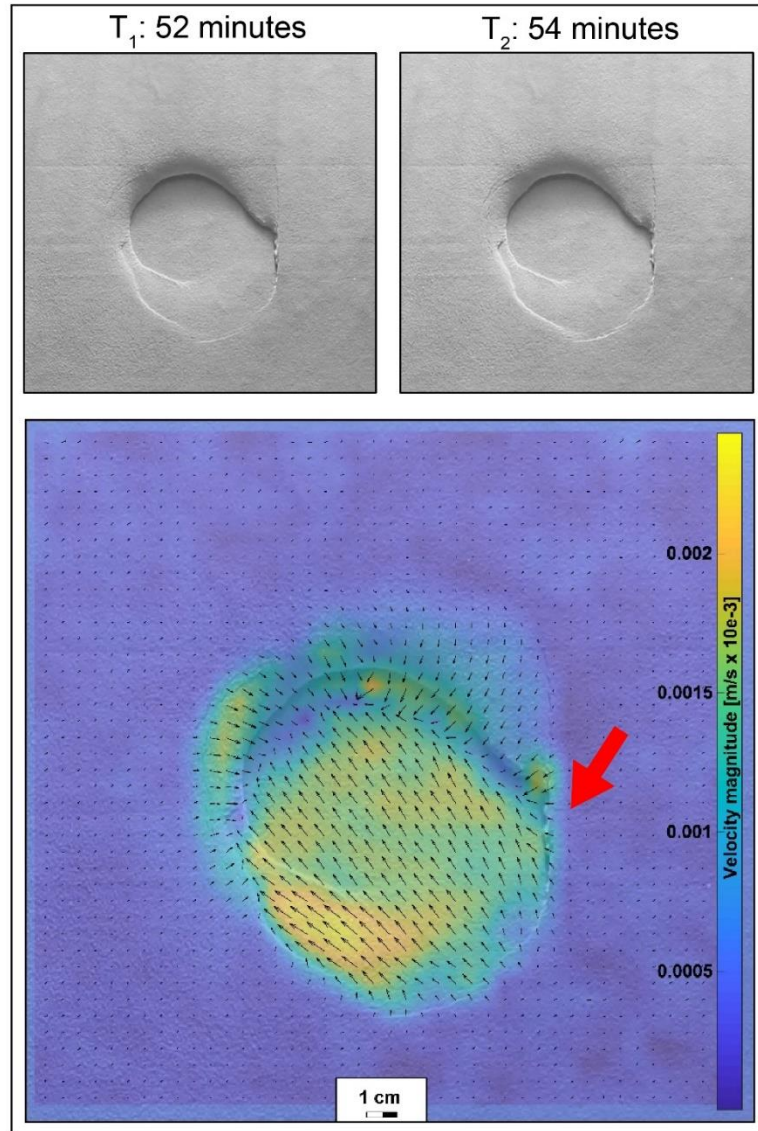
Figure 3.20. DPIV analysis of two frames (FrameT$_1$=52 minutes of deformation and T$_2$= 54 minutes of deformation; i.e., frame interval 120 seconds) for Model-20. DPIV well highlights the discontinuity reactivation and its role as a structural boundary, limiting at this stage both inner reverse fault propagation and outer (in the left area) normal fault propagation. Normal faulting continued in the left area of the model only after discontinuity reactivation. Red arrow indicates the position of the reactivated discontinuity. Warm colours indicate higher particle velocity.

Model-21: Tangent discontinuity

Model-21 tested the role of a tangent discontinuity (with respect to the analogue magma chamber), cut into the overburden. The setup is similar to Model-20, except for the position of the discontinuity, which was nearly tangent in the previous model, but in a more internal position (Fig. 3.17). Model-21 development did not show variations in the fault chronology (Fig. 3.21), and a rectilinear normal fault represents the direct evidence of discontinuity reactivation. Once the inherited structure was reactivated gaining vertical displacement, the external normal fault system then proceeded to "close" the circular caldera "ring". A difference is represented by the dimension of the reactivated discontinuity, which is rather smaller, due to its

66

tangent position. Furthermore, in this case, inner reverse faults are able to "complete" their propagation, "closing the ring" to create a central subsiding piston. Interesting is the point of intersection of reverse faults that generate a sort of fish-tail (Figs. 3.22 and 3.23). This feature can develop because the discontinuity is introduced as tangent feature, and do not forces reverse fault to develop, as happened in Model-21 where the near-tangent discontinuity is located in an inner position, and sufficiently close to the reverse faults to interact with them.
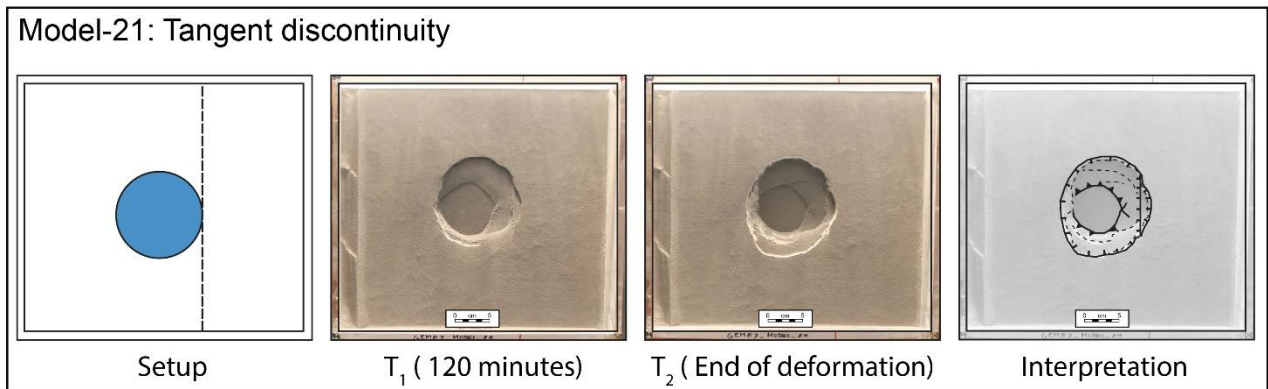
Figure 3.21. Model-21 setup, development and interpretation. In this model, an artificial discontinuity tangent to the analogue magma chamber is introduced to investigate its effect on caldera collapse.
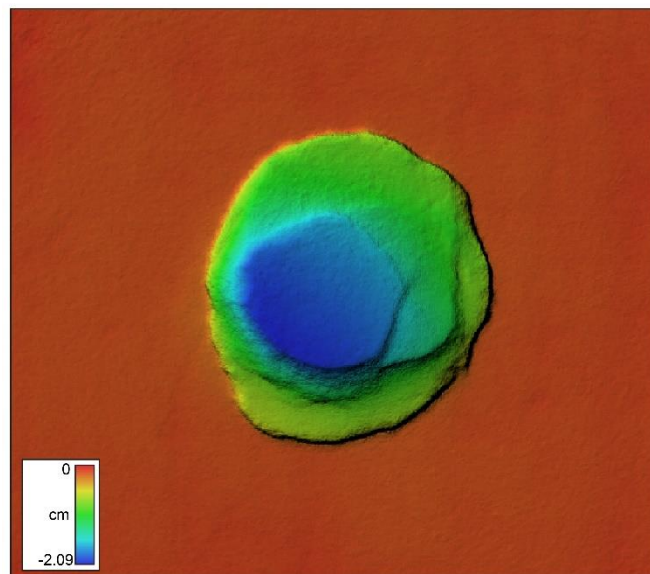
Figure 3.22. Model-21 Digital Elevation Model (DEM) of final deformation stage.
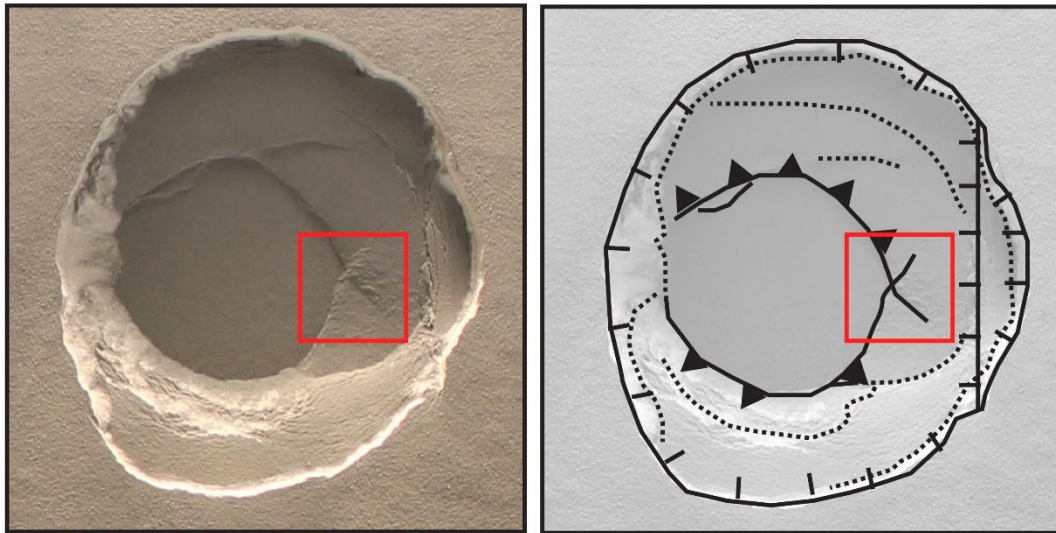
Figure 3.23. Model-21 top view, Final stage of the model deformation is shown on the left panel, while interpretation is presented on the right panel. The red squares mark the 'fish-tail'-like feature, developed as a result of reverse fault propagation and intersection.

Interestingly, this feature did not appear as the simple result of reverse faulting due to piston-like subsidence at the caldera centre. In particular, DPIV analysis highlighted a strike-slip component of the displacement vectors in the area developing the fish-tail-like feature and along the inner portion of fault that connect to it (red rectangle in Fig. 3.24).
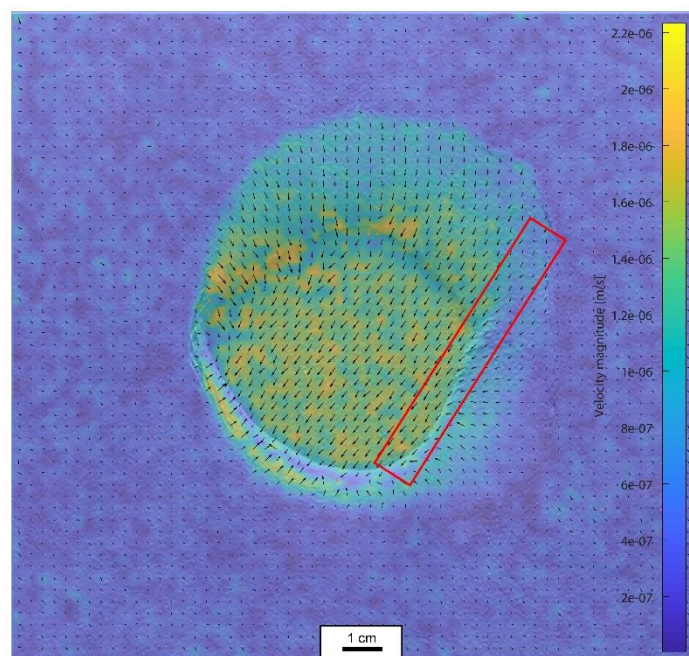
Figure 3.24. DPIV analysis of frame 23 (T=46 minutes of deformation) and frame 24 (T=48 minutes of deformation) of Model-21. Vectors in the red rectangle are parallel to fault strike marking a strike-slip component of displacement (note that vertical displacement is not registered by DPIV analysis). The fault in the red rectangle terminates in the fish-tail shown in Fig. 3.23)

Model-22: Central discontinuity

Model-22 tested the role of a discontinuity in the overburden placed at the exact centre above the analogue magma chamber. Model-22 evolution progressed similar to Model-17, Model-20 and Model-21, presenting a central subsiding piston bordered by outward dipping reverse faults and, afterward by inward dipping normal faults (Fig. 3.25), which connected at depth to the previously formed fault system. Interestingly, no deformation was associated with the discontinuity introduced at the centre of the model. No sign of reactivation was detectable, during deformation, nor at the final stage of modelling deformation. This is confirmed by the high resolution digital elevation model (Fig. 3.26), showing no indication at surface of discontinuity displacement.
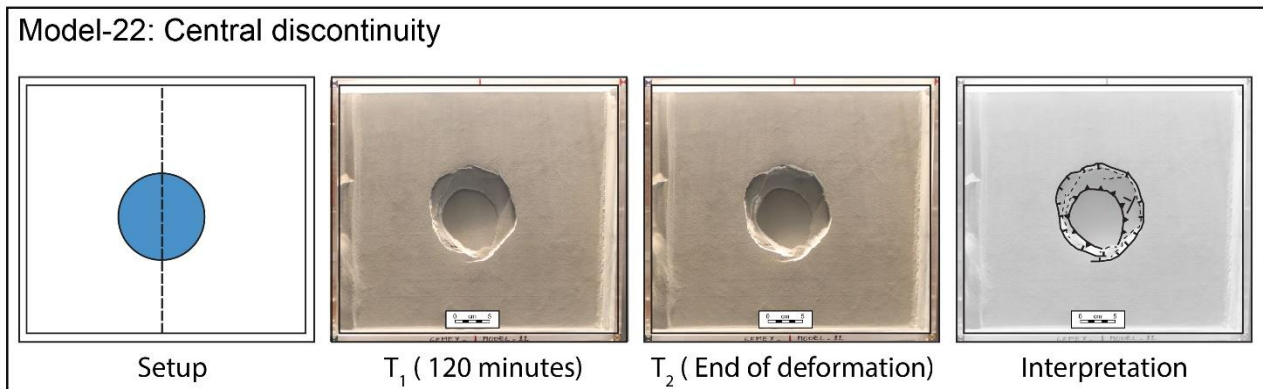
Figure 3.25. Model-22 setup, evolution and interpretation.
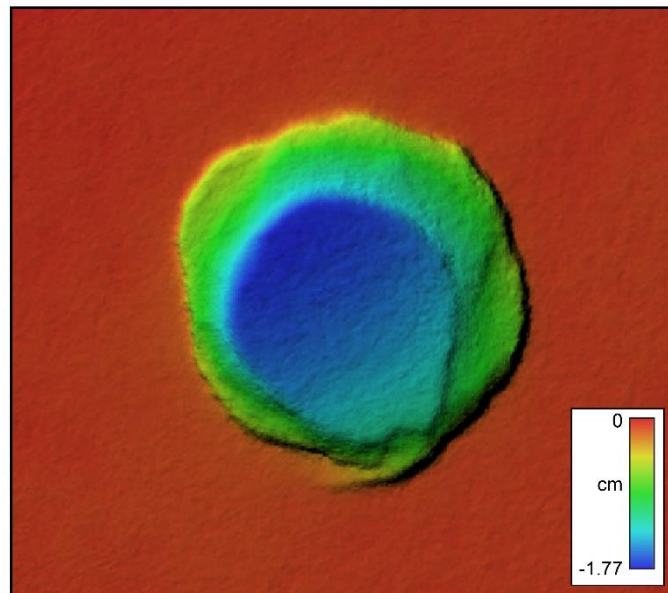
Figure 3.26. Model-22 Digital Elevation Model (DEM) at the final stage of deformation. No evidence for reactivation of inherited discontinuity is visible at the centre of the subsided caldera piston.

Model-23: External discontinuity

Model-23 tested the role of an external discontinuity with respect to the analogue magma chamber. The discontinuity was placed 1 cm outward of the magma chamber. Model evolution started with incipient down-sagging, predating the formation of the outward dipping reverse fault. Deformation then shifted to the outer rim by forming inward dipping normal faults (Fig. 3.27). During caldera collapse the external discontinuity did not influence at all collapse evolution. Only in the final stages it was partly reactivated due to lateral decompression that occurred after piston subsidence. Vertical displacement occurred only in a short sector, linking with the ring fault system (Fig. 3.28). Overall, in Model-23 the external discontinuity is interpreted to not influence the process of caldera collapse.
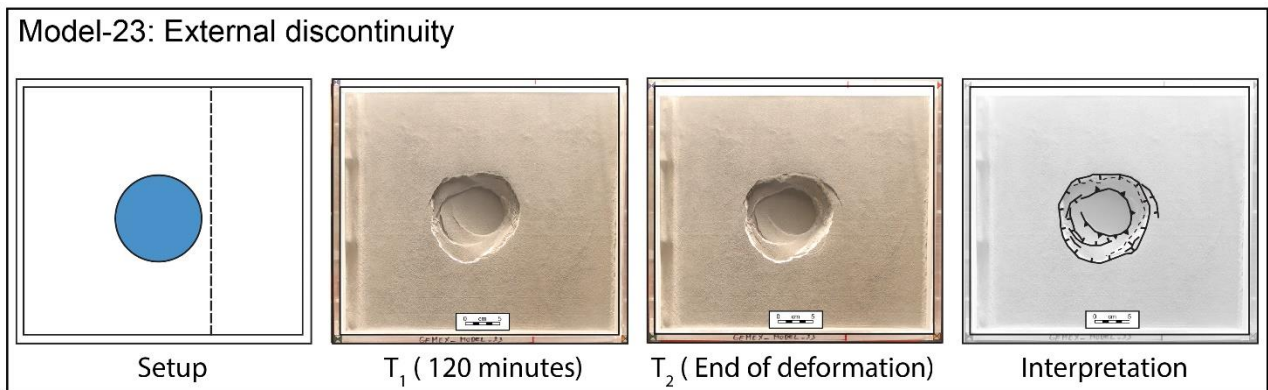
Figure 3.27. Model-23 setup, evolution and interpretation.
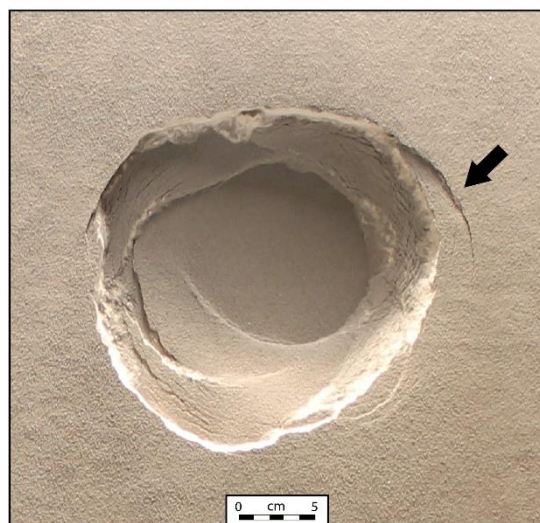
Figure 3.28. Final top-view of Model-23. Black arrow indicates the sector of the inherited discontinuity experiencing passive reactivation, due to lateral decompression.

3.2.3 Sub-series D3.5-2c: Substrate-discontinuity caldera collapse (SDCC)

Five models belonging to sub-series D3.5-2c were selected to show the role of inherited fabrics in the substrate, interacting with the magmatic chamber but not crosscutting the overburden. We reproduced an inherited fault by introducing alternatively one or two rectilinear sides to the magmatic chamber, dipping at 90° or 60° (inward and outward; Fig. 3.29). These rectilinear sides were supposed to mimic normal faults acting as a structural boundary in the substrate for the magmatic chamber. We aimed to investigate how their introduction my influence caldera collapse processes and lead to the final resulting collapse geometry.

Figure 3.29. Setup of models shown for sub-series D3.5-2c

Model-24: Single rectilinear and vertical side

Model-24 tested the role of a discontinuity acting as a boundary for the analogue magma chamber. This discontinuity may simulate an inherited structure is the substrate that does not crosscut the overburden and that therefore only limits the geometry of the magma chamber. To test this, the analogue magma chamber was designed with a rectilinear vertical side, while in the overburden no discontinuities were introduced. Model evolution shown in Figure 3.30 revealed that the rectilinear border of the magma chamber has a strong influence on the caldera collapse process since the beginning of the down-sagging stage: the incipient depression acquired a 'half-moon'-like geometry due to the development of a rectilinear branch of reverse faults bounding the subsiding piston (Fig. 3.31). The outward reverse fault pointed at depth at the analogue magma border that, being in this case rectilinear, forced the reverse fault to propagate following a straight trajectory. Afterwards, when deformation shifted to the external areas, the ring fault was similarly forced to

develop parallel to the reverse fault in correspondence of the faults developed in the subsiding piston to accommodate deformation induced by its asymmetric geometry.
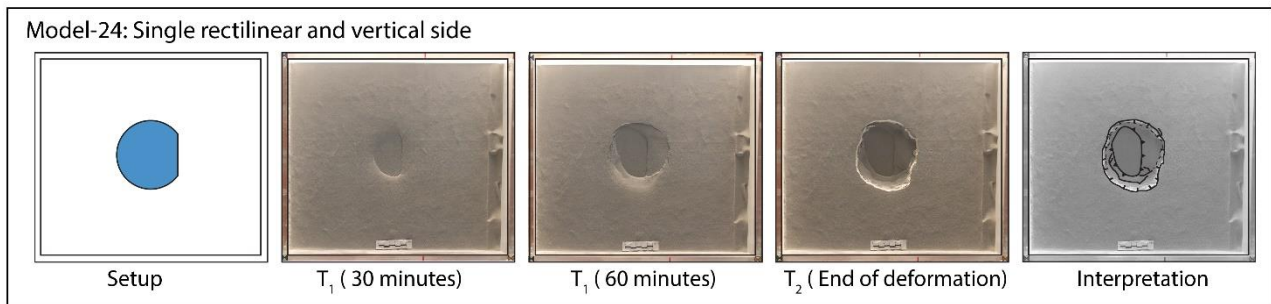
Figure 3.30. Model-24 setup, temporal evolution and interpretation.
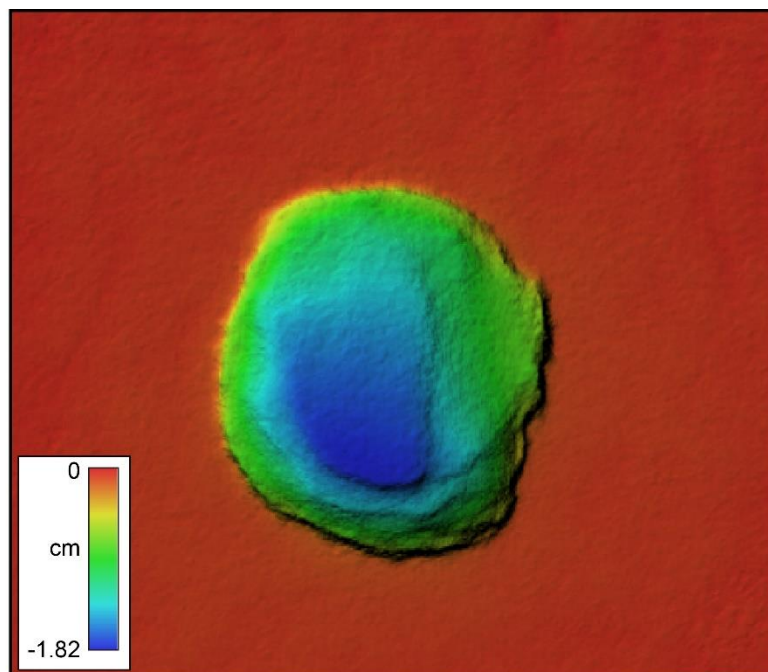
Figure 3.31. Digital Elevation Model (DEM) of Model-24.

Model-30: Two rectilinear and vertical sides

Model-30 was built with a similar setup as Model-24, except for the presence of an additional rectilinear side bounding the analogue magma chamber. The two rectilinear sides intersect with an angle of 90°. As shown in Figure 3.32, model evolution did not differ from the previous one, except for the development of a second couple of revere-normal faults. Incipient collapse of the central caldera piston was accommodated by the formation of two rectilinear reverse faults, while the external ring faults in correspondence of the rectilinear

sides of the analogue magma chamber were forced to mimic the analogue magma chamber shape at depth (Figs. 3.32 and 3.33).
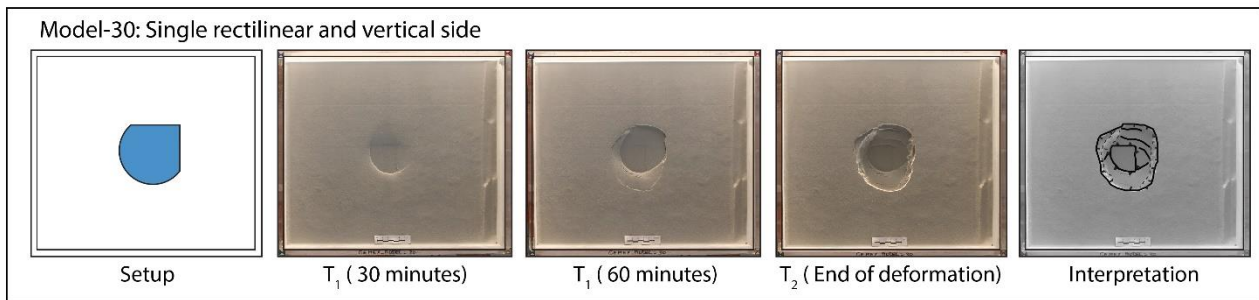
Figure 3.32. Model-30 setup, temporal evolution and interpretation.
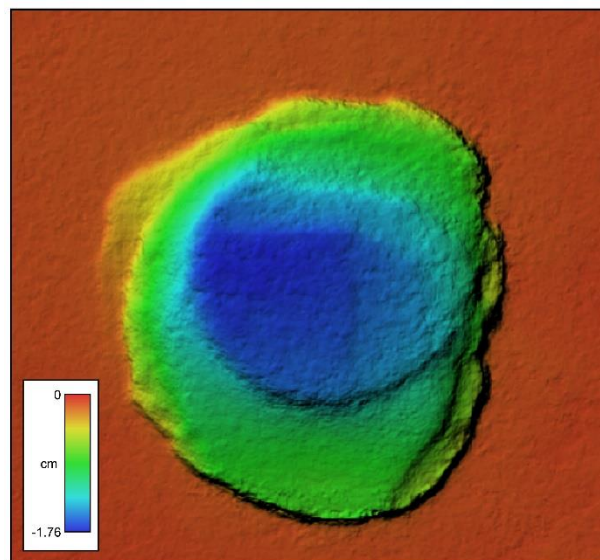
Figure 3.33. Digital Elevation Model (DEM) of Model-30.

Cross sections of Model-30 (Fig. 3.34) showed the same structure as the reference symmetric model (Model-17): outward dipping reverse faults and inward dipping normal faults connecting at depth to the inner fault system; therefore no difference can be inferred. The single structural variation induced by the presence of one/two rectilinear discontinuity in the substrate in which the analogue magma chamber is settled is to force top view geometry collapse at surface.
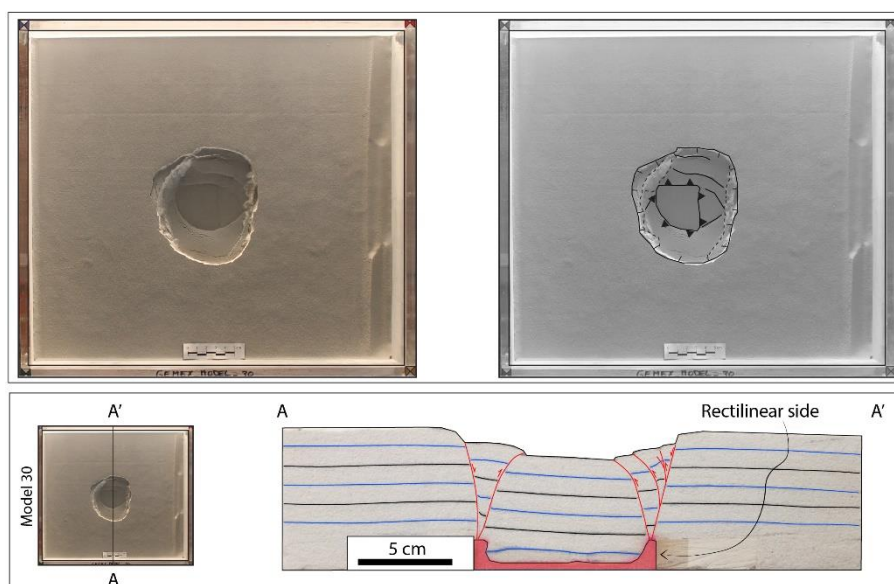
Figure 3.34. Model-30 top view, interpretation and cross section. From section AA' cutting through a rectilinear side of the magma chamber, no difference with the reference symmetric model (e.g. Model-17) can be observed. Rectilinear side did not alter the internal architecture or timing of deformation; rectilinear discontinuity in the substrate simply forced reverse and normal faults to acquire rectilinear propagation trajectory.

Model-36: Single rectilinear side dipping inward (60°)

Setup of Model-36 was similar to Model-24, implying the presence of a single rectilinear discontinuity bounding the magma chamber and simulating an inherited structure in the substrate. Despite this similarity, the discontinuity differs from the one in Model-24 for the dipping angle, which in this case was 60° (i.e., not 90° as in the previous model). The discontinuity plane therefore simulated an inward dipping (60°) inherited structure bounding the analogue magmatic chamber (Fig. 3.35).
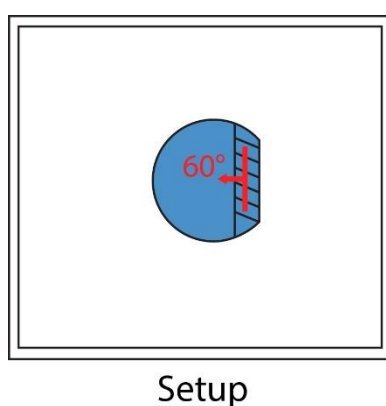
Figure 3.35. Model-36 setup. The analogue magma chamber is bounded at one side by a 60° inward-dipping rectilinear discontinuity. This artificial discontinuity simulates an inherited structure in the substrate.

Model evolution followed a similar pattern as those described for previous models, developing outward dipping reverse faults and inward dipping normal faults. In correspondence of the rectilinear discontinuity at the analogue magma chamber border, the model developed rectilinear reverse and normal faults (Fig. 3.36). Nonetheless, at surface these faults are localized in a more external position owing to projection effect induced by their 60° dipping attitude. Furthermore, secondary reverse structures affected the collapsed piston (Fig. 3.36) that subsided about 1.7 cm (Fig. 3.37).
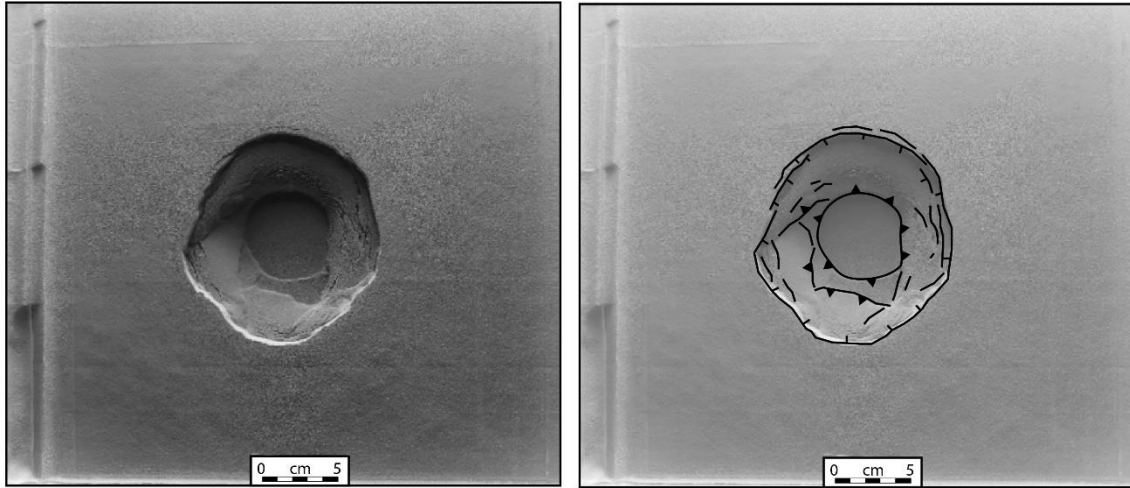
Figure 3.36. Model-36 top view of the final stage of deformation (left panel) and its interpretation (right panel).
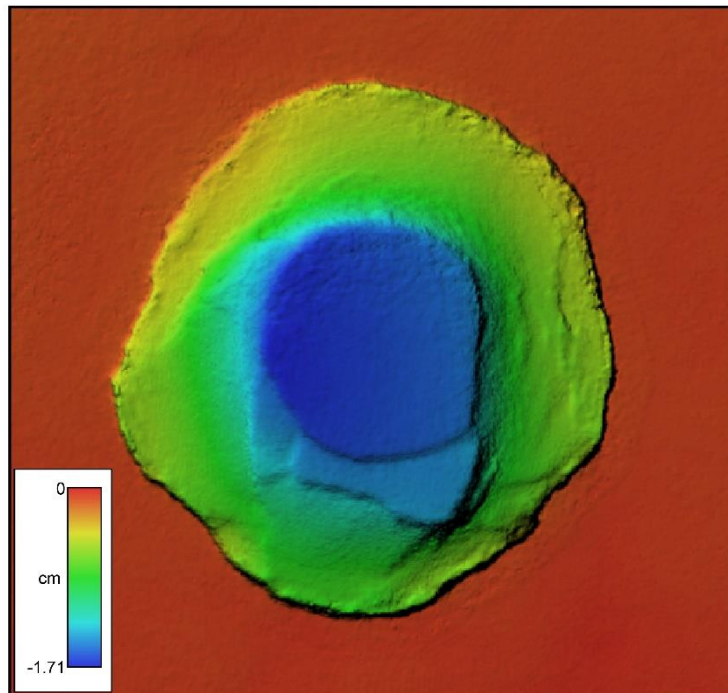
Figure 3.37. Digital Elevation Model (DEM) of Model-36.

Model-37: Single rectilinear side dipping outward (60°)

Model-37 tests the role of a single outward-dipping artificial discontinuity (60°) introduced in the substrate and limiting the analogue magma chamber. Model deformation proceeded throughout time with no substantial variations in comparison to the other models of series D3.5-2c (Fig. 3.38). The introduced discontinuity, yet dipping outward, did not make model evolution differ from the established pattern of deformation. As in the other cases, the rectilinear side localized deformation developing as a normal fault forming the caldera ring at the final stages of model deformation. DEM reconstruction highlights well the rectilinear features of this model (Fig. 3.39).
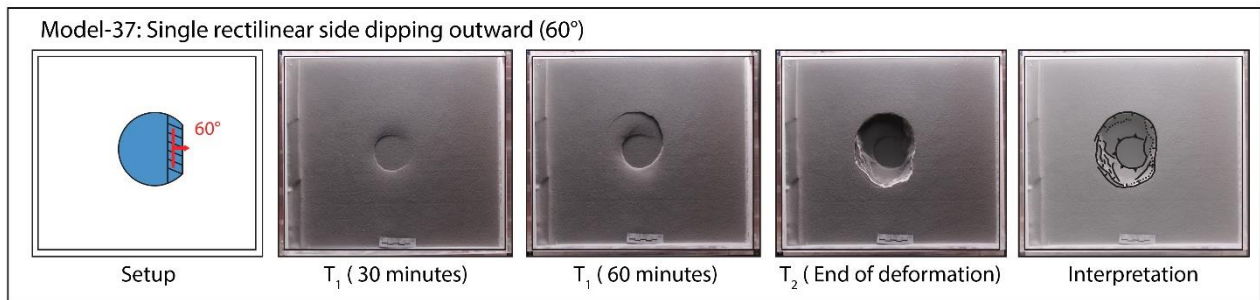
Figure 3.38. Setup, temporal model evolution and interpretation of Model-37. An outward dipping (60°) discontinuity bounds the analogue magma chamber, simulating the presence of an inherited structure in the substrate.
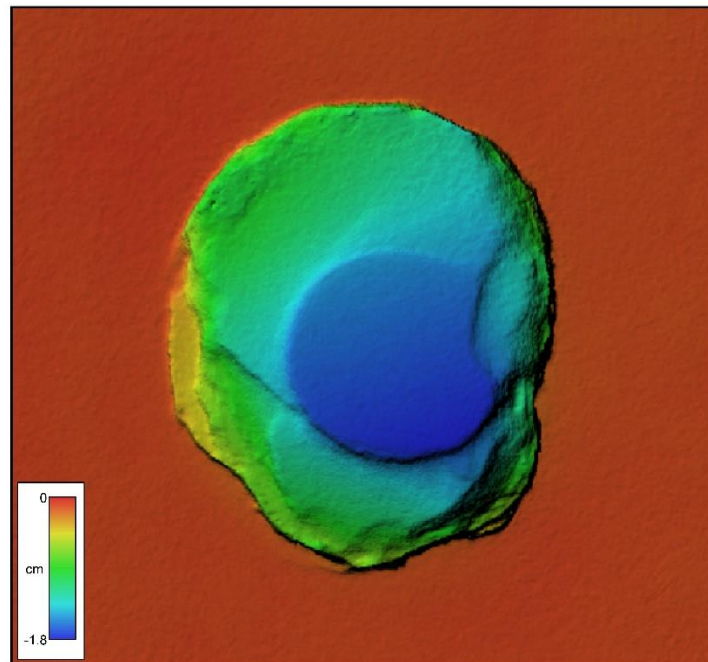
Figure 3.39. Digital Elevation Model (DEM) of Model-37.

Model-39: Single (internal) rectilinear side dipping inward (60°)

This model reproduces the setup of Model-36 but the rectilinear side was placed in a more internal position inside the analogue magma chamber, to investigate the effect of discontinuity position during caldera collapse. As for Model-24, Model-30, Model-36 and Model-37, the rectilinear discontinuity localized the deformation and forced the model to develop rectilinear reverse/normal faults. No visible effects related to the dipping angle (60° or 90°) were observed (Fig. 3.40). In this model, the dip of the introduced discontinuity simply controlled the trajectory of fault development. The position of the discontinuity (i.e., in this case localized in a more internal position) influenced the final shape of the model, which lost the circular plain view geometry and assumed a more elongated shape, as highlighted by DEM elaboration (Fig. 41).
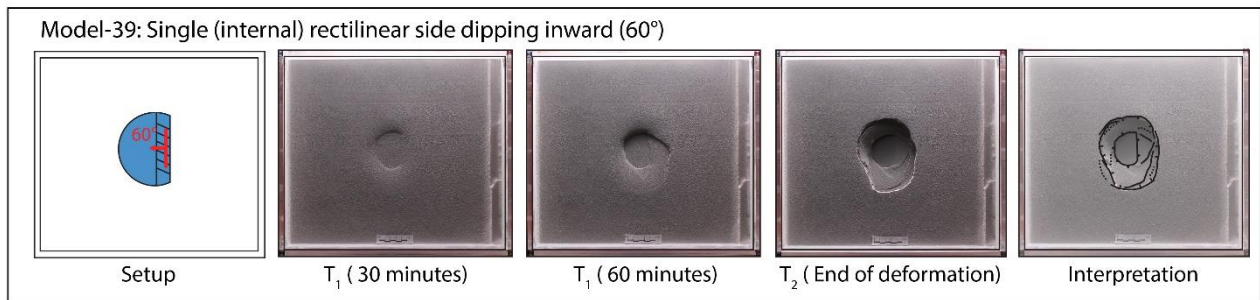
Figure 3.40. Setup, temporal model evolution and interpretation of Model-39. An inward dipping (60°) artificial discontinuity bounds the analogue magma chamber, as in Model-36, but the discontinuity is localized in a more internal position with respect to Model-36.
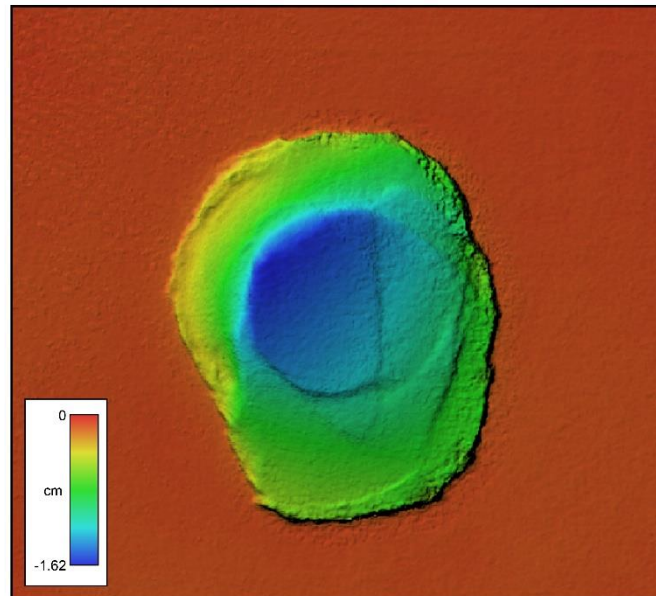
Figure 3.41. Digital Elevation Model (DEM) of Model-39.

3.2.4 Sub-series D3.5-2d: Substrate to Overburden-discontinuity (OSDCC)

Sub-series D3.5-2d aimed to investigate the role of inherited faults crosscutting the substrate (all of it or part of it), as well as the overburden and directly derive (except for Model-76) from setup of Series D3.5-2c. We placed straight artificial discontinuities in the overburden in continuity with the substrate fault to create a single inherited structure extending from the substrate and reaching the surface (or stopping below it, in the case of Model-76). We reproduced one/two discontinuities intersected with a 90° angle, and having 90° and 60° inward/outward dipping attitude.
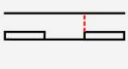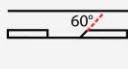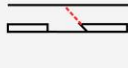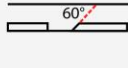
MODEL SETUP

MODEL #			SETUP DESCRIPTION
Model-25			**Rectilinear side (90°) + sand pre-cut**
Model-32			**Two Rectilinear sides (90°)+ sand pre-cuts**
Model-35		60°	**Rectilinear side (inward-60°) + sand pre-cut**
Model-38			**Rectilinear side (outward-60°) + sand pre-cut**
Model-40		60°	**Rectilinear side (internal, inward-60°) + sand pre-cut**
Model 76			**Rectilinear sides + sand pre-cuts not reaching surface**

Figure 3.42. Setup and short description for models of sub-series D3.5-2d.

Six models (Model-25, Model-32, Model-35, Model-38, Model-40, and Model-76) were selected as representative for this experimental series and are presented and described below (Fig. 3.42).

Model-25: Single rectilinear vertical side + vertical discontinuity in the overburden

Model-25 setup is a modification of Model-24 setup. In correspondence of the substrate discontinuity we placed a brittle discontinuity in the overburden. This cut in the brittle overburden was the continuation of the substrate discontinuity and therefore simulates an inherited structure that affects both substrate and overburden. Model deformation is rather different from that of the standard symmetric Model-17 and from Model-24. As visible from temporal deformation sequence in Figure 3.43, after the down-sagging phase, the inherited discontinuity was promptly reactivated as a vertical and rectilinear normal fault, inhibiting the development of the reverse fault that generally developed with a rectilinear trajectory. In this case the

overburden discontinuity localized the total amount of deformation on that caldera side, leading to a rectilinear and vertical border (Figs. 3.43 and 3.44). Besides, in the other areas of the collapsing caldera, the evolution followed the standard deformation pattern, given by the development of outward dipping reverse fault at the caldera centre and inward dipping normal fault at the boundary.
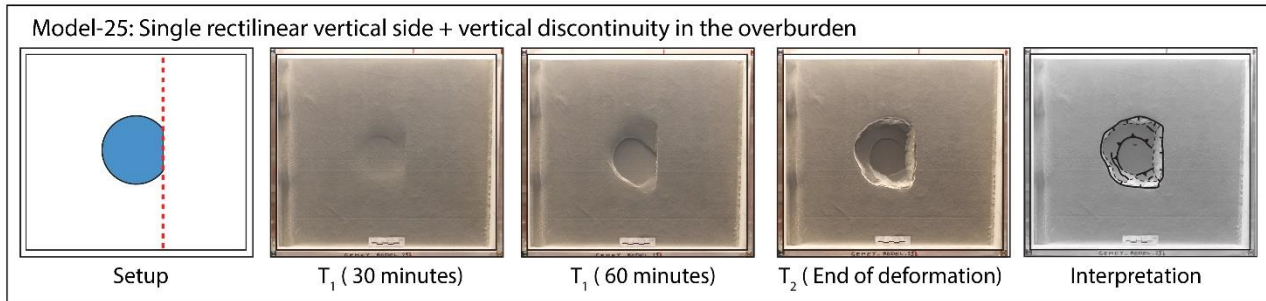
Figure 3.43. Setup, temporal evolution and interpretation of Model-25.
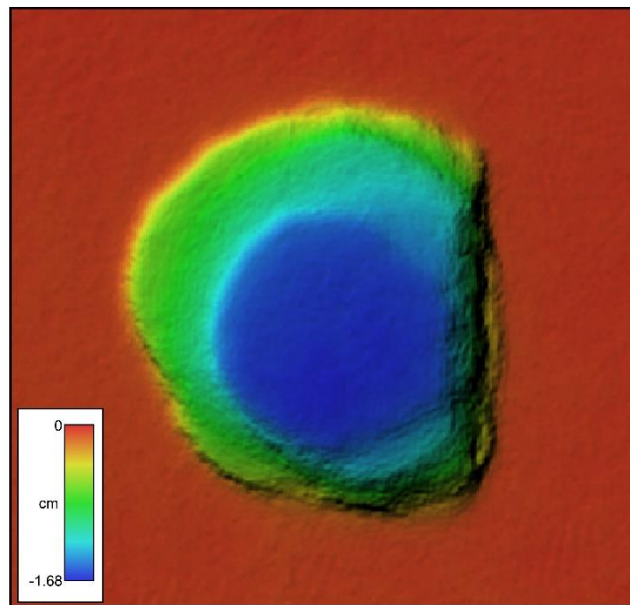
Figure 3.44. Digital Elevation Model (DEM) of Model-25.

Model-32: Two rectilinear vertical sides + vertical discontinuities in the overburden

Model-32 derived from a variation to Model-30 setup, by the addition of two rectilinear discontinuities cut in the brittle overburden with the DA, in correspondence of the substrate discontinuity (as previously described for Model-25). Development of Model-32 followed the same pattern of deformation as Model-25, by developing rectilinear vertical normal faults in correspondence of the brittle discontinuities. As in the case of Model-25, the presence of the brittle discontinuity inhibited the formation of the outward dipping reverse

faults, that only developed in the areas where no discontinuities were introduced (Fig. 3.45). This aspect of deformation is extremely evident observing the model cross sections. Specifically, Figure 3.46 shows a cross section of Model-25 cut orthogonal to one of the two discontinuities: on the side of the collapsed caldera correspondent to the cut in the brittle overburden, no outward dipping reverse fault bounding the central subsided piston is visible. Besides, a reverse fault is visible on the opposite side, where no discontinuities were introduced.
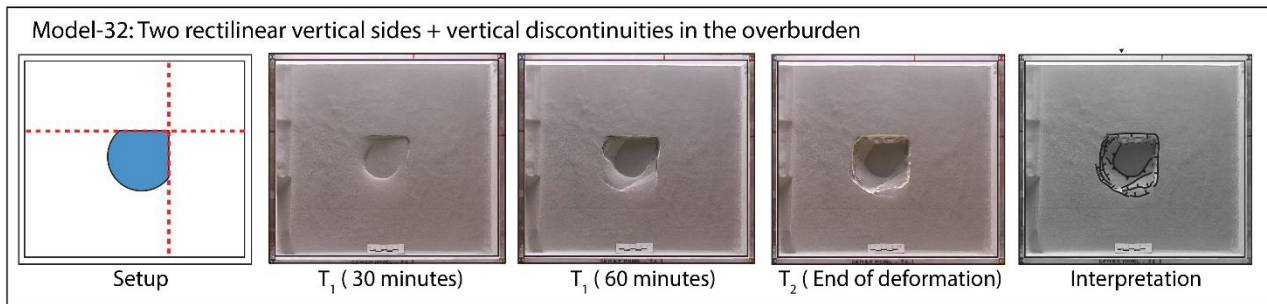
Figure 3.45. Setup, temporal evolution and interpretation of Model-32.

The absence of the reverse faults was due to the reactivation of weak zones created by the cut in the brittle overburden that localized the deformation leading to a vertical (in section) and rectilinear (in top view) normal fault. Digital Elevation Model of Model-32 (Fig. 3.47) clearly shows the absence of reverse faults in correspondence of the introduced discontinuities. In comparison to Model-25, Model-32 has two rectilinear sides instead of one.
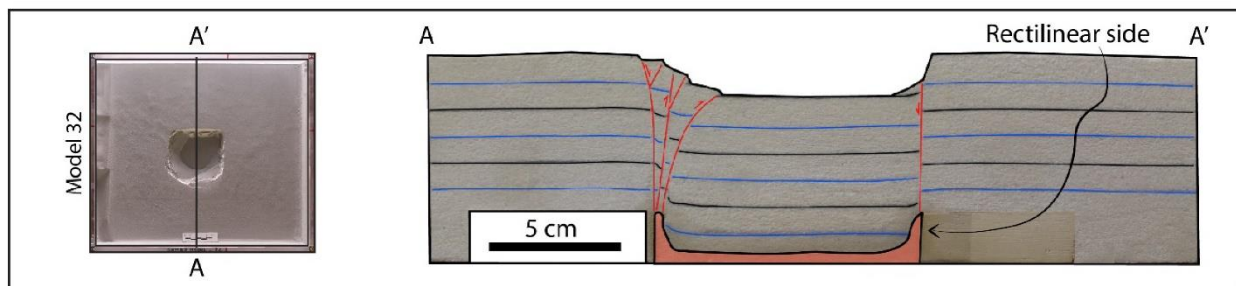
Figure 3.46. Top view and interpreted cross section of Model-32.
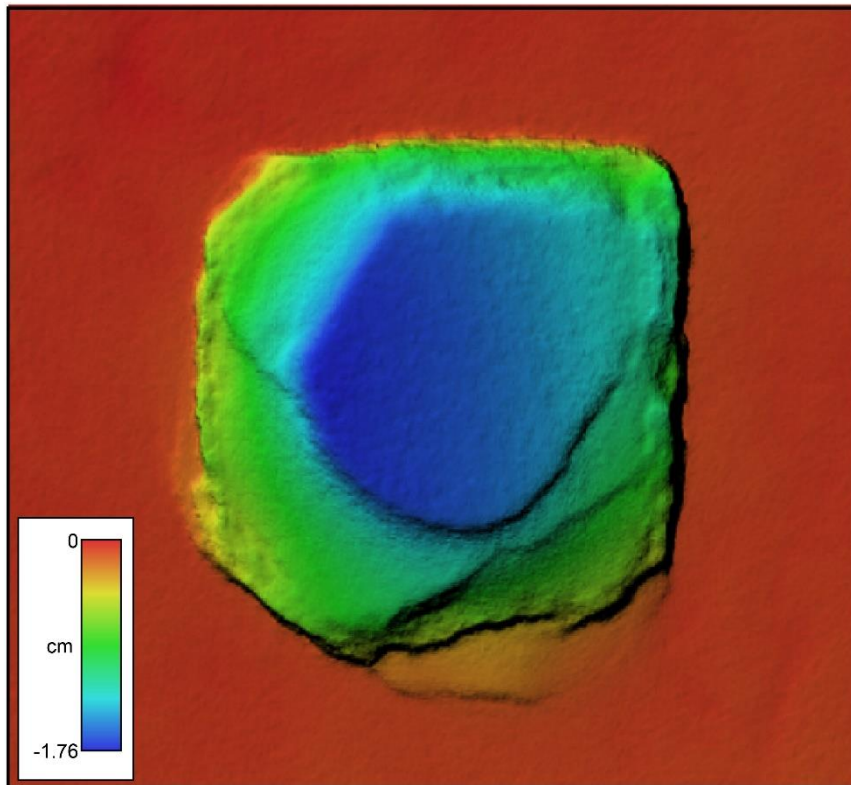
Figure 3.47. Digital Elevation Model of Model-32.

Model-35: Single rectilinear inward dipping (60°) side + 60° dipping discontinuities in the overburden

Model-35 has a similar setting to Model-36, therefore having a single 60° inward-dipping rectilinear discontinuity in the substrate. In addition, as for Model-25 and Model-32, the discontinuity was extended to include both the brittle overburden and the substrate and with the same angle (60°). In this case, the presence of the discontinuity in the brittle overburden did not lead to the same deformation pattern observed in Model-32 (Fig. 3.48), as reverse fault formation was not inhibited by discontinuity reactivation and the collapsed caldera presented the same geometry as Model-36, with a rectilinear reverse fault bounding the subsiding piston and a rectilinear inward-dipping normal fault constituting the ring fault. This effect was likely due to discontinuity dip. The 60° of dip also affected the length of the rectilinear side constituting a branch of the ring fault: surface projection causes the fault to be rather smaller and the rectilinear portion of the ring fault to link with the remnant ring fault system with a curvilinear trajectory (Fig. 3.49).
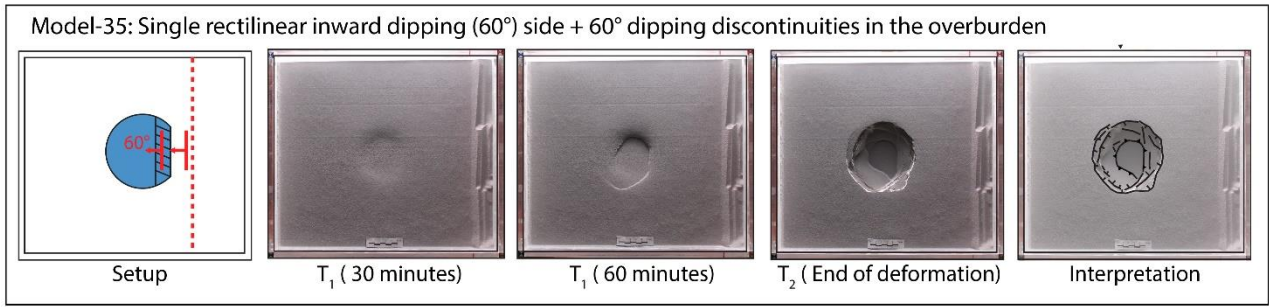
Figure 3.48. Setup, temporal evolution and interpretation of Model-35.
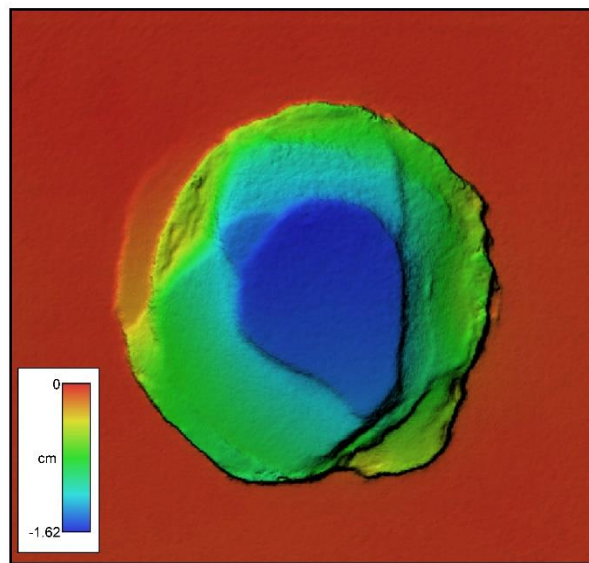
Figure 3.49. Digital Elevation Model (DEM) of Model-35.

Model-38: Single rectilinear outward dipping (60°) side + 60° dipping discontinuity in the overburden

Model-38 was designed with a setup similar to Model-37, with the addition of a 60°outward-.dipping brittle discontinuity cut in the overburden in continuity with the substrate discontinuity. No evidence of fault pattern variations was observed with respect to Model-37: Model-38 developed a rectilinear reverse fault (Figs. 3.50 and 3.51) in the subsiding piston and a rectilinear inward-dipping normal fault connected to the ring fault system and bounding the collapsed caldera. The overall shape of the caldera was elongated, with the major axis striking parallel to the discontinuity trend direction.
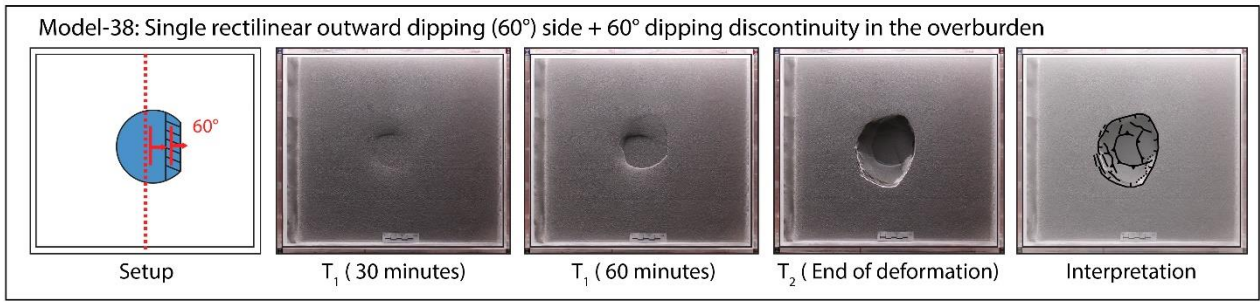
Figure 3.50. Setup, temporal evolution and interpretation of Model-38.
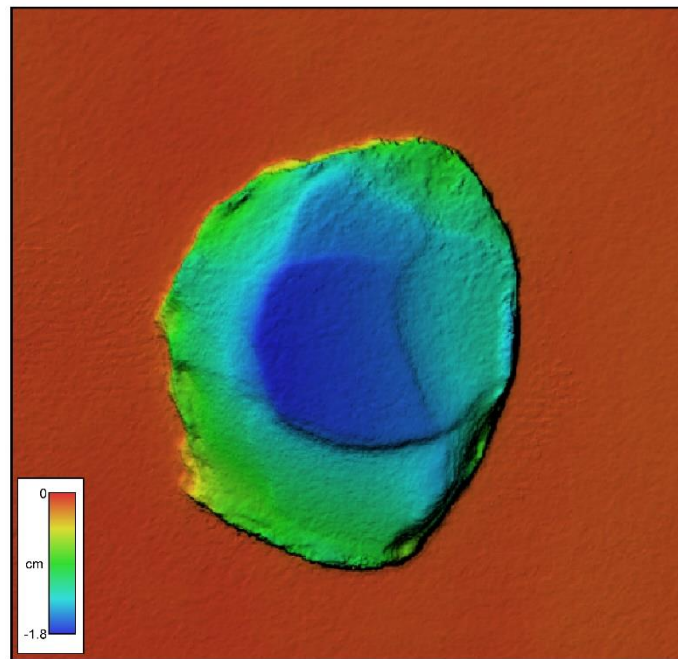
Figure 3.51. Digital Elevation Model (DEM) of Model-38.

Model-40: Single rectilinear (internal) inward dipping (60°) side + 60° dipping discontinuities in the overburden

Model-40 was run with a similar setup to Model-39, with the addition of the discontinuity cut in the brittle overburden. The artificial discontinuity, as for the other models, represents a 60°-dipping extension of the substrate discontinuity, already tested in Model-39. Compared to Model-35, both discontinuities were placed in a more internal position with respect to the analogue magma chamber. Model evolution (Fig. 3.52) progressed similar to Model-35, developing a rectilinear outward-dipping reverse fault and a rectilinear inward-dipping normal fault in correspondence of the introduced discontinuity (Fig. 3.53).
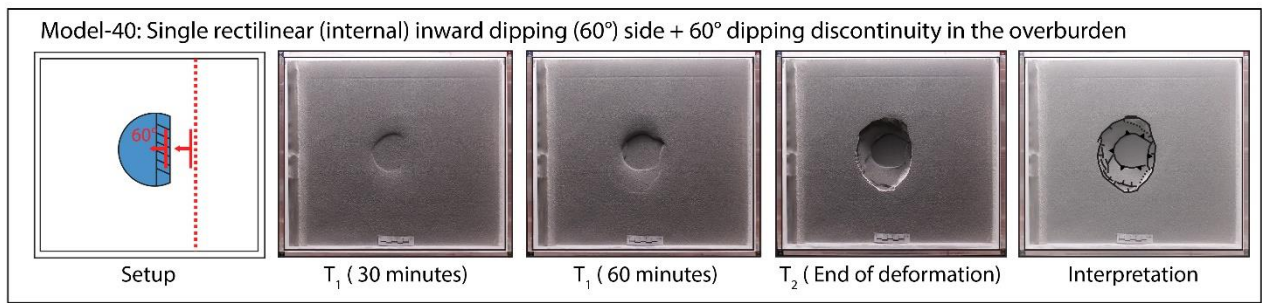
Figure 3.52. Setup, temporal evolution and interpretation of Model-40.
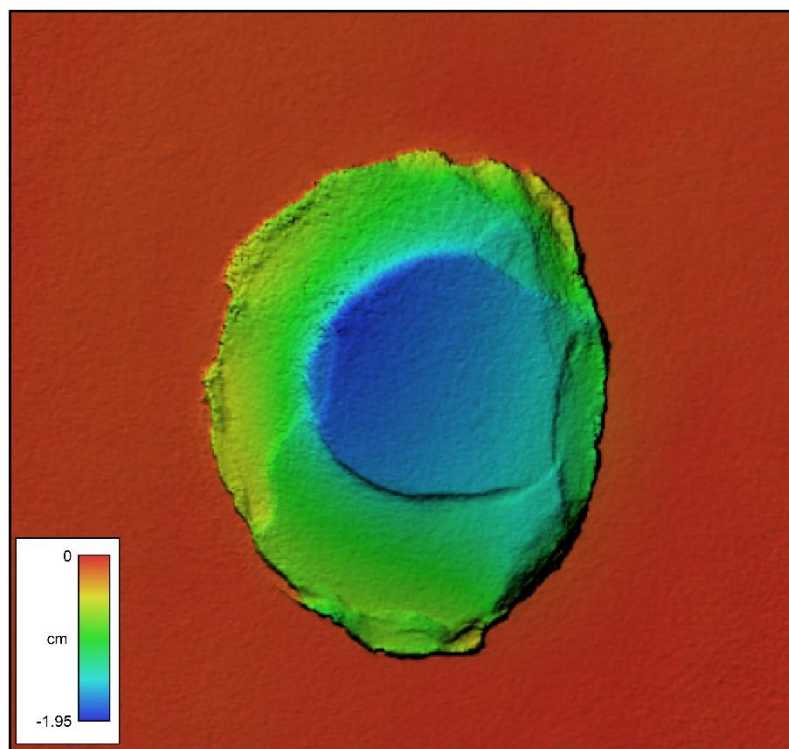

Figure 3.53. Digital Elevation Model (DEM) of Model-40.

Model-76: Two rectilinear vertical sides + vertical discontinuities in the overburden + single central vertical discontinuity not reaching the topographic surface

Model-76 resulted from combination of various setups and aimed at testing specific hypotheses proposed by team working for WP4 (Liotta and WP4 Working Group, 2019; see Fig. 1.5). Particularly, we aimed to test the hypothesis of reactivation of inherited structures bounding the caldera collapse at Los Humeros, and the presence of intra-caldera discontinuity reactivation. Both kinds of structures represented inherited faults that were supposed to crosscut only the overburden pile beneath the volcano-clastic deposits and lava-flows.

Accordingly, we designed the setup with two discontinuities bounding the analogue magma chamber in the substrate and extending upward in the brittle overburden to reach a depth of 2 cm below the model surface. In addition, we placed a third central discontinuity above the analogue magma chamber, reaching again a depth of 2 cm below the model surface (Fig. 3.54).
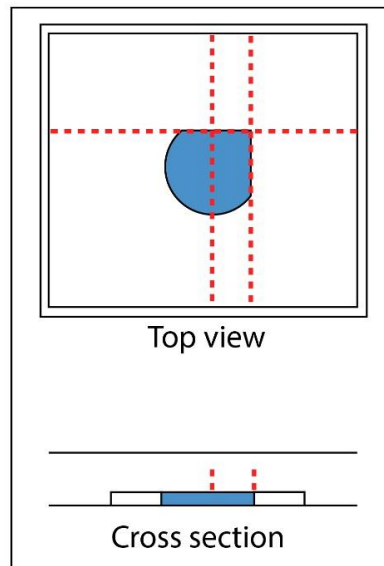
Figure 3.54. Setup of Model-76. This setup was designed to test the possible role on caldera collapse process of two artificial discontinuities in the substrate and partly affecting the overburden, but being sealed by brittle material representing the volcanic deposits. A third discontinuity with the same characteristics was placed above the analogue magma chamber, in a central position. Red dashed lines indicate overburden discontinuity position.

This set up is by far the most complicated designed in Series D3.5-2 and the pattern of deformation reflects this complexity. Temporal evolution (Fig. 3.55) showed some variations when compared to Model-24, Model-25, Model-30 and Model-32. Specifically, Model-76 developed a subsiding piston that was bordered by outward-dipping reverse fault following a circular trajectory where no discontinuities were introduced. Also, the model developed a rectilinear reverse fault on the two sides where the artificial discontinuities were placed. Deformation then shifted to peripheral areas and inward-dipping normal faults began to propagate.
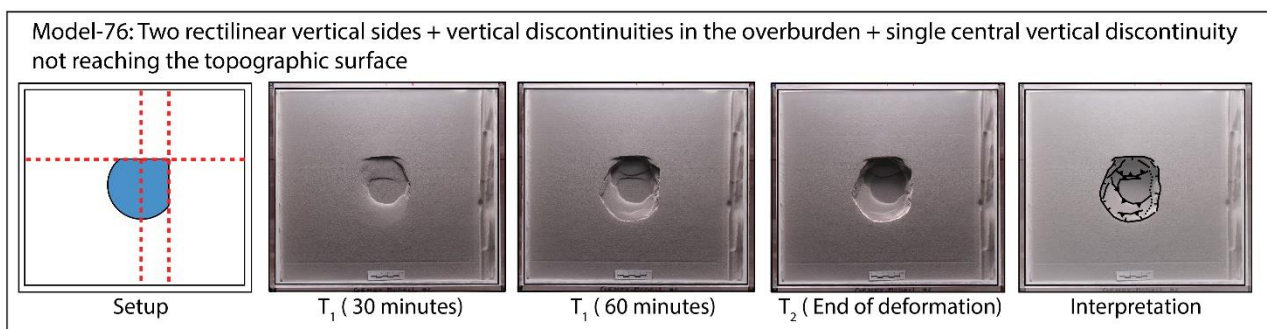
Figure 3.55. Setup, model evolution and interpretation of Model-76.

These faults were not completely vertical, and in the shallow portion of the model (see cross section in Fig. 3.56) varied their dip angle. This aspect is strictly dependent on the absence of the inherited discontinuity in the undeformed 2 cm-thick layer at the model top. At depth, inherited discontinuities were reactivated, while at shallow levels, where the brittle discontinuity stopped, fault propagation was forced by weak frictional properties of analogue material to break according to Coulomb criterion, leading to a fault dipping with a smaller angle. Surface deformation was then accommodated by secondary faults. Regarding the role of the central discontinuity, the latter has not played a significant role during caldera collapse. Central piston subsidence was accommodated by lateral faults, and this inherited structure remained inactive. Confirmation of this evolution is supported by the high resolution Digital Elevation Model (DEM) elaborated for Model-76 and shown in Figure 3.57.
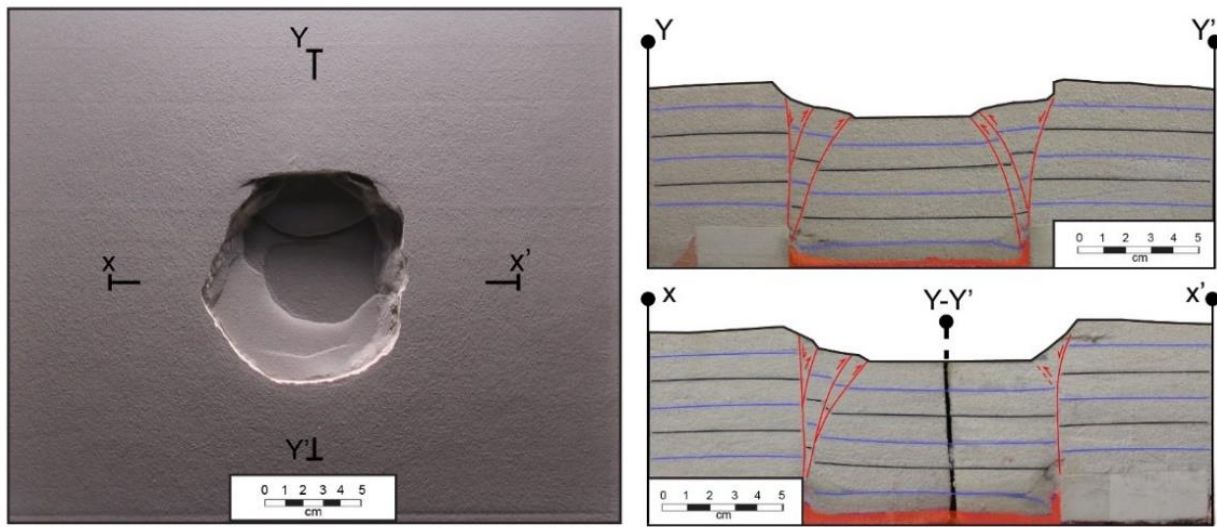
Figure 3.56. Top view and cross section interpretation of Model-76.
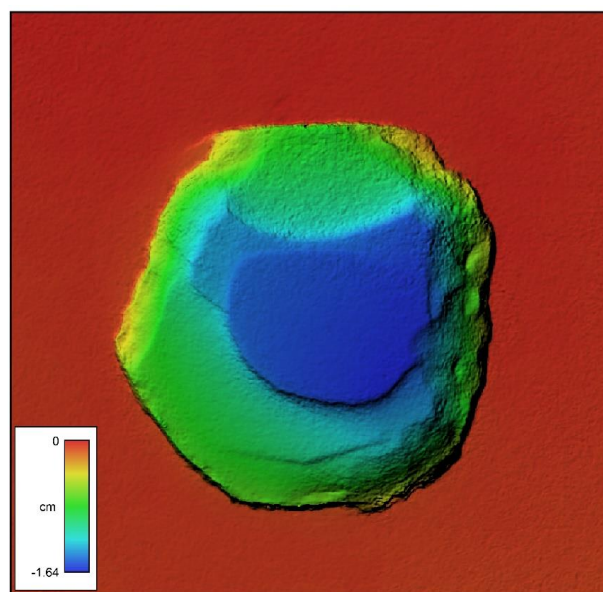
Figure 3.57. Digital Elevation Model (DEM) of Model-76.

4 Discussing the interactions between regional tectonics and volcanoes

In the following sections we discuss the modelling results of experimental series 3.5-1 and 3.5-2, and we then compare them with the natural cases of interest (the TMVB and Los Humeros and Acoculco volcanic systems). Specific discussion of modelling of Series 3.5-1 is given in Section 4.1 while Series 3.5-2 is discussed in Section 4.2. A comparison with the natural cases is discussed in Section 4.3, where insights from analogue models into the evolution of the Los Humeros and Acoculco volcanic systems are described.

4.1 Time-space deformation pattern of a continental rift propagating across existing crustal faults

The aim of Series D3.5-1 was to investigate whether a propagating rift may interact with previously formed discontinuities, simulating pre-existing crustal faults. Before discussing any implication for natural cases it is useful to describe the reliability of the realized models. In general terms, the correct scaling guarantees for valuable comparison between models and nature. In fact, the setup correctly reproduces in terms of thickness, density distribution and mechanical properties the lower (LC) and upper crust (UC) in the TMVB. Length and throw of faults are correctly scaled, having the first a maximum value of ~ 10 cm (scaling to maximum 15 km in nature) and the second a maximum values of few millimetres (scaling to few hundreds of meters in nature). Top view geometry of fault is reliable, faults being organized in graben systems showing an average width of 2.5 cm (scaling to ~35-40 km in nature). Distribution and chronology of fault formation is in agreement with what expected from the adopted modelling strategy: the rotational nature of the modelling setup implies a gradient of deformation developing from the opposite position of the poles of rotation and propagating toward them, with a gradient in vertical fault displacement that is consistently higher in the left-lateral area of the models (where cumulative deformation is larger) and smaller in the model area adjacent to the poles of rotation, which experience low deformation. Velocity vectors reproduce well the prospected natural processes. Large scale DPIV analysis performed on the area of interest of target models (Fig. 4.1a, b) shows a gradient of velocity vector modules that decreases toward the poles of rotation, vectors being null at the centre of the model (Fig. 4.1c,d,f). Graph in Figure 4.1e indicates a decrease in deformation velocity along trace B-B' (see Fig. 4.1c) in the proximity of the poles of rotation. Vectors direction here marks particle movements toward the centre of the model, a deformation pattern that is likely due to counter-rotation of the mobile plates close to the rotation poles, but that does not affect the development or the evolution of structures in the area. The direction of vectors highlights the presence of a boundary effect in the left-lateral side of the area of interest, which is likely due to rubber sheet compression

along the direction of rift propagation (black arrows in Fig. 4.1a,b,c). This effect is negligible since it affects an area of the model that is not of interest.
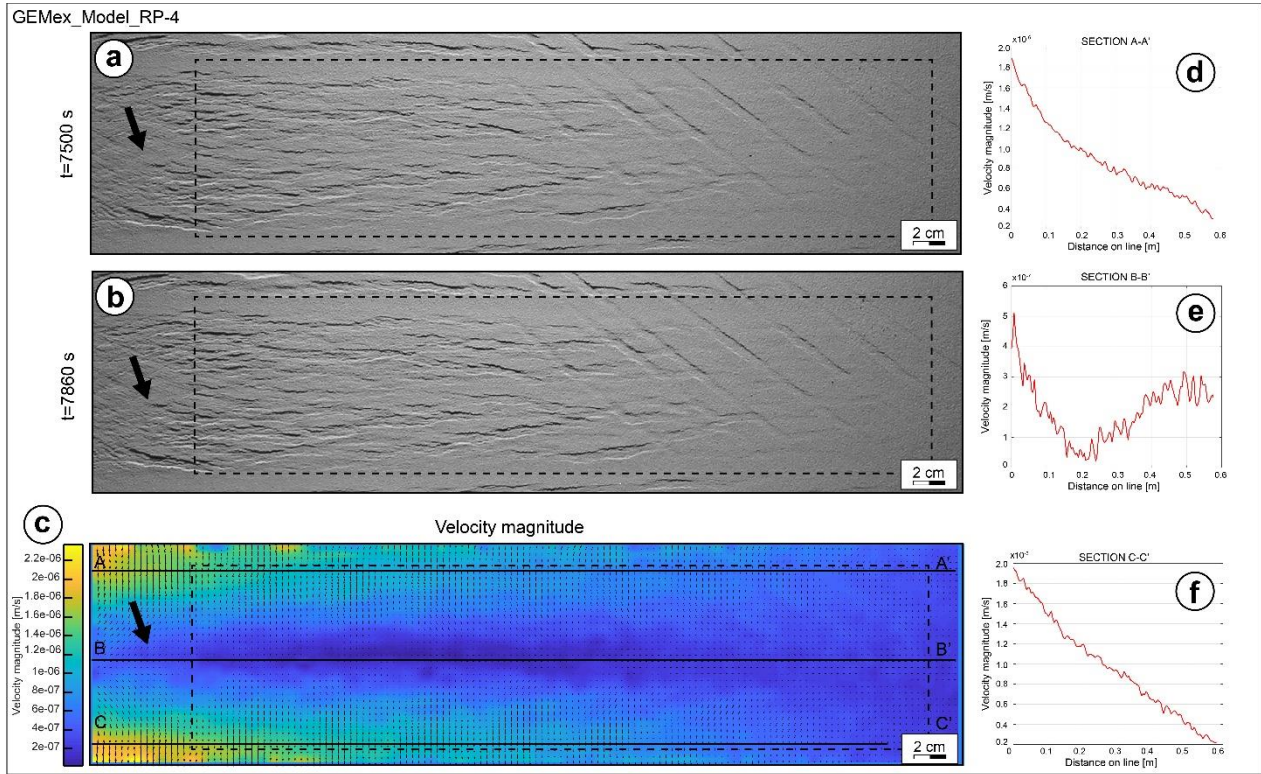
Figure 4.1. Digital Particle Image Velocimetry analysis (DPIV) of Model RP-4. (a and b) show the two frames (t= 7500 s and t=7860 s) from which DPIV analysis shown in (c) was calculated. (c) Velocity magnitude overlaid by velocity vectors. Warmer colours denote higher velocities, while cooler colours indicate lower velocities. Dashed polygons in (a), (b) and (c) mark the area of interest. (d-f) show velocity graphs along traces A-A', B-B', and C-C'. Trace location is shown in (c). Elaboration in (c), (d), (e) and (f) were elaborated with PIVlab algorithms (Thielicke and Stamhuis, 2014).

Considering the entire series (Model RP-1 to Model RP-9), model development followed -at first order of observation- the same evolution. Chronology of fault development is similar through the series, as well as fault density and dimension. The average trend of rift-related structure is approximately N90° and it is constant in all the performed models. Similarly, fault trace distribution respected the same trend throughout the various models of the series. This is an indication of model reproducibility, and allows for further model comparisons taking into account model differences. Those are mainly represented by reactivation of inherited structures introduced before deformation into the model setup as weak zones, obtained by cutting through the 1 cm-thick layer of Qz-Kfeld sand mixture, simulating the brittle UC. The variously oriented artificial discontinuities (see Tab. 4.1) responded (or not) to model deformation as a function of the angle to the direction of propagation. Model RP-1 setup was built with no discontinuities, and model RP-2 and RP-3 were built with only one set (respectively indicated as S1 in Model RP-2 and S2 in Model RP-3). The other models (Model RP-4 to Model RP-9) were built with different trends for the two sets of discontinuities S1 and S2, ranging from high angle to low angle with respect to the direction of rift propagation. When

compared to the other models, Model RP-2 and Model RP-3 indicate that there was no reciprocal influence of the two sets. As an example, the orientation of one did not influence the development of the other, whichever the trend of the two sets of artificial discontinuities. Being the setup designed to have a symmetrical opening of the MPs (as also shown by velocity vectors obtained with DPIV analysis; see Fig. 4.1c), the rift-related structures developed similarly on both mobile plates, so did the inherited structure when introduced symmetrically with respect to the VD below the rubber sheet (i.e., Model RP-6 and RP-8). What induces the reactivation of a set of discontinuities is simply the favourable or disadvantageous orientation with respect to the stress field induced by rifting propagation and deformation. Modelling results are summarised in Table 4.1, and show for which angle α and β discontinuity sets are reactivated.

Model Name	Azimuth of S1 (α) [°]	Azimuth of S2 (β)[°]	S1 reactivation	S2 reactivation
RP-1	/	/	/	/
RP-2	30	/	NO	/
RP-3	/	125	/	YES
RP-4	30	125	NO	YES
RP-5	45	135	YES	YES
RP-6	60	120	YES	YES
RP-7	15	165	NO	NO
RP-8	75	105	YES	YES
RP-9	90	180	YES	NO

Table 4-1. Table summarizing the models belonging to Series D3.5-1 and showing which sets of artificial discontinuities were reactivated during model deformation.
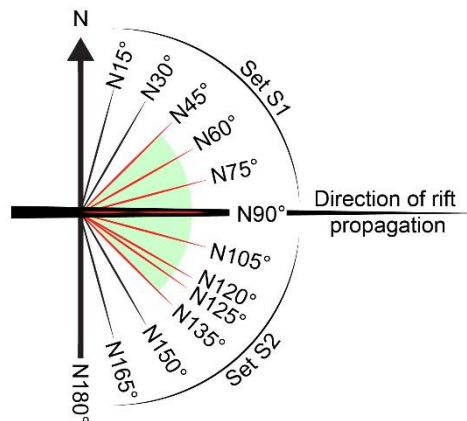
Figure 4.2. Angles of reactivations for discontinuities tested in Series D3.5-1. Green area and red lines mark the strike angles for which discontinuities belonging to sets S1 and S2 were reactivated.

Only discontinuity sets having an angle to the rift direction of propagation <45° (i.e., striking between N45° and N135°) were reactivated (Tab. 4.1, Fig. 4.2), in agreement with the local stress field imposed by model deformation (S_{Hmin} extentional and orthogonal to the rift axis) (e.g., Ranalli & Yin, 1990). For angles α and β <45° and >135° we did not observe reactivation of weak zones. Discontinuity reactivation is therefore dependent on the local stress field, but a factor of interest is to understand which kind of deformation the reactivated structures experienced. Observing model top views, one can infer that not all the reactivated structures experience the same type of deformation. In particular, in Model RP-3 and Model RP-4, reactivated structures were evident and formed quite narrow and discontinuous grabens, displacing rift-related structure propagation, while in Model RP-8 grabens associated with the reactivation of inherited discontinuities were wider and continuous (reaching more than 20 cm in length). What is similar between the reactivated structures in all the models is the presence of a couple of conjugate normal faults (i.e., constituting the grabens) that formed during model deformation. Regarding the artificial inherited weak zones, it is worth noting that they were simulated by cutting through the 1 cm- thick sand mixture layer (Fig. 4.3a). The cut reoriented sand particles, creating a weak zone of about 0.5-0.8 mm, with the two weak zone boundaries giving rise to the couple of normal faults that resulted in a graben system (Fig. 4.3b).
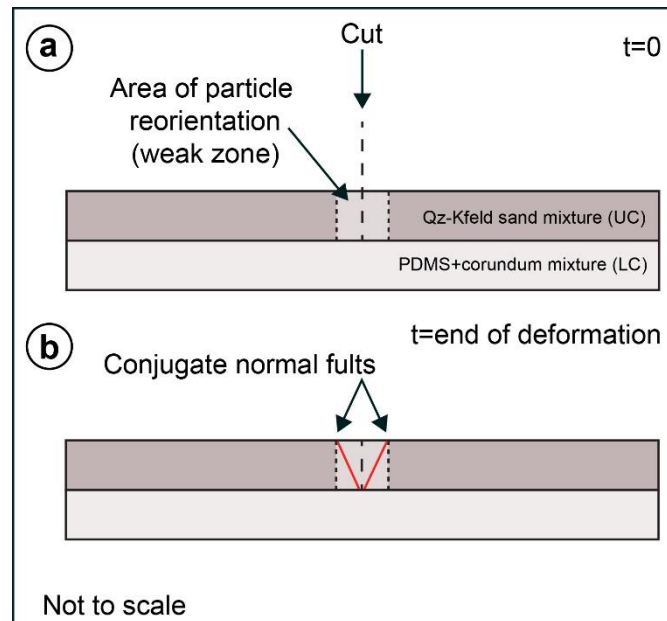
Figure 4.3. Sketch showing (a) the area experiencing particle reorientation due to sand layer cutting, and (b) the relation between the resulting normal faults and the predetermined weak zone. UC: Upper Crust; LC: Lower Crust.

Nonetheless, the width of the grabens is not equal in the various models: while in Model RP-4 grabens are narrow, in model RP-8 they are extremely wide, likely as a consequence of a more favourable orientation with respect to the extensional stress field. Experiencing a dilation, rather than shear slip, may be an

important feature when studying migration of fluids through secondary permeability, therefore the observed characteristics are extremely interesting. In order to investigate this aspect, it was possible to test the tendency of target structures to experience slip or dilation, given a certain stress field, using FracPaQ algorithms.

Slip tendency (T_S) defined by Morris et al. (1996) is the ratio of the shear stress (τ) on the normal stress (σ_n) acting on a given fracture. Knowing the value of two principal stresses and the orientation of one of them, it is possible to compute the 2D equivalent of the Slip tendency (T_S) on fracture planes (Healy and Rizzo, 2018). In the same way, it is possible to calculate the Dilation tendency (T_d; Ferril et al., 1999) defined as the ratio (σ_1-σ_n)/(σ_1-σ_3).

In our model setup we simulated a stress field that is responsible for a normal faulting regime, implying a compressive $\sigma_{HMAX}=\sigma_2$ and an extensional $\sigma_{HMIN}=\sigma_3$. σ_1 is then equal to σ_V (Fig. 4.4a, b). For T_S and T_d calculations, we have assumed for models reasonable values of 100 Pa and 50 Pa for σ_{HMAX} and σ_{HMIN}, respectively.
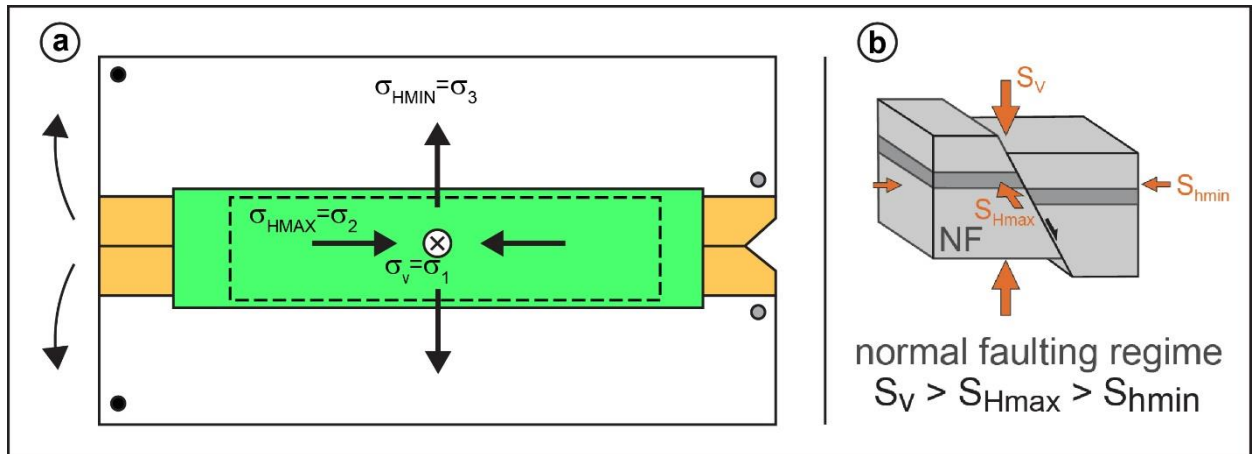
Figure 4.4. (a) Stress field induced on a model by our deformation apparatus, coherent with an extensional stress field (b). Sketch in (b) is modified from the World Stress Map by Heidbach et al., (2016).

We have elaborated top view of model surface with fault traces coloured by the value of T_d and T_s. Figure 4.5a shows the fault traces map for Model RP-4, coloured by T_S. Figure 4.5b shows the rose diagram of fault segments coloured by the same parameters. Warm colours indicate high (normalized) tendency to slip. Clearly, the reactivated faults are favourably oriented to the stress field. This is simply testified by the fact that they were reactivated during deformation. For example, discontinuities of set S1 were not reactivated because they are not favourably oriented. Nonetheless, among this simple consideration, values of T_S indicate that, although favourably oriented, S2 were not reactivated as dilation structures but experienced

91

slip. Besides, rift-related faults did not experience slip and were highly dilatant. This is also evident from Figure 4.5c and Figure 4.5d, showing the fault trace map and rose diagram of fault segments orientation for the same model RP-4 coloured by T_d. In this case, reactivated faults were marked by purple colours, indicating scarce tendency to dilation. This is an obvious direct effect of discontinuity orientation.
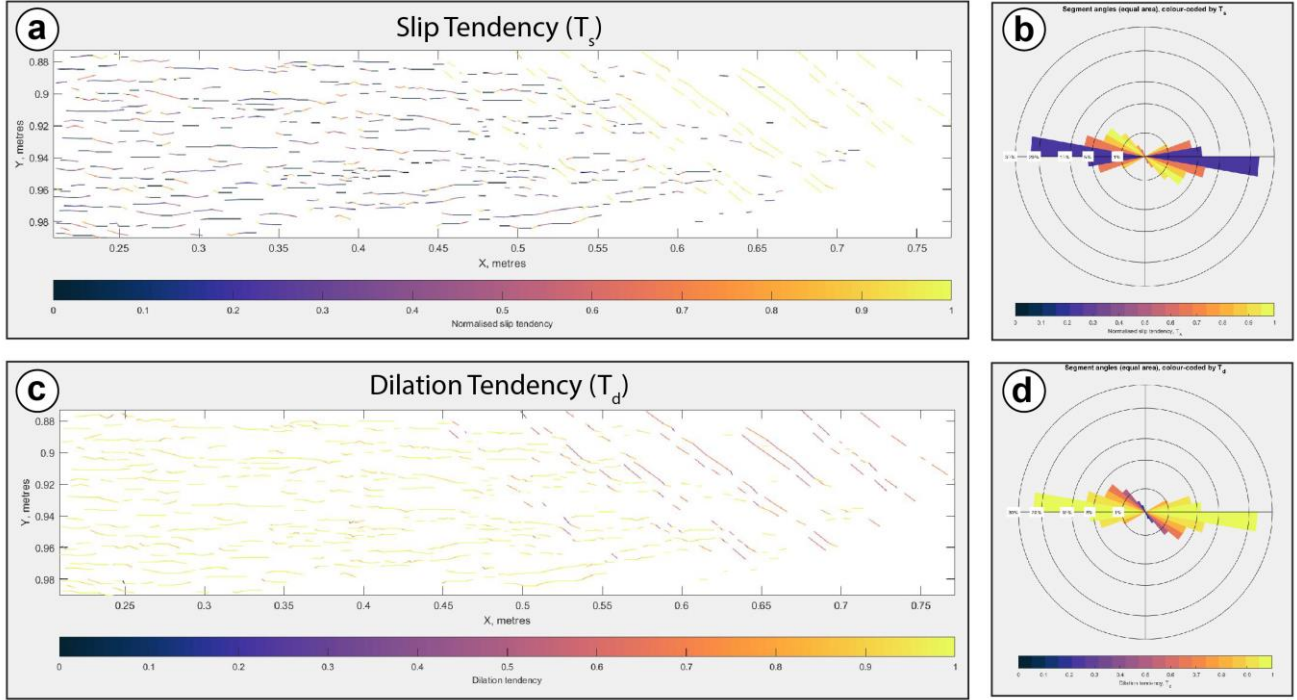
Figure 4.5. Slip tendency and Dilation tendency of structures in Model RP-4. (a) Mapped fault traces coloured according to calculated Normalized Slip tendency (T_s). Cooler colours indicate lower T_s while warmer colour marks higher T_s. (b) Rose diagram showing trend of mapped fault traces coloured by T_s. Colour scale is the same as in (a). (c) Mapped fault traces coloured according to calculated Dilation tendency (T_d). Cooler colours indicate lower Td while warmer colour marks higher T_d. (d) Rose diagram showing trend of mapped fault traces coloured by T_d. Colour scale is the same as in (c).

Model RP-8 was analysed similarly to Model RP-4, calculating T_S and T_d. Figure 4.6a shows the fault pattern for this model, coloured by Ts, indicating that rift-related structures have a scarce tendency to slip. Besides, discontinuities belonging to S1 and S2 are more favourably oriented to be reactivated as slipping structures. Rift-related felts show high tendency to dilation (T_d), as expected, but in this case also discontinuity S1 and S2 have an orientation that implies high values of T_d, and grabens formed by the reactivation of these structures are consistently rather continuous and wide (Fig. 4.6c, d).
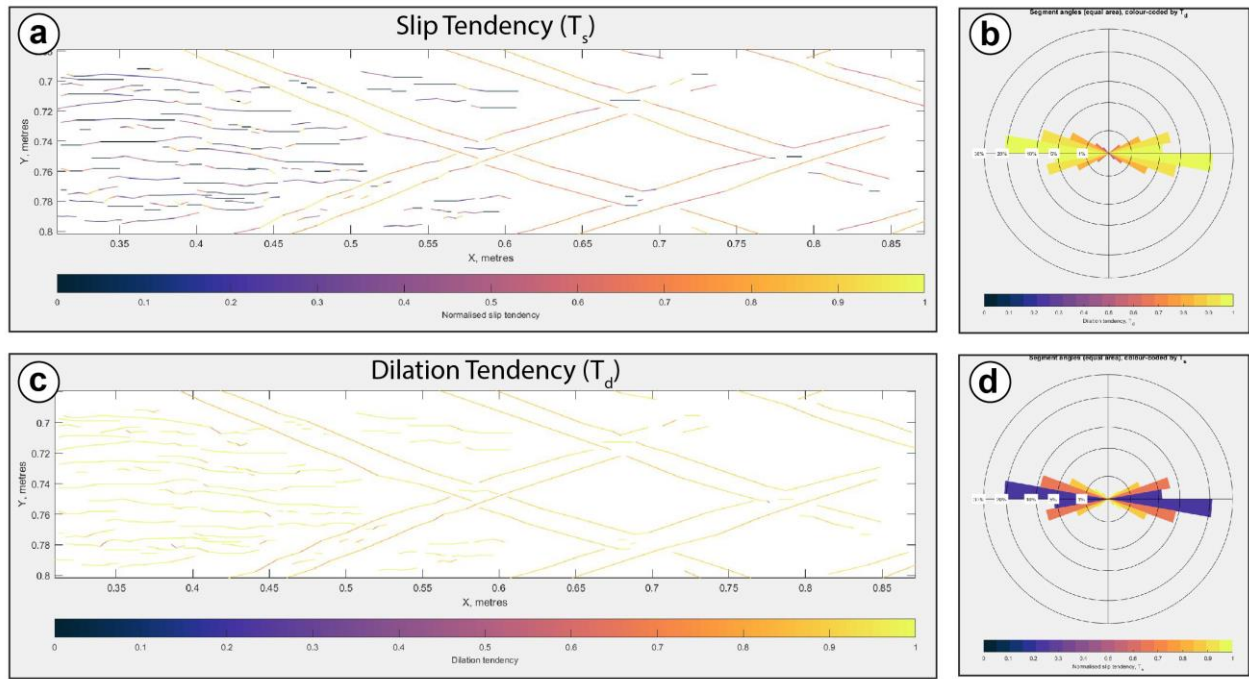
Figure 4.6. Slip tendency and Dilation tendency of structures in Model RP-8. (a) Mapped fault traces coloured according to calculated Normalized Slip tendency (T_s). Cooler colours indicate lower T_s. Warmer colour marks higher T_s. (b) Rose diagram showing trend of mapped fault traces coloured by T_s. Colour scale is the same as in (a). (c) Mapped fault traces coloured according to calculated Dilation tendency (T_d). Cooler colours indicate lower Td while warmer colour marks higher T_d. (d) Rose diagram showing trend of mapped fault traces coloured by T_d. Colour scale is the same as in (c).

4.2 Addressing the influence of pre-existing discontinuities in caldera collapse

We have systematically tested the role of variously-oriented discontinuities (from the substrate to the brittle overburden) in caldera collapse processes through models performed in the four sub-series of Series D3.5-2. Sub-series D3.5-2a gives a reference model for comparison of all other models, hence it is useful to start the discussion from Model-17.

Modelling results of circular caldera collapse (Model-17) represent the formation of a typical fault pattern: outward-dipping reverse faults developed since the incipient stage of modelling, after initial down-sagging, to progressively reduce displacement (i.e., accommodating less deformation) due to deformation shift in peripheral areas, where inward-dipping normal faults start to develop. This fault system represents the outer rim of ring faults of the collapsed caldera. Model evolution obtained from our model setup is therefore similar to what proposed by Acocella (2007). When comparing temporal evolution of Model-17 with the model proposed by Acocella (2007; Figs. 4.7 and 4.8), we can define the observed 4 stages: the incipient down-sagging (stage 1) is followed by reverse faulting (stage 2) and shift of deformation (peripheral down-sagging (stage 3) to generate outer normal ring faults (stage 4) and terminate the collapse process. Interestingly, this evolution has been observed for various models using setups applying an under-pressure

mechanism (Acocella, 2007) and our models, which use a similar setup proposed by Roche (2000), are similar. This is a guarantee of model reproducibility and therefore of model quality. Soundness of Model-17 therefore represents an important step to correctly interpret models performed for other experimental sub-series.
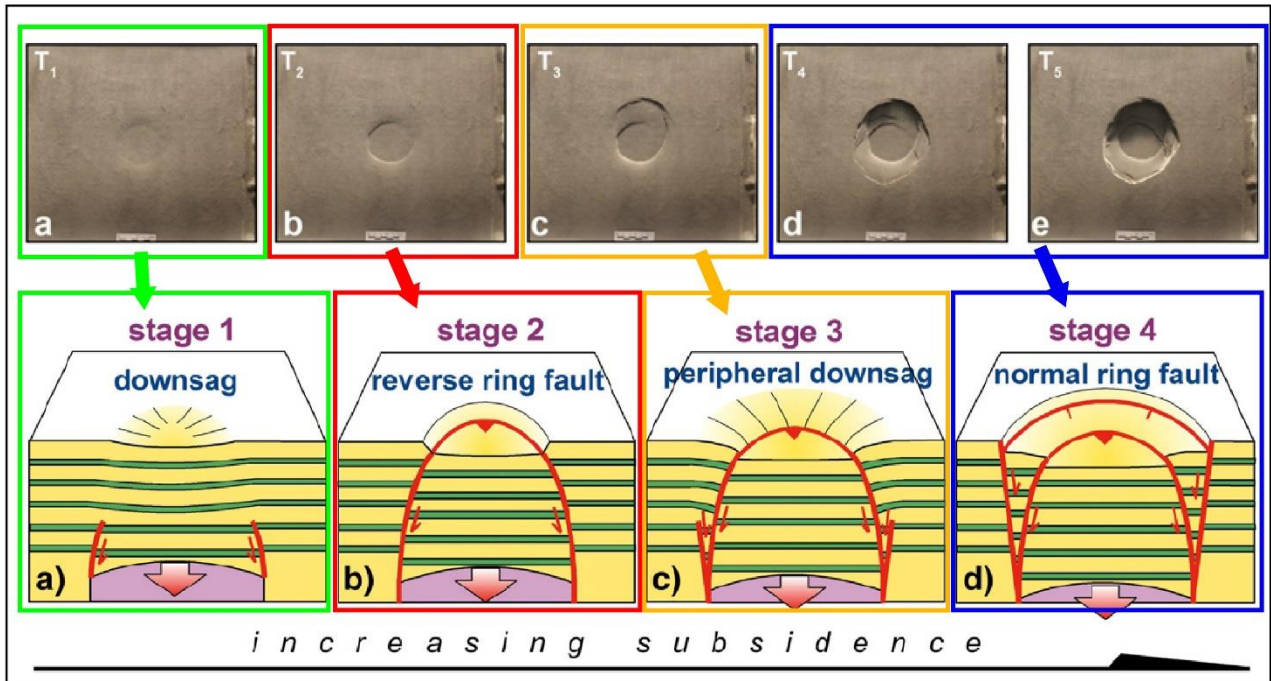
Figure 4.7. Model-17 progressive deformation throughout time, compared to caldera collapse evolution proposed by Acocella (2007), which is reported in the lower panels. In particular, evolution of Model-17 occurs according to a similar 4-stage model, from incipient down-sagging caldera collapse generating inner outward-dipping reverse faults to external shifting of deformation accommodated by peripheral down-sagging, normal faults forming the external ring fault system.
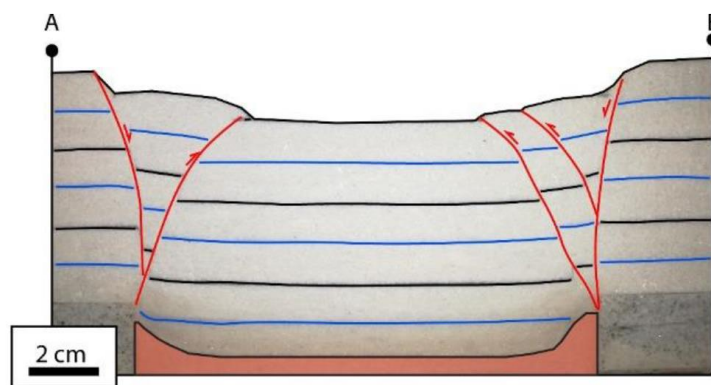
Figure 4.8. Section AB of Model-17 (see Fig. 3.13 for section location). Note similarity with the sketch in Fig. 4.7.

Besides this first-order similarity, there are relevant aspects related to lateral fault propagation and fault interference (both regarding the reverse and normal ring fault systems) that have been identified from the use

of the Qz-Kfeldspar sand mixture (which allows high resolution of fault detection). This evolution is notable in this model, but was previously barely described. This aspect, indeed, is important for a correct understanding of caldera collapse processes, yet it does not properly belong to the topics addressed by Deliverable 3.5, which mostly discuss considerations on the role of tectonics. For this reason, these aspects are discussed more extensively in Deliverable 3.6 (*Report on the analogue modelling of the collapse of caldera and volcanic edifices and the associated surface deformation*), which focuses on caldera collapse processes. In the present Deliverable 3.5, we have limited the discussion of Model-17 to define the first-order structural pattern that developed as described above, and that is of interest for comparing differences induced by the presence of inherited structures simulated in the Series D3.5-2 models.

Model of sub-series D3.5-2b aimed at the investigation of inherited discontinuities that do not affect the magma chamber (i.e., are placed above it in the brittle overburden or aside to it). Interestingly, Model-20 contains an internal discontinuity and differs for some aspects from the standard evolutionary model described above. In particular, this model differs significantly in that the reactivation of the near tangent structure "attracts" the propagating reverse fault and stops it. The reverse fault does not crosscut the reactivated structure, the latter linking to the incipient normal ring fault. Due to the circularity of the analogue magma chamber, the normal fault continued its propagation along a circular trajectory, leading to a geometry similar to that of Model-17, except for the well-developed reactivated, rectilinear intra-caldera fault.

The tangent discontinuity introduced in Model-21 led to a geometry similar to that observed in Model-21, but did not "attract" reverse faults, the discontinuity being located in a more external position. These models suggest that the effect of a near-tangent and tangent discontinuity in the brittle overburden above the analogue magma chamber is to generate (due to reactivation during caldera collapse) a rectilinear, nearly vertical intra-caldera normal fault that links to the external system of ring faults.

According to what described, one would expect that a central discontinuity may have a significant effect on the caldera collapse process. Nonetheless, Model-22 demonstrates that role of a central discontinuity located above the analogue magma chamber is unimportant. Furthermore, high resolution DEM of the caldera centre shows that no displacement is observed in the central subsided piston at the location of the existing discontinuity (Fig. 4.9).
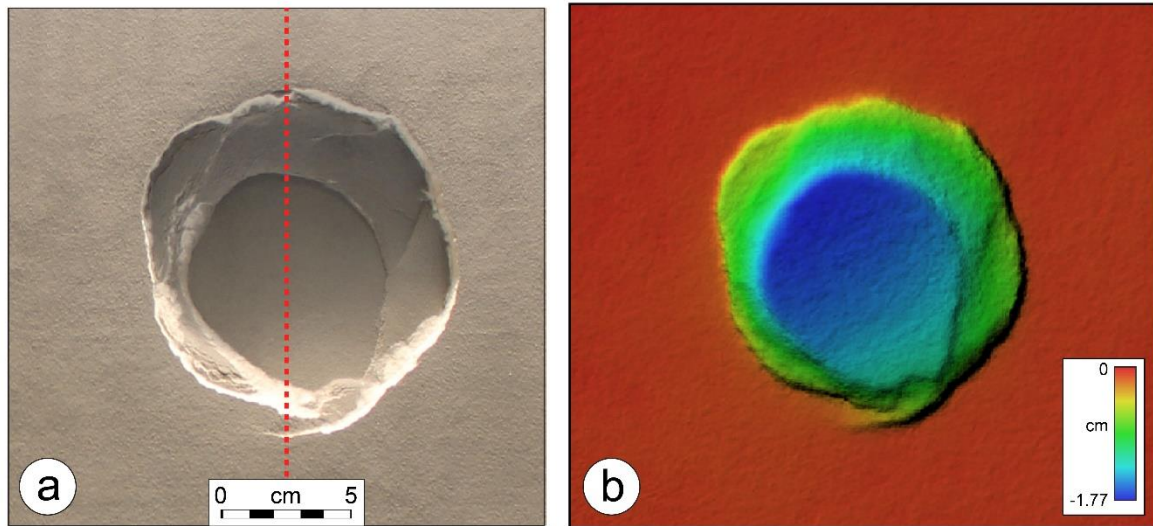
Figure 4.9. Top-view (a) and DEM (b) for Model-22. An artificial rectilinear discontinuity was introduced in the sand pack above the analogue magma chamber, in the centre of the model. DEM shows no evidence for reactivation of this discontinuity after caldera collapse.

Regarding the presence of an external discontinuity, as expected the latter had no effect on caldera collapse processes, as shown by Model-23.

Models of Series D3.5-2c aimed to test the possible role of inherited discontinuities affecting the analogue magma chamber and limiting its geometry (i.e., bounding the analogue magma chamber, hence having one or more rectilinear sides). In these models, we shaped the analogue magma chamber with one or two rectilinear sides (vertical side or 60°-dipping inward/outward side) to simulate a fault limited to the substrate and not extending in the brittle overburden.

Analysis of temporal deformation pattern of Model-24 and Model-30 indicate that the presence of one or two vertical discontinuities in the substrate does not alter the chronology of deformation defined with the standard circular Model-17: both models experienced the typical four-stage evolution (down-sagging, reverse faulting, peripheral-down-sagging and normal ring faulting). Nonetheless, these models showed that the presence of a discontinuity limiting the analogue magma chamber strongly affects the final geometry of the collapsed caldera, which will be defined by rectilinear reverse and normal faults in correspondence of the introduced discontinuities; this evolution also indicates that the boundary of the analogue magma chamber is a sensitive area that has the ability to influence the final caldera geometry (Fig. 4.10).
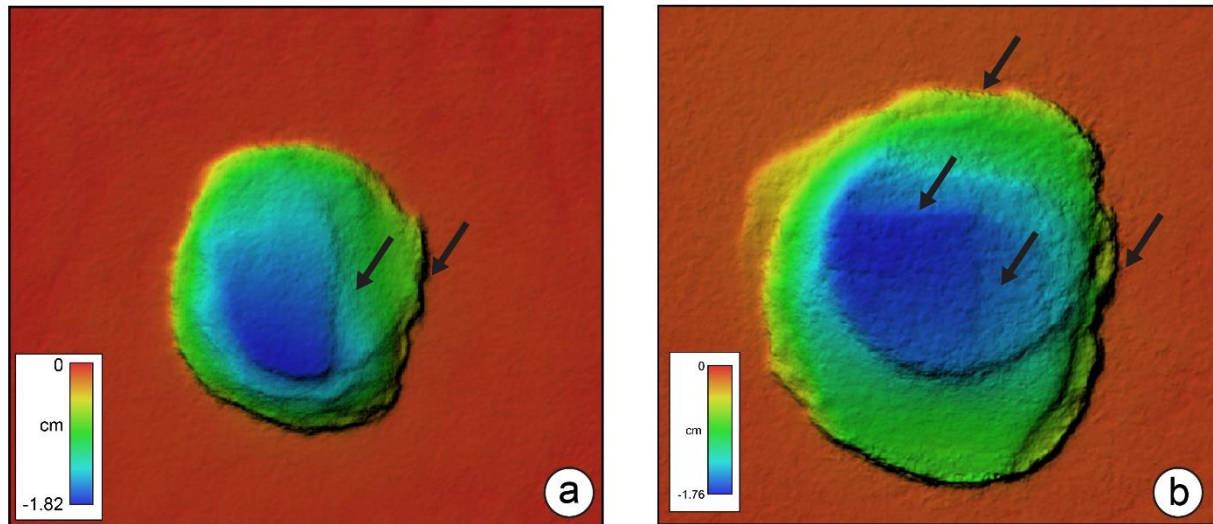
Figure 4.10. Digital Elevation Model of (a) Model-24 bearing one artificial rectilinear discontinuity limiting the analogue magma chamber and (b) Model-30, designed with two rectilinear discontinuities bounding the analogue magma chamber. Both DEMs of final models show that the introduced discontinuities strongly affected the final geometry of the collapsed caldera. Black arrows indicate the rectilinear caldera faults.

A similar effect was observed when introducing 60°-dipping rectilinear faults at one side of the analogue magma chamber (i.e., Model-36, Model-37 and Model-39, the latter having the same inherited structure as Model-37 but in a more internal position). In detail, the 60°-dipping inward and outward faults forced the collapsing caldera to develop rectilinear reverse and normal faults. Comparing these models with Model-24 and Model-30, one can note a higher degree of complexity inside the subsided caldera, which is likely related to the minor accommodation volume linked to the non-vertical inherited faults. The 60°-dipping fault likely caused internal block reorganization that led to the formation of secondary structures connecting circular reverse/normal structures and rectilinear structures (Fig. 4.11). Nonetheless, the first-order effect of the introduced artificial discontinuity was similar to what described earlier.
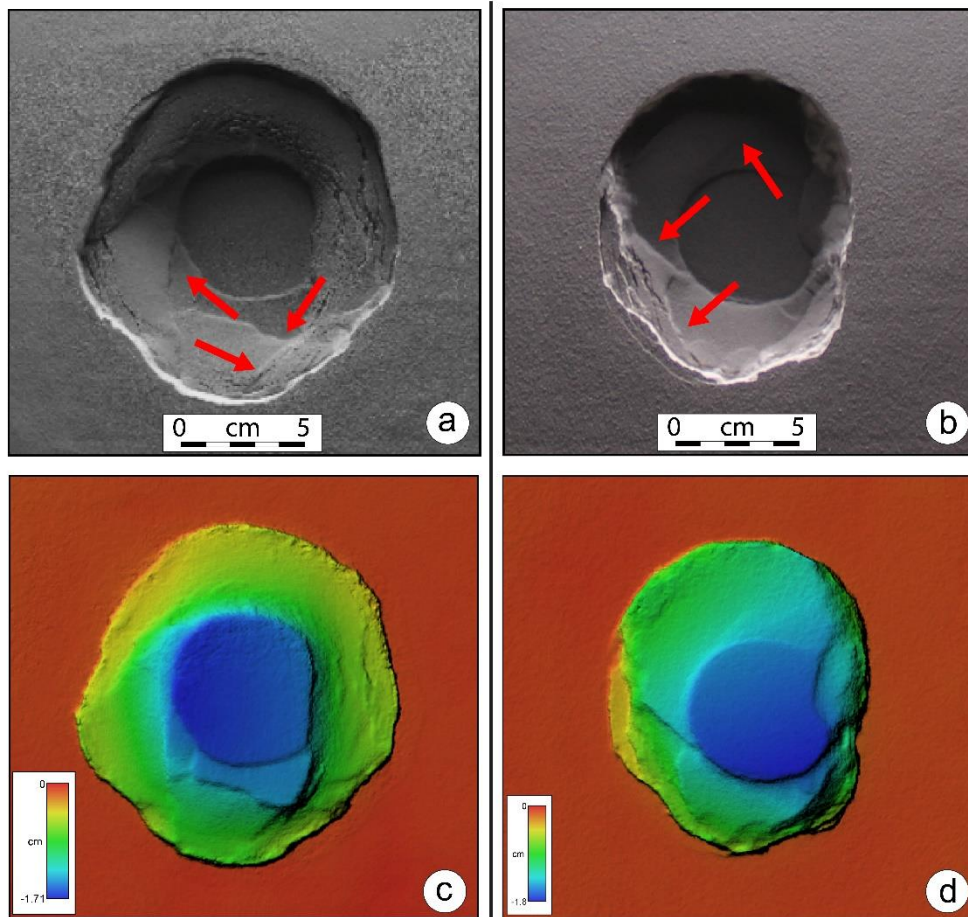
Figure 4.11. (a, b) Top views of Model-36 and Model-37, and (c, d) Digital Elevation Models (DEMs). Red arrows indicate secondary structures developed during caldera collapse that were likely derived by volume accommodation related to the presence of non-vertical inherited faults in the substrate. Besides this second-order difference compared to Model-24 and Model-30, these two models show the same first-order structural pattern, with rectilinear faults forced by the presence of artificial discontinuities delimiting the analogue magma chamber.

Rather different is instead the case of some models belonging to sub-series D3.5-2d. Models of this sub-series aimed to test the role of fault discontinuities in the substrate (and limiting the analogue magma chamber) and affecting in continuation the overlying brittle overburden. Furthermore, Model-76 tested the specific case of discontinuities developing in the substrate and brittle overburden, but not affecting the latter in its whole thickness; the vertical discontinuities stopped at 2 cm below the model surface, simulating inherited structures that may have been sealed by volcanic deposits.

Model-25 and Model-32 differ substantially from the model of the other sub-series, in that both the final geometry and chronology of fault pattern development showed several variations. On areas of the model where no discontinuities were introduced, the two models developed without showing appreciable differences in comparison to Model-24 and Model-30. The central caldera piston subsided accommodating the displacement along outward-dipping reverse faults and afterwards along inward-dipping normal faults.

Contrarily, in areas bearing the introduced artificial discontinuities, the deformation followed a different evolution. Specifically, the vertical discontinuities localized deformation, and totally reactivated the entire brittle overburden, inhibiting the formation of outward-dipping reverse faults (Figs. 4.12 and 4.13).
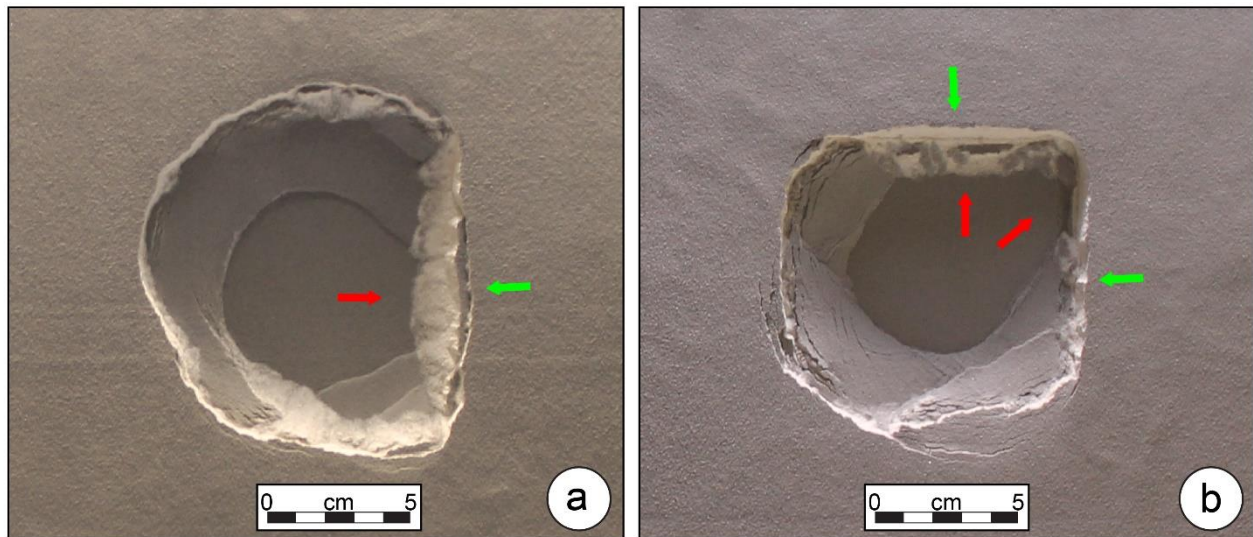
Figure 4.12. (a) Top-view of Model-25 showing the reactivated, rectilinear discontinuities (green arrow) and the missing reverse fault at the caldera centre (red arrow). Reverse fault formation was likely inhibited by the total reactivation of the discontinuities. (b) Top-view of Model-32 showing, as for Model-25, the reactivated discontinuities (green arrows) and the missing internal reverse faults (red arrows).
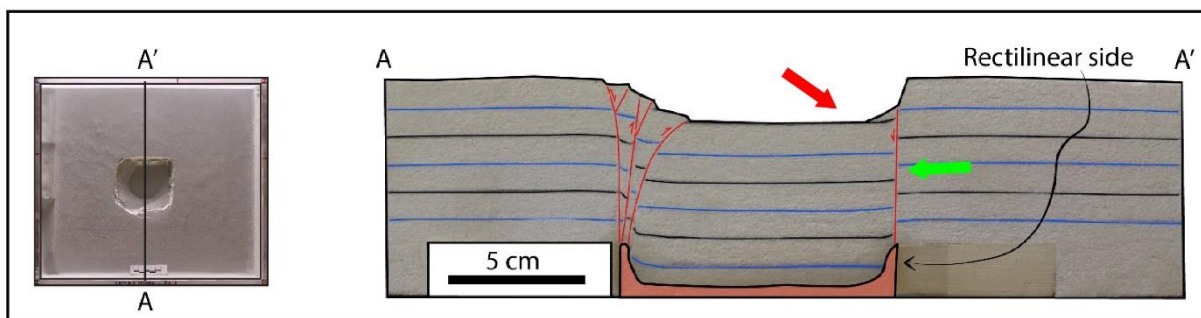
Figure 4.13. Cross section of Model-32 showing the presence of a rectilinear sub-vertical normal fault (green arrow) and the missing of the central reverse fault (red arrow), which is instead present on the opposite side, where no discontinuities have been introduced.

This led the models to develop rectilinear sides in correspondence of the introduced discontinuities, but different intra-caldera geometries. This model evolution seems to not apply to Model-35, Model-38 and

Model-40 built with fault discontinuities dipping 60° inward or outward, as these models followed the classical evolution with reverse faults and normal faults developing all along the subsiding caldera piston.

Finally, a specific case is represented by Model-76. If the other models represented systematic variations to define experimental series, Model-76 aimed to test specific aspects of interest for Los Humeros caldera system, which emerged after discussion with other work-packages (especially WP4; Liotta and WP4 Working Group, 2019). We tested the idea of two inherited faults driving the formation of rectilinear ring faults at the caldera border (as in Model-25 and Model-32), but not affecting the entire overburden sequence, as volcanic deposits overlay the Los Humeros caldera area. Furthermore, a third structure was hypothesized to crosscut the centre of the caldera systems, as in Model-22 (but not reaching model surface). Model-76 shows intermediate features compared to the above described models. In particular, the external discontinuities led to the formation of rectilinear ring faults, but the depth of the upper fault tip (2 cm in the model) likely played an important influence on inhibiting or not the formation of rectilinear reverse fault at the caldera centre. Whereas in Model-25 and Model-32 the presence of the inherited faults completely inhibits the formation of reverse faults, in Model-76 this did not completely happen, the reverse fault being absent only on one of the two sides bearing the discontinuity. This effect is likely due to the termination depth of the discontinuity, which did not reactivate completely. Notable is in fact the variation of normal fault angle in the upper 2 cm of the model (Fig. 4.14a). Whereas in Model-25 and Model-32 the normal fault reactivated completely with a sub-vertical attitude, in Model-76 the dip angle of one of the two rectilinear normal faults decreased to a lower value. Interestingly, as for Model-22, no evidence for the reactivation of the central discontinuity is observed (Fig. 4.14a, b).
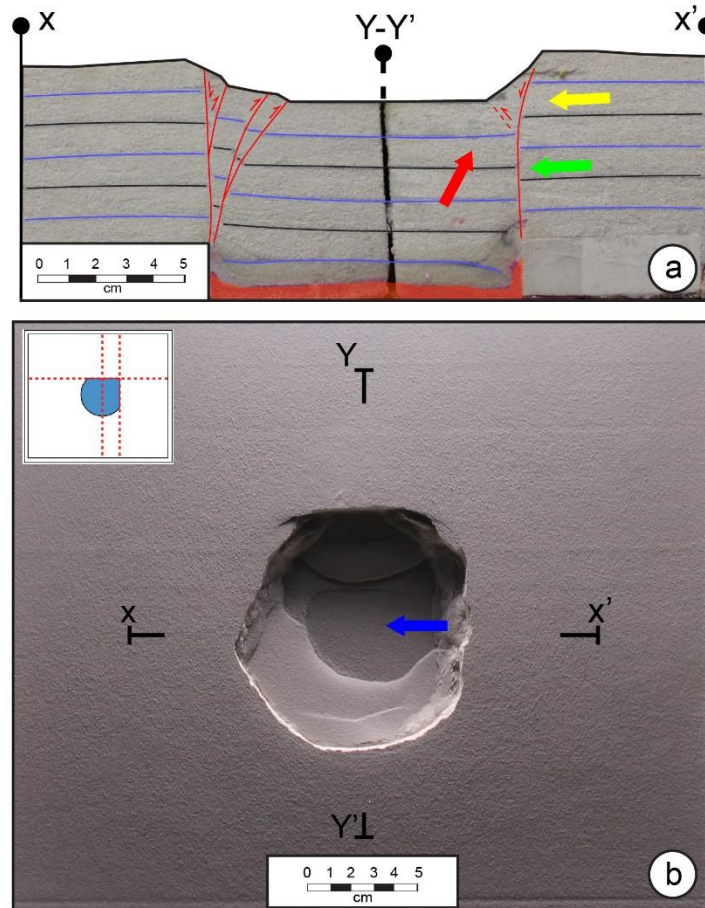
Figure 4.14. (a) Cross section of Model-76 showing the reactivated, rectilinear fault discontinuity (green arrow) decreasing its dip angle at surface (yellow arrow) and the missing principal reverse fault (red arrow). (b) Top-view of Model-76 showing the non-reactivation of the central discontinuity. Blue arrow indicates the position where the discontinuity was placed before model deformation.

4.3 Clues from analogue modelling of Series D3.5-1 and D3.5-2 on the evolution of Los Humeros and Acoculco geothermal systems

In sections 4.1 and 4.2 we have discussed specific aspects of models performed in experimental series D.3.5-1 and D3.5-2, aiming at the investigation of (1) possible interactions between a propagating rift and inherited crustal faults and (2) the role of pre-existing discontinuities on caldera collapse processes. In this section 4.3 we discuss more specifically how the results of these models can be applied to the case study of Los Humeros volcanic complex and Acoculco caldera complex. Regarding series D3.5-1, interestingly is to discern whether inherited fault systems identified by other authors and WP in the area of interest may have reacted to stress induced by rift propagation. Specifically, our models showed that not all the inherited fault systems are likely to be reactivated during rift propagation. Sketch in Figure. 4.2 indicates that for a

101

symmetric rift opening, discontinuity sets that are favourably oriented for reactivation are comprised between N45° and N135°, considering a direction of rift propagation trending N90°. This is important when trying to asses which of the existing faults have a potential for focusing migration of magmatic fluids, under the assumption that an active (or reactivated) fault could better convey magmatic fluids toward the surface than an inactive and sealed fault. Considering the case of Los Humeros and Acoculco, Model RP-4 simulated the structural case of two discontinuity sets S1 and S2, trending respectively N30° and N125° in the model reference frame. These orientations, considering assumptions and corrections made in our model (see section 2.2.1) correspond to a real orientation of N°45 and N145°. Evolution of model RP-4 showed that only discontinuity set S2 trending N125° (i.e., N145° in the natural case) is favourably oriented to be reactivated by a propagating rift, while the N30°-trending set S1 (i.e., N45° in the natural case) remained inactive. This may suggest that inherited discontinuities that are likely to localize magmatic fluid migration at Los Humeros and Acoculco might be those trending (on average) N145°. Interestingly, discontinuity set S2 was highly reactivated during deformation of Model RP-4, and showed a certain dilation tendency indicating an even more favourable condition for the upward migration of magmatic fluid. Normalized values of dilation tendency of reactivated structures in Model RP-4 is generally higher than 0.5 (normalized values vary between 0 and 1, being 1 the dilatation value of pure extensional structures; yellow colour in Fig. 4.15). This is most evident where reactivated S2 structures link with rift-related propagating faults, generating hybrid faults (black arrows in Fig. 4.15) trending, for short distances, with an angle comprised between N125° (i.e., S2 trend in the models) and N90° (i.e., direction of rift propagation and trend of extensional rift-related propagating faults) (Fig. 4.15). Notably, this evolution accords well with the observation that ca. N145°-trending faults show the highest geothermal alteration produced by emplacement of geothermal fluids (see section 1.3). The preferential movement of magmatic fluids along NW-SE-oriented faults may thus suggest a partial reactivation of these inherited structures, which may accord with the results of the analogue modelling.
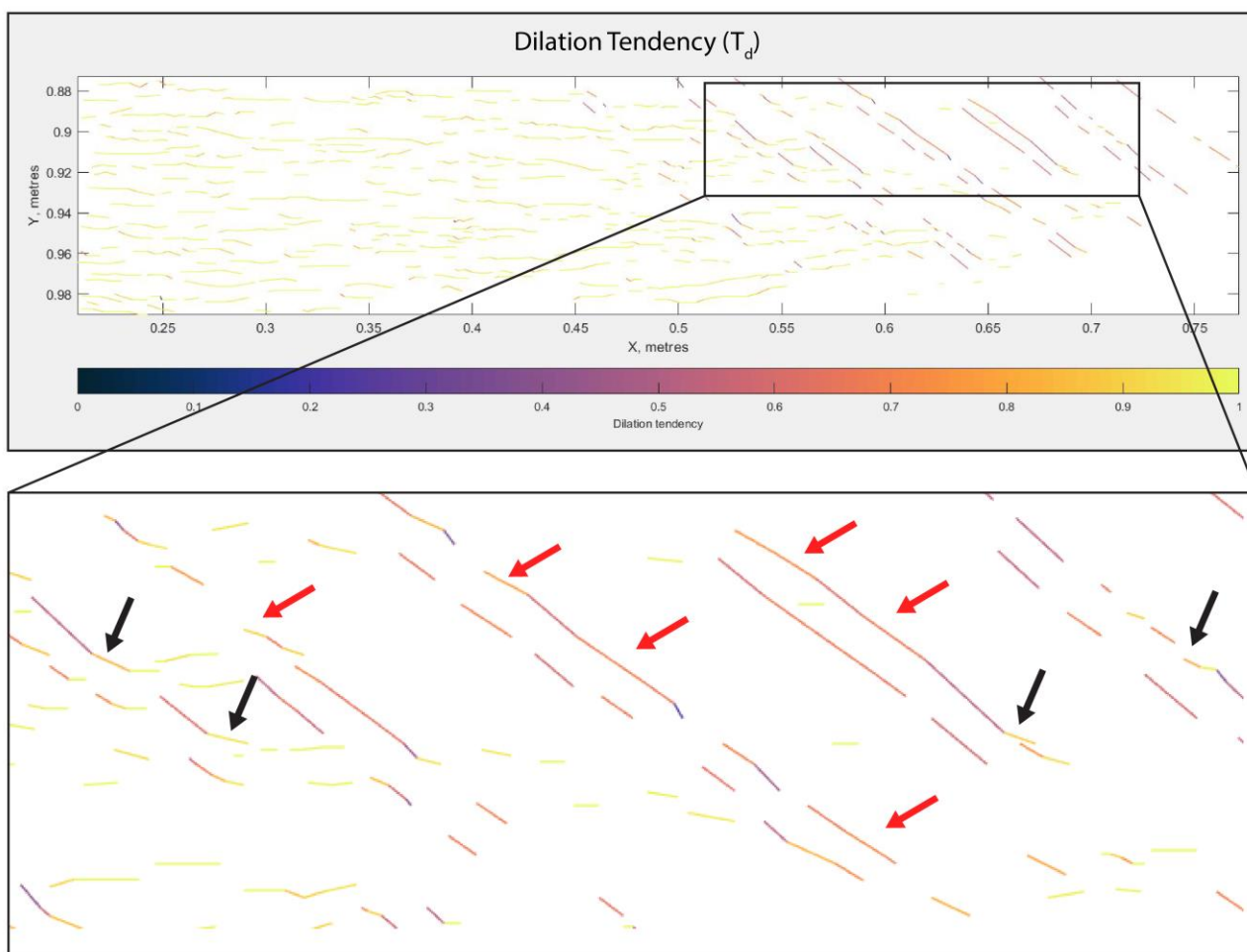
Figure 4.15. **Normalized dilation tendency for Model RP-4. Reactivated set S2 structures show a considerable degree of dilatation, suggesting potentially favourable conditions for fluid migration.**

Therefore, locations where the intersection between reactivated structures and rift-related propagating faults is evident in nature might represent favourable loci for fluid migration that deserve further investigation.

Whereas these models investigated the possible role of tectonics on fluid migration at a regional scale, series D3.5-2b tested the influence of inherited tectonic structures on caldera collapse processes, therefore giving insights into the possible relationships between structures and geothermal fluids at a local scale.

The aim of the four subseries (D3.5-2a, D3.5-2b, D3.5-2c, and D3.5-2d) was to test different combinations of inherited faults showing different attitude (orientation, dip, portion of the stratigraphy affected by artificial discontinuities). Beyond specific results discussed in section 4.2, the performed models, when compared to the natural cases of Los Humeros and Acoculco, indicate a significant degree of similarity.

In particular, Model-25 and Model-32 (bearing respectively one and two discontinuities developing from the substrate to the model surface) resulted in a geometry that is strikingly comparable to what described by

103

various authors and by the work carried out in the frame of WP4 (Liotta and WP4 Working Group, 2019). As regards Los Humeros, several studies (e.g., Carrasco-Núñez et al., 2017b; 2018; Norini et al., 2019) suggest that the shape of the collapsed caldera may have been controlled by pre-existing faults that have been reactivated during its collapse. This would have led to the formation of the rectilinear south-eastern caldera rim (i.e., the 'Los Humeros scarp'), and likely to that of a similar feature delimiting the south-western caldera rim (see section 1.2). Model-25 and Model 32 indicate that a discontinuity in such a position may result in a similar geometry, once reactivated during caldera collapse (Fig. 4.16). Similarly, geological and structural data at the Acoculco caldera complex (e.g., López-Hernández al., 2009; Avellán et al., 2018) report the occurrence of inherited faults in correspondence of some segments of the caldera rims that achieve a sub-rectilinear geometry (Fig. 4.16)
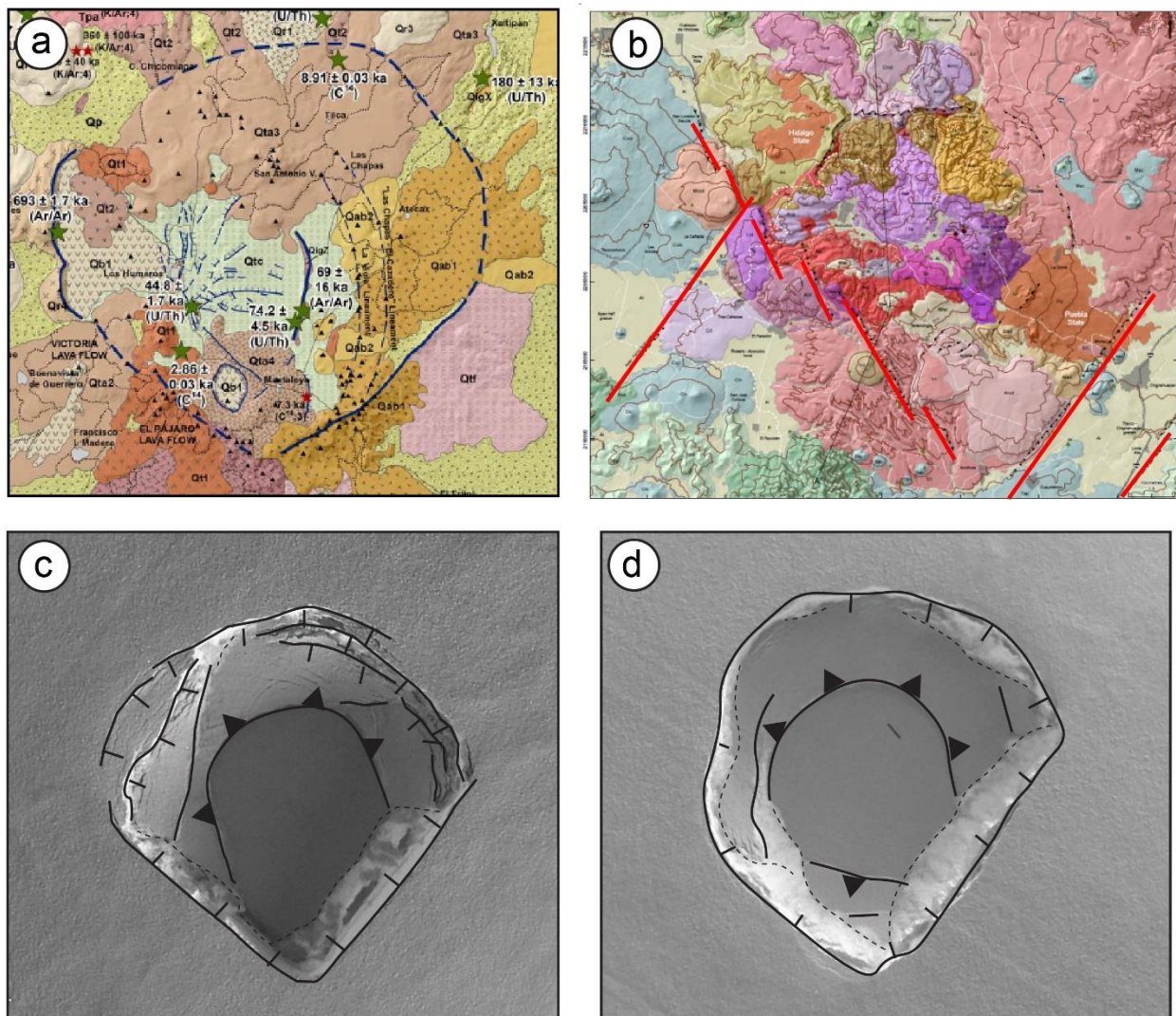
Figure 4.16. (a) Structural and geological maps of the Los Humeros volcanic complex (from Carrasco-Núñez et al., 2018) and (b) Acoculco caldera complex (modified from Avellán et al., 2018) showing the presence of rectilinear faults bounding the caldera systems. (c) and (d) Comparison in the surface fault pattern with Model-32 and Model-25, which show marked similarity with the natural prototype.

These models were designed with artificial discontinuities extending from the substrate to include the overburden up to the surface of the model. Likely, at Los Humeros and Acoculco, inherited faults were sealed by volcanic deposits, reflecting a model setup more similar to Model-76. In this model, the introduced discontinuities only partly affected the overburden, not reaching the model surface (but stop at a depth of 2 cm below model surface). Nonetheless, Model-76 resulted in a shape similar to Model-25 and Model-32 and therefore to the natural prototype of Los Humeros and Acoculco. This observation supports that inherited structures bordering a magma chamber (affecting the overburden, or only part of it) have the ability to be reactivated during caldera collapse, leading to the formation of rectilinear caldera rims. In general, however, the deformation pattern of Los Humeros and Acoculco calderas show a broad similarity with that of analogue models controlled by pre-existing discontinuities (Fig. 4.16), a correspondence suggesting that model and natural prototypes may share a similar evolution.

Model-76 also tested the possible influence of a central discontinuity localized above the analogue magma chamber and stopping 2 cm below model surface. We tested the presence of such a structure also in Model-20, but in this case the discontinuity affected the entire overburden sequence. In both Model-20 and Model-76 the central discontinuity was not reactivated, suggesting that a symmetric piston-like caldera subsidence is not able to reactivate inherited structures located in a central position above the magma chamber. Therefore, our models may indicate that the origin of the internal faults at Los Humeros could be related to a process different from simple symmetric caldera collapse.

Finally, the variations in model setup applied to sub-series D3.5-2b, D3.5-2c and D3.5-2d, regarding the localization of the tested inherited structures (i.e., affecting the substrate or the overburden, or both) suggest that seemingly there are variations in the general model of caldera collapse development proposed by many authors and summarized by Acocella (2007; Fig. 2.3). Some key structural elements may be missing during caldera development as for instance observed in Model-25 and Model-32, where the development of segments of reverse faults was inhibited due to the reactivation of inherited structures. This also suggests care in interpreting the internal architecture of caldera systems characterised by the presence of inherited faults (such as the Los Humeros volcanic complex), since not all the expected structures may be present (and brittle structures are important targets for geothermal exploration). Besides, not all the observed structures may be related to the caldera collapse process, at least when occurring symmetrically. Different is the case of asymmetric caldera collapse (e.g., trapdoor systems), which is one of the targets addressed by Deliverable 3.6.

5 Conclusion

Deliverable 3.5 reports the results obtained in the frame of Task 3.3, testing the interactions between regional tectonics and volcanic systems by developing new analogue models. In this frame, we have implemented two experimental series (D3.5-1 and D3.5-2) aiming respectively at the investigation of (1) the effect of a propagating rift on inherited fault reactivation, and (2) testing the possible role of inherited faults on caldera collapse processes.

By presenting and discussing 9 models (out of a total of 26 models) for Series D3.5-1, we have shown that a propagating rift (i.e., extension along the TMVB induced by propagating slab tearing) is able to interact with inherited faults, by reactivating those that are favourably oriented to the stress field induced by the rifting-related stresses. Among various orientations, models revealed that considering a propagating rift trending N90° only inherited faults striking between N45° and N135° were reactivated, also suggesting that these are the most favourable for conveying migration of magmatic fluids. The specific setup of Model RP-4 showed that in the natural case of the TMVB (specifically in the areas of Los Humeros volcanic system and Acoculco caldera system), only inherited faults trending N145° (i.e., N135° in the model) are favourably oriented for reactivation. Analysis of dilation tendency suggests that reactivated structures bear a dilation component that is likely facilitating magmatic fluid migration. Interestingly, dilation tendency increases in the fault segments linking the reactivated structures with the rift-related propagating faults (trending between N90° and N125°).

The 16 models presented for series D3.5-2 (out of a total of 18) showed how inherited structures may interact with the caldera collapse process, leading to variations in the 'classical' caldera collapse evolutionary model envisaging the formation of outward-dipping reverse faults followed by inward-dipping normal faults. Model development showed that rectilinear discontinuities bounding an analogue magma chamber m ay lead to the formation of rectilinear reverse faults and normal faults at surface, not changing the chronology of the fault pattern development, but affecting its geometry. Inherited faults not bounding magma chamber but affecting the overburden are instead able to force the formation of intra-caldera rectilinear faults. Besides, inherited structures bounding an analogue magma chamber and affecting the overburden stratigraphy (entirely or only part of it) are able to generate rectilinear caldera ring faults, sometimes inhibiting the formation of the inner reverse fault system. Interestingly, some models of Series D3.5-2 showed a high degree of similarity with the structural setting of the Los Humeros volcanic system and Acoculco caldera system, supporting the potential presence of inherited, rectilinear regional faults that might have been reactivated during caldera collapse to form part of the caldera ring fault system. Finally, models testing the presence of a central discontinuity suggest no reactivation of such structures during symmetric caldera collapse.

6 References

Acocella, V. (2007). Understanding caldera structure and development: An overview of analogue models compared to natural calderas. Earth-Science Reviews, 85(3-4), 125-160.

Acocella, V., & Mulugeta, G. (2002). Experiments simulating surface deformation induced by pluton emplacement. Tectonophysics, 352(3-4), 275-293.

Acocella, V., Faccenna, C., Funiciello, R., & Rossetti, F. (1999). Sand-box modelling of basement-controlled transfer zones in extensional domains. Terra Nova-Oxford, 11(4), 149-156.

Acocella, V., Cifelli, F., & Funiciello, R. (2000). Analogue models of collapse calderas and resurgent domes. Journal of Volcanology and Geothermal Research, 104(1-4), 81-96.

Acocella, V., Cifelli, F., & Funiciello, R. (2001a). Formation of nonintersecting nested calderas: insights from analogue models. Terra Nova, 13(1), 58-63.

Acocella, V., Cifelli, F., & Funiciello, R. (2001b). The control of overburden thickness on resurgent domes: insights from analogue models. Journal of Volcanology and Geothermal Research, 111(1-4), 137-153.

Acocella, V., Funiciello, R., Marotta, E., Orsi, G., & De Vita, S. (2004). The role of extensional structures on experimental calderas and resurgence. Journal of Volcanology and Geothermal Research, 129(1-3), 199-217.

Agostini, A., Corti, G., Zeoli, A., & Mulugeta, G. (2009). Evolution, pattern, and partitioning of deformation during oblique continental rifting: Inferences from lithospheric-scale centrifuge models. Geochemistry, Geophysics, Geosystems, 10(11).

Autin, J., Bellahsen, N., Husson, L., Beslier, M.O., Leroy, S., d'Acremont, E. (2010). Analogue models of oblique rifting in a cold lithosphere. Tectonics, 29, TC6016, doi:10.1029/2010TC002671.

Autin, J., Bellahsen, N., Leroy, S., Husson, L., Beslier, M. O., & d'Acremont, E. (2013). The role of structural inheritance in oblique rifting: Insights from analogue models and application to the Gulf of Aden. Tectonophysics, 607, 51-64.

Avellán, D.L., Macías, J.L., Layer,P.W., Cisneros, G., Sánchez-Núñez, J.M., Gómez-Vasconcelos, M.G., Pola, A., Sosa-Ceballos, G., García-Tenorio, F., Reyes Agustín, G., Osorio-Ocampo, S., García-Sánchez, L., Mendiola, I.F., Marti, J., López-Loera H., Benowitz, J. (2018). Geology of the late Pliocene – Pleistocene Acoculco caldera complex, eastern Trans-Mexican Volcanic Belt (México). Journal of Maps, DOI: 10.1080/17445647.2018.1531075Bellahsen, N., Daniel, J.M. (2005). Fault reactivation control on normal fault growth: an experimental study. J. Struct. Geol. 27, 769-780.

Alaniz-Álvarez, S.A., Nieto-Samaniego, Á.F. (2007). The Taxco–San Miguel de Allende fault system and the Trans-Mexican Volcanic Belt: two tectonic boundaries in central México active during the Cenozoic. In: Alaniz-Álvarez, S.A., Nieto-Samaniego, Á.F. (Eds.), Geology of México: Celebrating the Centenary of the Geological Society of México: Geological Society of America Special Paper, 422, pp. 301–316.

Benes, V., & Davy, P. (1996). Modes of continental lithospheric extension: experimental verification of strain localization processes. Tectonophysics, 254(1-2), 69-87.

Bonini, M., Souriot, T., Boccaletti, M., & Brun, J.P. (1997). Successive orthogonal and oblique extension episodes in a rift zone: Laboratory experiments with application to the Ethiopian Rift. Tectonics, 16(2), 347-362.

Brun, J.-P. (1999). Narrow rifts versus wide rifts: inferences for the mechanics of rifting from laboratory experiments. Philosophical Transactions Royal Society London, Ser. A, 357, 695-712.

Brun, J.-P., Tron, V. (1993). Development of the North Viking Graben: inferences from laboratory modelling. Sedimentary Geology, 86, 31-51.

Brun, J.-P., Beslier, M.O. (1996). Mantle exhumation at passive margins. Earth and Planetary Science Letters, 142, 161-173.

Burkett, E.R., Billen, M.I. (2010). Three dimensionality of slab detachment due to ridge–trench collision: laterally simultaneous boudinage versus tear propagation. Geochemistry, Geophysics, Geosystems 11, Q11012. doi:10.1029/2010GC003286

Burov, E. B., & Guillou-Frottier, L. (1999). Thermomechanical behavior of large ash flow calderas. Journal of Geophysical Research: Solid Earth, 104(B10), 23081-23109.

Cailleau, B., Walter, T. R., Janle, P., & Hauber, E. (2003). Modeling volcanic deformation in a regional stress field: Implications for the formation of graben structures on Alba Patera, Mars. Journal of Geophysical Research: Planets, 108(E12).

Callot, J.P., Grigne, C., Geoffroy, L., Brun, J.-P. (2001). Development of volcanic margins: Two-dimensional laboratory models. Tectonics, 20, 148-159.

Callot, J.P., Geoffroy, L., Brun, J.-P. (2002). Development of volcanic margins: Three-dimensional laboratory models. Tectonics, 21 (6), 1052, doi: 10.1029/2001TC901019.

Campos-Enriquez, J., & Garduño-Monroy, V. H. (1987). The shallow structure of Los Humeros and Las Derrumbadas geothermal fields, Mexico. Geothermics, 16(5-6), 539-554.

Carrasco-Núñez, G., McCurry, M., Branney, M.J., Norry, M., Willcox, C. (2012). Complex magma mixing, mingling, and withdrawal associated with an intraplinian ignimbrite eruption at a large silicic caldera volcano: Los Humeros of central Mexico. Geol. Soc. Am. Bull. 124, 1793–1809.

Carrasco-Núñez, G., Hernandez, J., De Leon, L., Davila, P., Norini, G., Bernal, J.P., Lopez, P. (2017a). Geologic map of Los Humeros volcanic complex and geothermal field, eastern Trans-Mexican Volcanic Belt. Terra Digitalis 1 (2), 1–11.

Carrasco-Núñez, G., López-Martínez, M., Hernández, J., & Vargas, V. (2017b). Subsurface stratigraphy and its correlation with the surficial geology at Los Humeros geothermal field, eastern Trans-Mexican Volcanic Belt. Geothermics, 67, 1-17.

Carrasco-Núñez, G., Bernal, J.P., Dávila, P., Jicha, B., Giordano, G., & Hernández, J. (2018). Reappraisal of Los Humeros volcanic complex by new U/Th zircon and 40Ar/39Ar dating: Implications for greater geothermal potential. Geochemistry, Geophysics, Geosystems, 19, 132–149.

Cedillo-Rodríguez, F. (1999). Modelo hidrogeológico de los yacimientos geotérmicos de Los Humeros, Puebla, México. Geoterm. Rev. Mex. Geoenerg. 15, 159–170.

Clifton, A. E., & Schlische, R. W. (2001). Nucleation, growth, and linkage of faults in oblique rift zones: Results from experimental clay models and implications for maximum fault size. Geology, 29(5), 455-458.

Clifton, A.E., Schlische, R.W., Withjack, M.O., Ackermann, R.V. (2000). Influence of rift obliquity on fault-population systematics: results of experimental clay models. Journal of Structural Geology, 22, 1491-1509.

Corti, G. (2004). Centrifuge modelling of the influence of crustal fabrics on the development of transfer zones: insights into the mechanics of continental rifting architecture. Tectonophysics, 384, 191-208.

Corti, G. (2005). Dynamics of periodic instabilities during stretching of the continental lithosphere: view from centrifuge models and comparison with natural examples. Tectonics, 24(2), TC2008, doi:10.1029/2004TC001739.

Corti G. (2008). Control of rift obliquity on the evolution and segmentation of the main Ethiopian rift. Nature Geoscience, 1, 258-262.

Corti, G., Manetti, P. (2006). Asymmetric rifts due to asymmetric Mohos: an experimental approach. Earth and Planetary Science Letters, 245, 315-329, doi:10.1016/j.epsl.2006.02.004.

Corti, G., Bonini, M., Innocenti, F., Manetti, P., Mulugeta, G. (2001). Centrifuge models simulating magma emplacement during oblique rifting. Journal of Geodynamics, 31, 557-576.

Corti, G., Van Wijk, J., Bonini, M., Sokoutis, D., Cloetingh, S., Innocenti, F., Manetti, P. (2003a). Transition from continental break-up to punctiform seafloor spreading: how fast, symmetric and magmatic. Geophysical Research Letters, 30 (12), 1604,

Corti, G., Bonini, M., Conticelli, S., Innocenti, F., Manetti, P., Sokoutis, D. (2003b). Analogue modelling of continental extension: a review focused on the relations between the patterns of deformation and the presence of magma. Earth-Science Reviews, 63, 169-247.

Corti G., Bonini M., Sokoutis D., Innocenti F., Manetti P., Cloetingh S., and Mulugeta G., (2004). Continental rift architecture and patterns of magma migration: a dynamic analysis based on centrifuge models. Tectonics, 23, TC2012, doi:10.1029/2003TC001561.

Corti, G., van Wijk, J., Cloetingh, S., Morley, C.K. (2007). Tectonic inheritance and continental rift architecture: Numerical and analogue models of the East African Rift system. Tectonics, 26, TC6006,

Corti, G. (2012). Evolution and characteristics of continental rifting: Analog modeling-inspired view and comparison with examples from the East African Rift System. Tectonophysics, 522, 1-33.

Dauteuil, O., Brun, J.P. (1993). Oblique rifting in a low spreading ridge. Nature, 361, 145-148.

Druitt, T. H., & Sparks, R. S. J. (1984). On the formation of calderas during ignimbrite eruptions. Nature, 310(5979), 679.

Elmohandes, S. E. (1981). The central European graben system: rifting imitated by clay modelling. Tectonophysics, 73(1-3), 69-78.

Erbello, A., Corti, G., Agostini, A., Sani, F., Kidane, T., & Buccianti, A. (2016). Modeling along-axis variations in fault architecture in the Main Ethiopian Rift: implications for Nubia-Somalia kinematics. Journal of Geodynamics, 102, 24-38.

Ferrari, L. (2004). Slab detachment control on mafic volcanic pulse and mantle heterogeneity in central Mexico. Geology, 32(1), 77-80.

Ferrari, L., Orozco-Esquivel, T., Manea, V., Manea, M. (2012). The dynamic history of the Trans-Mexican Volcanic Belt and the Mexico subduction zone. Tectonophysics, 522–523, 122–149.

Ferriz, H., Mahood, G. (1984). Eruptive rates and compositional trends at Los Humeros volcanic center, Puebla, Mexico. J. Geophys. Res. 89, 8511–8524.

García-Palomo, A., Macías, J. L., Jiménez, A., Tolson, G., Mena, M., Sánchez-Núñez, J. M., & Lermo-Samaniego, J. (2018). NW-SE Pliocene-Quaternary extension in the Apan-Acoculco region, eastern Trans-Mexican Volcanic Belt. Journal of Volcanology and Geothermal Research, 349, 240-255.

Garduño-Monroy, V., Spinnler, J., Ceragioli, E. (1993). Geological and structural study of the Chapala Rift, state of Jalisco, Mexico. Geoísica Internacional 32, 487–499.

Geyer, A., & Martí, J. (2014). A short review of our current understanding of the development of ring faults during collapse caldera formation. Frontiers in Earth Science, 2, 22.

Geyer, A., Folch, A., & Martí, J. (2006). Relationship between caldera collapse and magma chamber withdrawal: an experimental approach. Journal of Volcanology and Geothermal Research, 157(4), 375-386.

Gudmundsson, A. (2015). Collapse-driven large eruptions. Journal of Volcanology and Geothermal Research, 304, 1-10.

Gudmundsson, A. (2016). The mechanics of large volcanic eruptions. Earth-science reviews, 163, 72-93.

Gudmundsson, A. (1988). Formation of collapse calderas. Geology, 16(9), 808-810.

Gudmundsson, A., Marti, J., & Turon, E. (1997). Stress fields generating ring faults in volcanoes. Geophysical Research Letters, 24(13), 1559-1562.

Guillou-Frottier, L., Burov, E. B., & Milesi, J. P. (2000). Genetic links between ash-flow calderas and associated ore deposits as revealed by large-scale thermo-mechanical modeling. Journal of Volcanology and Geothermal Research, 102(3-4), 339-361.

Healy, D., Rizzo, R. E., Cornwell, D. G., Farrell, N. J., Watkins, H., Timms, N. E. & Smith, M. (2017). FracPaQ: A MATLAB™ toolbox for the quantification of fracture patterns. Journal of Structural Geology, 95, 1-16.

Heidbach, Oliver; Rajabi, Mojtaba; Reiter, Karsten; Ziegler, Moritz; WSM Team (2016). World Stress Map Database Release 2016. V. 1.1. GFZ Data Services. http://doi.org/10.5880/WSM.2016.001.

Holohan, E. P., Troll, V. R., Walter, T. R., Münn, S., McDonnell, S., & Shipton, Z. K. (2005). Elliptical calderas in active tectonic settings: an experimental approach. Journal of Volcanology and Geothermal Research, 144(1-4), 119-136.

Holohan, E. P., de Vries, B. V. W., & Troll, V. R. (2008). Analogue models of caldera collapse in strike-slip tectonic regimes. Bulletin of Volcanology, 70(7), 773-796.

Holohan, E. P., Walter, T. R., Schöpfer, M. P., Walsh, J. J., van Wyk de Vries, B., & Troll, V. R. (2013). Origins of oblique-slip faulting during caldera subsidence. Journal of Geophysical Research: Solid Earth, 118(4), 1778-1794.

Hubbert, M. K. (1937). Theory of scale models as applied to the study of geologic structures. Bulletin of the Geological Society of America, 48(10), 1459-1520.

Kennedy, B., Stix, J., Vallance, J. W., Lavallée, Y., & Longpré, M. A. (2004). Controls on caldera structure: Results from analogue sandbox modeling. Geological Society of America Bulletin, 116(5-6), 515-524.

Komuro, H., Fujita, Y., & Kodama, K. (1984). Numerical and experimental models on the formation mechanism of collapse basins during the Green Tuff orogenesis of Japan. Bulletin Volcanologique, 47(3), 649-666.

Komuro, H. (1987). Experiments on cauldron formation: a polygonal cauldron and ring fractures. Journal of Volcanology and Geothermal Research, 31(1-2), 139-149.

Lavallée, Y., Stix, J., Kennedy, B., Richer, M., & Longpré, M. A. (2004). Caldera subsidence in areas of variable topographic relief: results from analogue modeling. Journal of Volcanology and Geothermal Research, 129(1-3), 219-236.

Liotta, D., and WP4 Working Group, (2019). Final report on active systems: Los Humeros and Acoculco. Deliverable 4.1, GEMex project, European Union's Horizon 2020 programme, 334 pp.

Liotta, D., 2019. Los Humeros and Las Minas. Structural geology and geophysical features. GEMex 3rd Interim Meeting, 18-19 June 2019, Bochum, Germany.

Lipman, P. W. (1997). Subsidence of ash-flow calderas: relation to caldera size and magma-chamber geometry. Bulletin of volcanology, 59(3), 198-218.

López-Hernández, A., García-Estrada, G., Aguirre-Díaz, G., González-Partida, E., Palma-Guzmána, H., Quijano-León, J.L. (2009). Hydrothermal activity in the Tulancingo–Acoculco Caldera Complex, central Mexico: Exploratory studies. Geothermics 38, 279–293

Mart, Y., & Dauteuil, O. (2000). Analogue experiments of propagation of oblique rifts. Tectonophysics, 316(1-2), 121-132.

Marti, J., Ablay, G. J., Redshaw, L. T., & Sparks, R. S. J. (1994). Experimental studies of collapse calderas. Journal of the Geological society, 151(6), 919-929.

McClay, K.R., White, M.J. (1995). Analogue modelling of orthogonal and oblique rifting. Marine and Petroleum Geology, 12, 137-151.

McClay, K.R., Dooley, T., Whitehouse, P. Mills, M. (2002). 4-D evolution of rift systems: Insights from scaled physical models. American Association of Petroleum Geologists Bulletin, 86, 935-959.

Merle, O. & Abidi, N. (1995). Approche expérimentale du functionnement des rampes émergentes. Bulletin de la Société Géologique de France, 166, 439-450.

Michon, L. & Merle, O. (2003). Mode of lithospheric extension: Conceptual models from analogue modeling, Tectonics, 22, 1028,

Michon, L. & Sokoutis, D. (2005). Interaction between structural inheritance and extension direction during graben and depocentre formation: an experimental approach. Tectonophysics 409, 125-146.

Molnar, N. E., Cruden, A. R., & Betts, P. G. (2018). Unzipping continents and the birth of microcontinents. Geology, 46(5), 451-454.

Montanari, D., Agostini, A., Bonini, M., Corti, G., & Ventisette, C. (2017a). The use of empirical methods for testing granular materials in analogue modelling. Materials, 10(6), 635.

Montanari, D., Bonini, M., Corti, G., Agostini, A., & Del Ventisette, C. (2017b). Forced folding above shallow magma intrusions: Insights on supercritical fluid flow from analogue modelling. Journal of Volcanology and Geothermal Research, 345, 67-80.

Mulugeta, G. (1985). Dynamic models of continental rift valley systems. Tectonophysics, 113(1-2), 49-73.

Murase, T., & McBirney, A. R. (1973). Properties of some common igneous rocks and their melts at high temperatures. Geological Society of America Bulletin, 84(11), 3563-3592.

Naylor, M.A., van Gool, J.A.M., unpubl. Work (1982) in Mandl, G., 1988, Mechanics of tectonic faulting, 407 pp. Elsevier, Amsterdam, The Netherlands.

Naylor, M. A., Larroque, J. M., & Gauthier, B. D. M. (1994). Understanding extensional tectonics: insights from sand-box models. Geodynamic evolution of sedimentary basins: Éditions Technip, 69, 83.

Nestola, Y., Storti, F., Bedogni, E., & Cavozzi, C. (2013). Shape evolution and finite deformation pattern in analog experiments of lithosphere necking. Geophysical Research Letters, 40(19), 5052-5057.

Nestola, Y., Storti, F., & Cavozzi, C. (2015). Strain rate-dependent lithosphere rifting and necking architectures in analog experiments. Journal of Geophysical Research: Solid Earth, 120(1), 584-594.

Norini, G., Groppelli, G., Lagmay, A.M.F., Capra, L. (2006). Recent left-oblique slip faulting in the central eastern Trans-Mexican Volcanic Belt: seismic hazard and geodynamic implications. Tectonics 25, TC4012. doi:10.1029/2005TC001877

Norini, G., Groppelli, G., Sulpizio, R., Carrasco-Núñez, G., Dávila-Harris, P., Pellicioli, C., Zucca, F., De Franco, R. (2015). Structural analysis and thermal remote sensing of the Los Humeros Volcanic Complex: implications for volcano structure and geothermal exploration. J. Volcanol. Geotherm. Res. 301, 221–237.

Norini, G., Carrasco–Núñez, G., Corbo-Camargo, F., Lermo, J., Hernández Rojas, J., Castro, C., Bonini, M., Montanari, D., Corti, G., Moratti, G., Piccardi, L., Chavez, G., Zuluaga, M.C., Ramirez, M., Cedillo, F., (2019). The structural architecture of the Los Humeros volcanic complex and geothermal field. Volcanol. Geotherm. Res., 381, 312–329; doi: 10.1016/j.jvolgeores.2019.06.010.

Ramberg, H. (1981). Gravity, deformation and the earth's crust: in theory, experiments and geological application. Academic press.

Ranalli G. & Yin Z.M. (1990). Critical stress difference and orientation of faults in rocks with strength anisotropies: the two dimensional case. Journal of Structural Geology, 12, 1067-1071.

Roche, O., Druitt, T. H., & Merle, O. (2000). Experimental study of caldera formation. Journal of Geophysical Research: Solid Earth, 105(B1), 395-416.

Rosas-Elguera, J., Urrutia-Fucugauchi, J. (1998). Tectonic control on the volcano-sedimentary sequence of the Chapala graben, western Mexico. International Geology Review 40, 350–362.

Sani F., Bonini M., Corti G., Moratti G. (2019). Extension direction re-orientation in the oceanic rift of Iceland, and comparison with continental rifts. Tectonophysics, 756, 25-42.

Serra, S., & Nelson, R.A. (1988). Clay modeling of rift asymmetry and associated structures. Tectonophysics, 153(1-4), 307-312.

Sokoutis D., Corti, G., Bonini, M., Brun, J.-P., Cloetingh, S., Mauduit, T., Manetti, P. (2007). Modelling the extension of heterogeneous hot lithosphere. Tectonophysics, 444, 63-79.

Sosa-Ceballos, G., Macías, J.L., Avellán, D.R., Salazar-Hermenegildo, N., Boijseauneau-López, M.E., Pérez-Orozco, J.D. (2018). The Acoculco Caldera Complex magmas: Genesis, evolution and relation with the Acoculco geothermal system. Journal of Volcanology and Geothermal Research, 358, 288–306

Suter, M., Quintero, O., López, M., Aguirre, G., Ferrar, E. (1995). The Acambay graben: active intraarc extension in the Trans-Mexican Volcanic Belt. Tectonics 14, 1245–1262.

Suter, M., López-Martínez, M., Quintero-Legorreta, O., Carrillo-Martínez, M. (2001). Quaternary intra-arc extension in the central Trans-Mexican volcanic belt. Geological Society of America Bulletin, 113, 693–703. doi:10.1130/0016-7606.

Thielicke, W. & Stamhuis, E. (2014). PIVlab–towards user-friendly, affordable and accurate digital particle image velocimetry in MATLAB. Journal of Open Research Software, 2(1).

Troll, V. R., Walter, T. R., & Schmincke, H. U. (2002). Cyclic caldera collapse: Piston or piecemeal subsidence? Field and experimental evidence. Geology, 30(2), 135-138.

Tron, V. & Brun, J.P. (1991). Experiments on oblique rifting in brittle-ductile systems. Tectonophysics, 188, 71-84.

Verma, S.P. (1983). Magma genesis and chamber processes at Los Humeros caldera,Mexico – Nd and Sr isotope data. Nature 302, 52–55.

Verma, S.P. (2000). Geochemical evidence for a lithospheric source for magmas from Los Humeros Caldera, Puebla, Mexico. Chem. Geol. 164, 35–60.

Walter, T. R. & Troll, V. R. (2001). Formation of caldera periphery faults: an experimental study. Bulletin of Volcanology, 63(2-3), 191.

Weijermars, R. (1997). Principles of Rock Mechanics. Alboran Science Publishing, Amsterdam, 359 pp.

Weijermars, R., Schmeling, H. (1986). Scaling of Newtonian and non-Newtonian fluid dynamics without inertia for quantitative modelling of rock flow due to gravity (including the concept of rheological similarity). Physics of the Earth and Planetary Interiors 43, 316– 330.

Williams, H. (1941). Calderas and Their Origin, by Howel Williams. University of California Press.

Withjack, M.O. & Jamison, W.R. (1986). Deformation produced by oblique rifting. Tectonophysics, 126, 99-124.

Coordination Office, GEMex project

Helmholtz-Zentrum Potsdam
Deutsches GeoForschungsZentrum

Telegrafenberg, 14473 Potsdam

Germany

Coordination Office, GEMex project

Helmholtz-Zentrum Potsdam
Deutsches GeoForschungsZentrum

Telegrafenberg, 14473 Potsdam

Germany